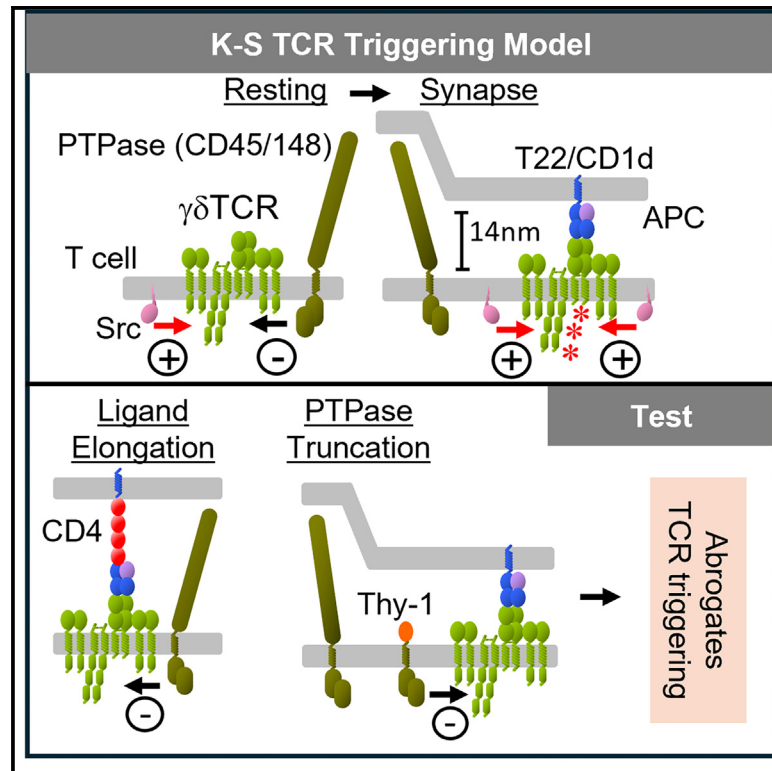


Ligand-induced segregation from large cell-surface phosphatases is a critical step in $\gamma\delta$ TCR triggering

Graphical abstract



Authors

Fenglei Li, Sobhan Roy, Jacob Niculcea, Keith Gould, Erin J. Adams, P. Anton van der Merwe, Kaushik Choudhuri

Correspondence

kaushik.choudhuri@biochem.utah.edu (K.C.),
anton.vandermerwe@path.ox.ac.uk (P.A.v.d.M.)

In brief

Li et al. use super-resolution optical imaging and electron microscopy along with size-based manipulations of CD45 distribution at the immunological synapse to show that $\gamma\delta$ TCR triggering requires segregation of large cell-surface phosphatases from engaged TCRs at synaptic contacts.

Highlights

- $\gamma\delta$ TCR triggering relies on Src kinase-mediated phosphorylation
- Size-based segregation of engaged $\gamma\delta$ TCRs from large phosphatases is necessary for triggering
- $\gamma\delta$ TCR triggering conforms to the kinetic-segregation model



Article

Ligand-induced segregation from large cell-surface phosphatases is a critical step in $\gamma\delta$ TCR triggering

Fenglei Li,^{1,2} Sobhan Roy,³ Jacob Niculcea,^{1,6} Keith Gould,⁴ Erin J. Adams,³ P. Anton van der Merwe,^{5,*} and Kaushik Choudhuri^{1,2,7,*}

¹Department of Microbiology and Immunology, University of Michigan Medical School, Ann Arbor, MI 48109, USA

²Department of Biochemistry, University of Utah School of Medicine, Salt Lake City, UT 84112, USA

³Department of Biochemistry and Molecular Biology, University of Chicago, Chicago, IL 60637, USA

⁴Department of Infectious Diseases, Imperial College London, London W2 1NY, UK

⁵Sir William Dunn School of Pathology, University of Oxford, Oxford OX1 3RE, UK

⁶Present address: Perelman School of Medicine, University of Pennsylvania, Philadelphia, PA 19104, USA

⁷Lead contact

*Correspondence: kaushik.choudhuri@biochem.utah.edu (K.C.), anton.vandermerwe@path.ox.ac.uk (P.A.v.d.M.)

<https://doi.org/10.1016/j.celrep.2024.114761>

SUMMARY

Gamma/delta ($\gamma\delta$) T cells are unconventional lymphocytes that recognize diverse ligands via somatically recombined T cell antigen receptors ($\gamma\delta$ TCRs). The molecular mechanism by which ligand recognition initiates $\gamma\delta$ TCR signaling, a process known as TCR triggering, remains elusive. Unlike $\alpha\beta$ TCRs, $\gamma\delta$ TCRs are not mechanosensitive and do not require co-receptors or typical binding-induced conformational changes for triggering. Here, we show that $\gamma\delta$ TCR triggering by nonclassical MHC class Ib antigens, a major class of ligands recognized by $\gamma\delta$ T cells, requires steric segregation of the large cell-surface phosphatases CD45 and CD148 from engaged TCRs at synaptic close-contact zones. Increasing access of these inhibitory phosphatases to sites of TCR engagement, by elongating MHC class Ib ligands or truncating CD45/148 ectodomains, abrogates TCR triggering and T cell activation. Our results identify a critical step in $\gamma\delta$ TCR triggering and provide insight into the core triggering mechanism of endogenous and synthetic tyrosine-phosphorylated immunoreceptors.

INTRODUCTION

$\gamma\delta$ T cells are unconventional lymphocytes with innate-like characteristics that play key roles in antimicrobial immunity and inflammation.^{1–3} They are activated by structurally diverse ligands via distinct somatically recombined $\gamma\delta$ T cell antigen receptors ($\gamma\delta$ TCRs).⁴ While many of the ligands that activate $\gamma\delta$ T cells remain poorly defined, major histocompatibility complex (MHC) class Ib molecules constitute a major class of membrane-tethered ligands that are recognized by both murine and human $\gamma\delta$ T cells.⁵ These minimally polymorphic nonclassical MHC class I antigens are widely expressed on immune and nonimmune cells and are upregulated on cell surfaces by intracellular stress, inflammatory mediators, or exposure to microbial components.

The $\gamma\delta$ TCR is a multi-subunit receptor complex composed of an antigen-binding $\gamma\delta$ heterodimer assembled with dimeric CD3 and TCR- ζ signaling subunits^{6,7} that contain immunoreceptor tyrosine-based activation motifs (ITAMs)⁸ in their cytoplasmic domains. Engagement of the TCR by cognate ligands initiates intracellular signaling by inducing phosphorylation of TCR ITAMs, a process known as TCR triggering.⁹ The mechanism of $\gamma\delta$ TCR triggering is not known, although several mechanisms

implicated in $\alpha\beta$ TCR triggering are likely not involved. A characteristic binding-induced conformational change in the cytoplasmic tail of CD3 ϵ subunits of $\alpha\beta$ TCRs,¹⁰ which recruits the adaptor protein Nck, does not occur in the murine G8 $\gamma\delta$ TCR following engagement by its cognate ligand T22¹¹—a murine MHC class Ib antigen. Moreover, the homologous segment of the mechanosensitive TCR C β F-G loop of $\alpha\beta$ TCRs is truncated in TCR C γ , suggesting that $\gamma\delta$ TCRs may not be mechanically activated.¹² This was recently confirmed by direct force measurements of the human $\gamma\delta$ TCR DP10.7, interacting with its cognate ligand, the sulfoglycolipid sulfatide complexed with the human MHC class Ib molecule CD1d (sulfatide-CD1d).¹³ Despite effective triggering, TCR DP10.7 binds only transiently to sulfatide-CD1d under load and lacks the characteristic catch bond force profile that correlates with pMHC-mediated $\alpha\beta$ TCR triggering. Mechanisms of triggering that rely on co-receptor-mediated TCR dimerization/aggregation are also unlikely to operate in $\gamma\delta$ T cells, as they exit the thymus at the CD4/CD8 double-negative stage during thymic development and are predominantly co-receptor negative.¹⁴

Here, we investigate whether $\gamma\delta$ TCR triggering is instead more reliant on the kinetic-segregation (K-S) model of TCR



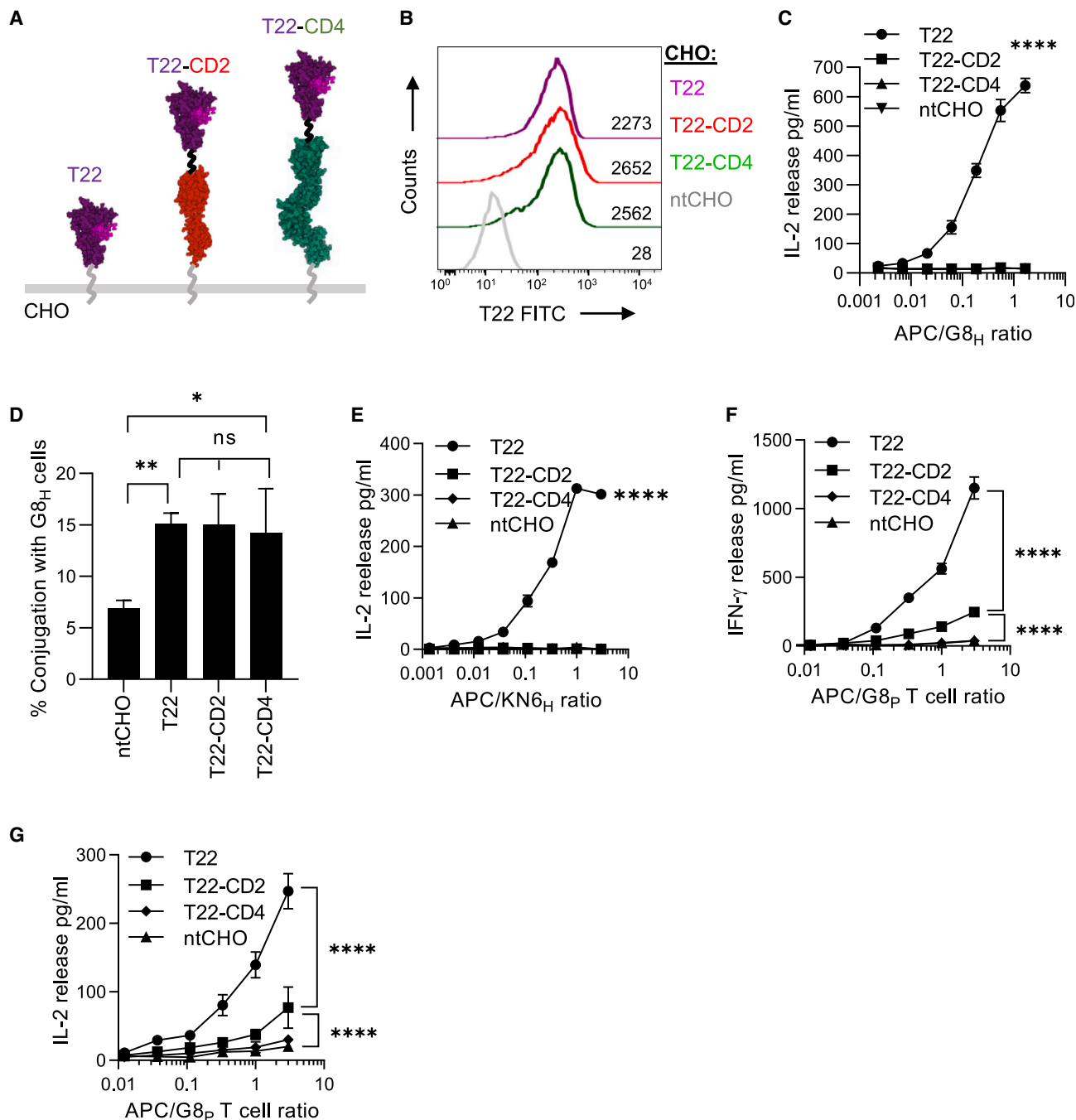


Figure 1. Elongation of murine MHC class Ib molecule T22 abrogates cognate $\gamma\delta$ T cell activation

(A) Structure-based schematic of single-chain constructs of T22 and elongated forms of T22. β 2M (pink) is attached to the N terminus of T22 using a glycine/serine linker. In elongated forms of T22, spacers derived from human CD2 or CD4 are joined to the C terminus of T22 by glycine/serine linkers (black). All constructs are tethered to the plasma membrane by the mouse H-2D^b stalk segment (gray).

(B) Histogram cascade plot of surface expression of the indicated T22 constructs in stably transfected CHO cells or untransfected CHO cells (ntCHO), detected using a T22-specific antibody and fluorescently labeled secondary anti-hamster antibody by flow cytometry. Numbers represent mean fluorescence intensity (MFI) of the associated trace.

(C) IL-2 release by cognate $\gamma\delta$ G8 T cell hybridomas (G8_H) (10^4 /well), co-cultured with increasing numbers of CHO cells expressing comparable levels of the indicated T22 constructs, or with untransfected CHO cells (nt). Results are representative of three independent experiments.

(D) Cell-cell adhesion assay using a 1:1 mixture of fluorescently labeled G8_H T cells (labeled with CFMFA—green fluorescence) and CHO cells (labeled with CellTracker Deep Red—red fluorescence) expressing the indicated T22 constructs. Heteroconjugates were detected by flow cytometry and quantitated as percentage of events “double-positive” for both G8_H T cell-associated and CHO cell-associated fluorescence.

(legend continued on next page)

triggering,¹⁵ which does not require conformational changes, mechanical forces, or co-receptor binding. The K-S model proposes that, due to the relatively small size of TCRs and their membrane-tethered ligands, TCR engagement takes place within zones of close contact between T cells and antigen-presenting cells (~15 nm), from which T cell surface phosphatases with large and bulky ectodomains, such as CD45 and CD148, are sterically excluded. The resulting shift in local kinase-phosphatase balance allows stable phosphorylation of engaged TCRs by T cell-expressed Src-family kinases such as Lck and Fyn,¹⁶ thus initiating signaling. We show that increasing access of CD45 and CD148 to sites of $\gamma\delta$ TCR engagement abrogates triggering and T cell activation, in keeping with the K-S model.

RESULTS

Co-receptors and CD3 ϵ conformational change do not contribute to $\gamma\delta$ TCR triggering

To establish which TCR triggering mechanism(s) operate in $\gamma\delta$ T cells, we chose to focus initially on the well-characterized murine G8 $\gamma\delta$ TCR and its ligand T22 as a model experimental system.¹⁷ We engineered an expression construct comprising a single-chain dimer (SCD) of T22 in which β 2M was fused to the N terminus of the T22 α chain via a 10-residue glycine/serine linker (Figures 1A and S1A). The T22 SCD construct was transfected into CHO cells, and stable transfectants were sorted by fluorescence-activated cell sorting (FACS), using T22-specific hamster monoclonal antibody (mAb) 7H9 (gift from Y.H. Chien, Stanford) and a fluorescently labeled secondary antibody, to obtain sorted CHO cells with well-defined cell-surface levels of T22 (T22-CHO) (Figure 1B). T cell hybridomas expressing cognate G8 $\gamma\delta$ TCRs (G8_H T cells) or another T22-specific TCR, KN6,¹⁸ were robustly activated by co-culture with T22-CHO cells as measured by interleukin-2 (IL-2) release in culture supernatants (Figures 1C and 1E). Neither G8 nor KN6 T cell hybridomas (KN6_H T cells) expressed detectable levels of CD8 or CD4 on their surface, precluding a role for co-receptors in their activation (Figures S1B and S1C).

The Nck-recruiting CD3 ϵ conformational change does not occur in G8 TCRs following engagement by cell-expressed T22,¹¹ although it is unclear whether this is true more generally for $\gamma\delta$ TCRs. We therefore tested for this conformational change in a second, lower-affinity (K_D 16 μ M),¹⁹ T22-specific murine $\gamma\delta$ TCR, KN6.¹⁸ KN6_H T cells were brought into contact with T22-expressing CHO cells at 4°C to induce intercellular contact and activated by incubation at 37°C for 10 min. Cell lysates were probed using a well-established TCR pull-down assay,¹⁰ modified to detect conformation-sensitive TCR binding to biotinylated Nck SH3.1 peptides immobilized on streptavidin-coated ferromagnetic beads. As with the G8 TCR,¹¹ KN6-associated TCR ζ was not immunoprecipitated by bead-immobilized Nck3.1 peptides following engagement by T22-CHO cells, or by soluble T22

tetramers (Figure S2A), but was readily detected when KN6 hybridomas were artificially stimulated with activating anti-CD3 ϵ mAb 2C11 (Figures S2A and S2B).

We also tested for the CD3 ϵ conformational change in more physiological primary $\gamma\delta$ T cells isolated from G8 TCR transgenic mice bred on a *Balb/c Rag*^{-/-} background²⁰⁻²² (gift from Y.H. Chien, Stanford). Primary G8 $\gamma\delta$ T cells (G8_P T cells) were isolated from spleen and lymph nodes and enriched by negative selection to >95% purity (Figure S2E), as measured by labeling with a fluorescent T22-tetramer (PE), and detected using flow cytometry (Figure S2E). As with G8 T cell hybridomas, G8_P T cells were robustly activated by T22-CHO cells, as measured by interferon- γ (IFN- γ) and IL-2 release (Figures 1F and 1G). However, the CD3 ϵ conformational change was not detected, either by Nck SH3.1-mediated TCR pull-down (Figures S2C and S2D) or by labeling with the conformation-sensitive anti-CD3 ϵ mAb APA1/1²³ (Figures S2F–S2H). In contrast, the CD3 ϵ conformational change was readily induced in CD4⁺ OT-II TCR transgenic T cells by tetramerized and cell-presented forms of its cognate ligand, the MHC class II molecule I-A^b complexed with ovalbumin 323–339 peptide fragment (I-A^b/OVA^{323–339}) (Figures S2I–S2L). To check whether the absence of CD3 ϵ conformational change was due to unbinding of T22 tetramers, we fixed and permeabilized G8_P T cells following a 5-min incubation with T22 tetramers or medium alone. As a positive control, OT-II_P T cells were incubated with I-A^b/OVA^{323–339} tetramers for 5 min. Staining of permeabilized and fixed cells with APA1/1 antibody and analysis by flow cytometry revealed the presence both bound tetramers and CD3 ϵ conformational change in OT-II_P T cells (Figures S3A–S3C and S3G), while APA1/1 labeling was absent in G8_P T cells despite the presence of bound T22 tetramers (Figures S3D–S3F and S3G). Taken together, these results show that typical ligand-induced conformational changes observed in murine $\alpha\beta$ TCRs are absent in murine T22-specific $\gamma\delta$ T cells.

T22 ectodomain size but not flexibility critically affects cognate $\gamma\delta$ T cell activation

We next asked whether TCR triggering proceeded according to the K-S model in $\gamma\delta$ T cells. To test this, we adapted a powerful approach employed in our previous studies of the K-S model in $\alpha\beta$ TCR triggering,^{24,25} in which we disrupted close contacts at T cell synapses using elongated cognate pMHC ligands containing rigid immunoglobulin superfamily (IgSF) domain spacers in the membrane-proximal stalk region. We used this approach to engineer chimeric expression constructs of elongated versions of T22 SCD by inserting the ectodomain sequence of human CD2 (2-IgSF domains) or human CD4 (4-IgSF domains) between the C terminus of the T22 ectodomain and the N terminus of the H-2D^b stalk and transmembrane segment (Figure 1A). Stable CHO cell transfectants expressing T22 and elongated forms of T22 were sorted for comparable surface expression and co-cultured with G8_H T cells (Figure 1B). Robust and titratable IL-2

(E) IL-2 release from KN6 $\gamma\delta$ T cell hybridomas (KN6_H) in response to increasing numbers CHO cells expressing the indicated T22 constructs.

(F) IFN- γ release by primary T22-specific primary G8 $\gamma\delta$ T cells (G8_P) in response to increasing numbers of CHO cells expressing the indicated T22 constructs.

(G) IL-2 release by primary T22-specific primary G8 $\gamma\delta$ T cells (G8_P) in response to increasing numbers CHO cells expressing the indicated T22 constructs.

Data points in (C)–(G) are means \pm SD. Means were compared by one-way ANOVA at APC/T cell ratio = 3. **** p < 0.0001, ** p < 0.01, * p < 0.05; ns, not significant (p > 0.05); p values are corrected for all pairwise comparisons. Panels are representative results of four independent experiments.

release from G8_H T cells was observed in response to T22-expressing CHO cells (Figure 1C). However, IL-2 release was completely abrogated by T22 elongation with CD2 or CD4 spacers (Figure 1C). This was not due to impaired TCR binding, as G8_H T cell adhesion to CHO cells expressing T22 constructs was unaffected by T22 elongation, as measured by a flow-cytometry-based adhesion assay (Figure 1D).²⁴ In this assay, conjugate formation between mouse T cells and CHO cells is primarily driven by TCR-ligand binding, as there is minimal cross-species adhesion between mouse and hamster cells.²⁴ Taken together, these results show that TCR-mediated activation of G8 $\gamma\delta$ T cells, as measured by “downstream” readouts of TCR signaling, is exquisitely sensitive to ligand elongation.

It remained possible that, despite effective binding, the short 5-residue glycine/serine interdomain peptide linker (g/s5) connecting the IgSF spacers to T22 may have constrained it in orientations that inhibited TCR triggering. We therefore substituted the g/s5 linker with a more flexible 10-residue glycine/serine linker (T22-g/s10) (Figures S4A and S4B).^{26,27} We also added a g/s10 linker to the stalk of unelongated T22 (T22-g/s10) to test whether increasing native ligand flexibility affected G8_H T cell activation (Figures S4A and S4B). Introduction of the g/s10 linker into native-sized T22 did not affect adhesion (Figure S4C) or activation (Figure S4D) of G8_H T cells. Conversely, replacement of the short interdomain linker connecting T22 to the CD4 spacer with the g/s10 linker failed to rescue G8_H T cell activation (Figure S4D), demonstrating that increased ectodomain flexibility of T22 constructs did not affect their activity or intermembrane spacing at synaptic contacts.

Graded attenuation of $\gamma\delta$ TCR triggering by progressive T22 elongation

To investigate whether the observed reduction in $\gamma\delta$ T cell activation in response to T22 elongation was due to reduced TCR triggering, we directly assayed T22-induced tyrosine phosphorylation of the TCR ζ chain.^{8,24} G8_H T cells were centrifuged at 4°C with CHO cells expressing T22 SCD or untransfected CHO cells as a control to induce intercellular contact and incubated at 37°C for 2–10 min to initiate signaling. TCR ζ was immunoprecipitated from sample lysates and tyrosine phosphorylation detected by SDS-PAGE and immunoblotting. A robust and sustained increase in TCR ζ phosphorylation was detectable in G8_H T cells within 2 min of co-incubation with T22-expressing CHO cells, which peaked at 5 min and remained phosphorylated after 10 min of incubation, with a progressive transition from the partially phosphorylated p21 phosphoform to the fully phosphorylated p23 phosphoform (Figure 2A).⁸ In marked contrast, CHO cells expressing T22-CD2 and T22-CD4 barely elicited detectable TCR ζ phosphorylation, which reverted to baseline levels within 10 min of co-incubation (Figures 2A and 2B). Similar results were obtained in G8_P T cells by antibody-mediated labeling of phosphorylated TCR ζ Y142, detected by flow cytometry following a 2-min incubation with CHO cells expressing T22 constructs (Figures 2C and 2D). These results directly demonstrate that G8 TCR phosphorylation is critically sensitive to T22 elongation, resulting in near complete abrogation of TCR triggering.

As a second readout of TCR triggering, we measured antigen-induced surface downregulation of the TCR, which reflects the

proportion of fully triggered and internalized TCR.²⁸ As expected, incubation of G8_H T cells with T22-CHO cells resulted in clear-cut TCR downregulation, with a ~40% reduction of surface TCR levels after 60 min of co-culture (Figures 2E and 2F). T22-CD2 and T22-CD4 elicited lower but measurable levels of TCR downregulation relative to T22, indicating weaker TCR triggering, while surface TCR levels were unchanged in T cell co-cultures with untransfected CHO cells (Figures 2E and 2F). The extent of TCR downregulation decreased in a graded manner as a function of increasing T22 ectodomain size: T22 > T22-CD2 > T22-CD4. These results show that T22 size is a critical and tunable determinant of TCR triggering.

Increased Src kinase activation does not rescue G8 TCR triggering in response to elongated T22

As in $\alpha\beta$ T cells, Src kinase-mediated tyrosine phosphorylation is critically required for T22-induced TCR triggering and “downstream” signaling in both G8_H and G8_P T cells, since chemical inhibition using the pan-Src inhibitor PP2 or the Lck-specific inhibitor A770041 results in abrogation of TCR phosphorylation (Figures S5A and S5D), which in turn leads to failure of downstream signaling as indicated by severely diminished LAT (Figures S5B and S5E) and Erk phosphorylation (Figures S5C and S5F). We therefore attempted to restore TCR triggering in response to elongated forms of T22 by short hairpin RNA (shRNA)-mediated knockdown of the tyrosine phosphatase Csk, a negative regulator of T cell Src kinases.^{29,30} We achieved an average of ~75% suppression of Csk expression in G8_H T cells (Figures S6A and S6B), while TCR surface levels, as measured by surface labeling of CD3 ϵ (Figure S6F), and Lck levels detected by immunoblot (Figures S6A and S6C), were unaffected by shRNA expression. As expected, Csk knockdown reduced phosphorylation of the negative regulatory tyrosine Y505 (Figures S6A and S6E) with a reciprocal increase in phosphorylation of the positive regulatory tyrosine Y394 (Figures S6A and S6D), consistent with increased Lck activity. Surprisingly, this did not increase T22-mediated TCR triggering in G8_H T cells as measured by intracellular Ca²⁺ influx following contact with supported lipid bilayers (SLB) containing T22 and ICAM-1 (Figure S6G). Similarly, downstream G8_H T cell activation was not increased by Csk knockdown. Rather, a marginal reduction in G8_H T cell activation was observed at high levels of antigenic stimulation (Figure S6H), which may reflect weak positive regulatory effects of Csk in $\gamma\delta$ T cells. G8_H T cell activation as measured by IL-2 release was also not rescued by Csk knockdown in response to elongated T22 ligands (Figure S6I). These results demonstrate that Lck-mediated phosphorylation is critical for G8 TCR triggering and suggest that basal activity of Lck and other Csk-regulated T cell Src kinases is sufficient to maximally trigger G8 TCRs. Unlike its function in tuning $\alpha\beta$ T cell signaling,²⁹ Csk appears not to play a substantial role in setting TCR signaling thresholds in $\gamma\delta$ T cells.

T22 elongation increases intermembrane distance at $\gamma\delta$ T cell synaptic contacts

We next investigated whether T22 elongation affected membrane positioning across synaptic contacts with G8_H T cells. Using transmission electron microscopy (TEM),^{24,31} we directly

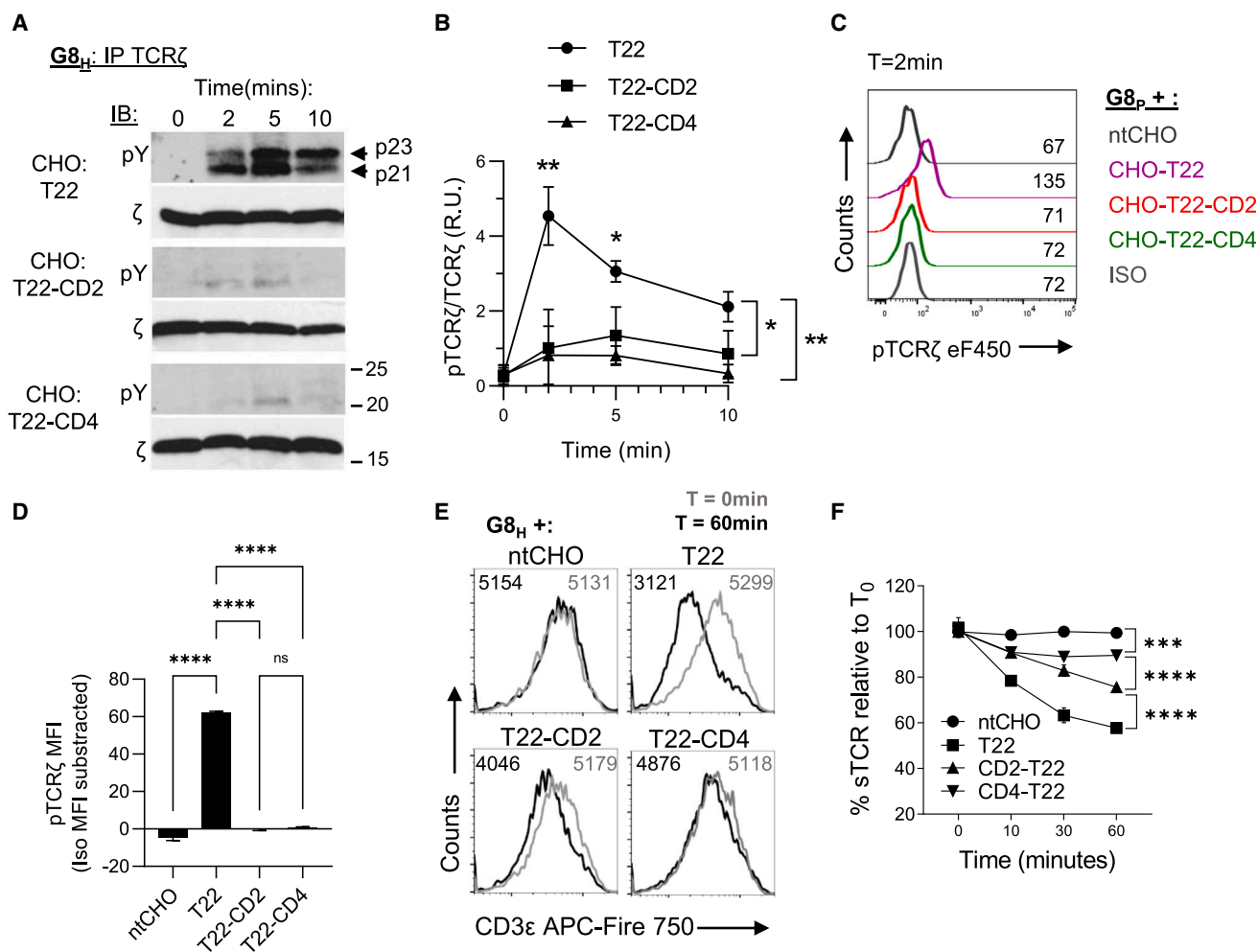


Figure 2. $G8 \gamma\delta$ TCR triggering is abolished by T22 elongation

(A) Time series of TCR ζ phosphorylation, measured by immunoprecipitation of TCR- ζ , followed by SDS-PAGE and immunoblotting with an anti-phosphotyrosine antibody (pY) to detect tyrosine-phosphorylated isoforms (arrows). p21, partially phosphorylated 21 kD ζ isoform; p23, fully phosphorylated ζ isoform. Blots were reprobed to detect unphosphorylated TCR- ζ as a loading control (ζ). Results are representative of three independent experiments.

(B) Quantitation of immunoblots in (A). Results are presented as normalized ratios of the total optical density of pY bands over that of corresponding TCR- ζ bands, following background subtraction. R.U., relative units. Data are means \pm SD. Means were compared for each time point.

(C) Histogram cascade plot of TCR ζ phosphorylation in $G8_P$ T cells following 2 min of incubation at 37°C with CHO cells expressing the indicated T22 constructs. Cells were stained with a fluorescently labeled anti-TCR ζ pY142 antibody and analyzed by flow cytometry. ISO, isotype control antibody. Results are representative of three independent experiments.

(D) Quantitation of TCR ζ pY142 staining as in (C). Results are presented as background (isotype control)-subtracted MFI. Data are means \pm SD.

(E) Representative histogram plots of TCR surface downregulation in $G8 \gamma\delta$ T cell hybridomas incubated at 1:1 ratio for 0–60 min with CHO cells expressing the indicated T22 constructs or untransfected CHO cells (ntCHO). Surface TCR was measured in unpermeabilized samples using a directly labeled mouse CD3 ϵ -specific antibody and detected by flow cytometry. Overlays of 0-min (gray) and 60-min (black) time points are shown.

(F) Time series of TCR surface downregulation, in response to T22, elongated forms of T22, or untransfected CHO cells (nt). Results are presented as percentage of surface TCR fluorescence relative to $T = 0$ levels. Results are representative of three independent experiments. Data are means \pm SD. Means at $T = 60$ s were compared.

Means were compared by one-way ANOVA corrected for all pairwise comparisons. * $p < 0.05$, ** $p < 0.01$, *** $p < 0.001$, **** $p < 0.0001$; ns, not significant ($p > 0.05$).

measured intermembrane distances at synaptic interfaces between $G8_H$ T cell hybridomas and CHO cells expressing T22 or T22-CD4. To achieve this, conjugates of $G8_H$ T cells with CHO cells expressing T22 constructs were fixed after 2 min of incubation at 37°C and processed for TEM. Thin sections were screened to identify T cell:CHO cell heteroconjugates (Figure 3A), and intermembrane distance was measured at ~200- to 400-nm

intervals along the contact interface (Figures 3B and 3D). Intermembrane distance measurements were plotted as normalized frequency distributions of intermembrane distances with a bin of 2 nm (Figures 3C and 3E). The mean intermembrane distance at interfaces between $G8_H$ T cells and T22-expressing CHO cells was 13.5 ± 2.7 nm, consistent with the end-to-end span of the T22-G8 complex structure determined by X-ray

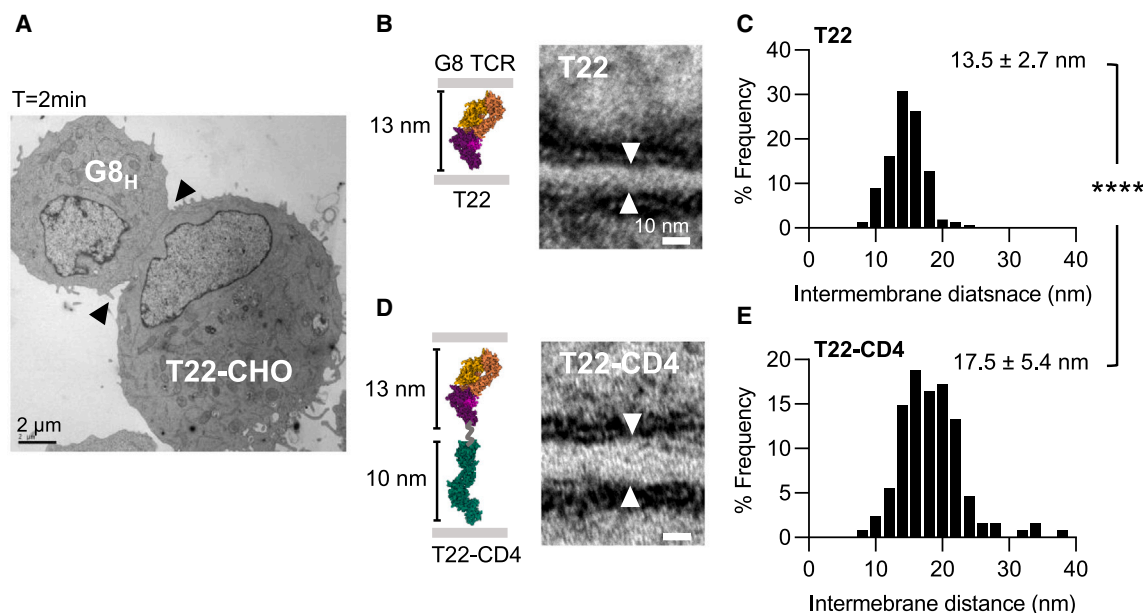


Figure 3. T22 elongation increases intermembrane spacing and at G8 T cell synaptic contacts

(A) Representative heteroconjugate between a G8_H T cell and CHO cell expressing T22. Arrowheads indicate G8-CHO cell synapse along which the intermembrane distances of apposed plasma membranes were measured.

(B and D) (Left) Structure-based cartoon of T22 (B) and elongated T22-CD4 constructs (D) with estimated dimensions of ectodomains. Flexible 5 residue glycine/serine linker joining T22 to the CD4 spacer is shown in gray. (Right) Representative high-magnification image of a region of synaptic contact between G8_H T cell and CHO cells expressing T22 (B) or T22-CD4 (D). Arrowheads indicate region at which intermembrane distance measurements were made, at which G8_H T cell and CHO cell plasma membranes are parallel and orthogonal to the imaging plane, as indicated by their “tramline” morphology.

(C and E) Frequency distribution of intermembrane distances at synaptic contacts. A total of 189 measurements along synaptic contacts were taken from 15 conjugates between G8 T cell hybridomas and CHO cells expressing T22 (C), and 117 measurements were taken from 18 conjugates with CHO cells expressing T22-CD4 (E). Measurements were pooled from three independent experiments. Mean intermembrane distance \pm SD is shown in each panel. Means were compared by two-tailed t test. **** $p < 0.0001$.

crystallography¹⁷ (Figures 3B and 3C) and also consistent with the formation of close-contact zones induced by TCR engagement. Mean intermembrane distance was significantly increased at G8_H T cell interfaces with T22-CD4 expressing CHO cells to 17.5 ± 5.4 nm, with a maximum intermembrane distance of ~ 28 nm, consistent with the estimated dimensions of the fully extended G8 TCR:T22-CD4 complex span (Figures 3D and 3E). Intermembrane distances were more variable at G8_H TCR:T22-CD4 interfaces, reflected in a 2-fold increase in the standard deviation (SD) relative to TCR:T22 interfaces, likely due to increased flexibility of elongated T22-CD4. Substitution with a longer and more flexible g/s10 spacer into the stalk of unelongated T22, or in the interdomain linker connecting T22 and CD4, did not change the mean intermembrane spacing at synaptic contacts (Figure S3E), indicating that the rigid IgSF-containing spacers, and not the flexible linkers, were the primary determinants of intermembrane separation distance at synaptic contacts. We show here that apposed membranes at T22-induced contacts with G8_H T cells are positioned at a distance that is consistent with the T22:G8 TCR complex span (13.5 nm), as would be expected at close contacts formed by TCR engagement to T22 at synaptic interfaces. T22 elongation with IgSF spacers significantly increases intermembrane distance at synaptic contacts, by an average of ~ 4 nm, potentially allowing greater access of CD45 to engaged TCRs.

T22 ectodomain size controls $\gamma\delta$ TCR segregation from CD45 at T cell synapses

We next sought to determine whether T22 elongation affected the distribution of CD45 at G8 T cell contact interfaces. We first confirmed surface expression of CD45 (and the related phosphatase CD148) on G8_p T cells by flow cytometry (Figure S7D). Using confocal fluorescence microscopy, we measured TCR and CD45 distributions in G8_p T cell conjugates with CHO cells expressing T22, T22-CD4, or nontransfected CHO cells (ntCHO) as a control. Conjugates were fixed after 2 min of incubation at 37°C, and permeabilized samples were labeled with primary antibodies to TCR and CD45, followed by appropriate fluorescently labeled secondary F(ab')₂ fragments, and imaged by laser-scanning confocal microscopy (Figure 4A). Robust and comparable TCR accumulation was observed at T cell synapses with CHO cells expressing T22 and T22-CD4 (~ 2 -fold enrichment), indicating similar levels of TCR engagement (Figures 4A and 4B). In contrast, very few G8_p T cell conjugates with ntCHO cells were detected, in which TCR was not enriched at synaptic contacts, confirming that TCR enrichment resulted through engagement of cognate ligands. A small ($\sim 20\%$) but reproducible overall depletion of CD45 was observed at synapses with T22-expressing CHO cells (Figures 4A and 4C), indicating overall exclusion of CD45 from T22-mediated synaptic contacts. In contrast, CD45 levels at synapses with CHO cells

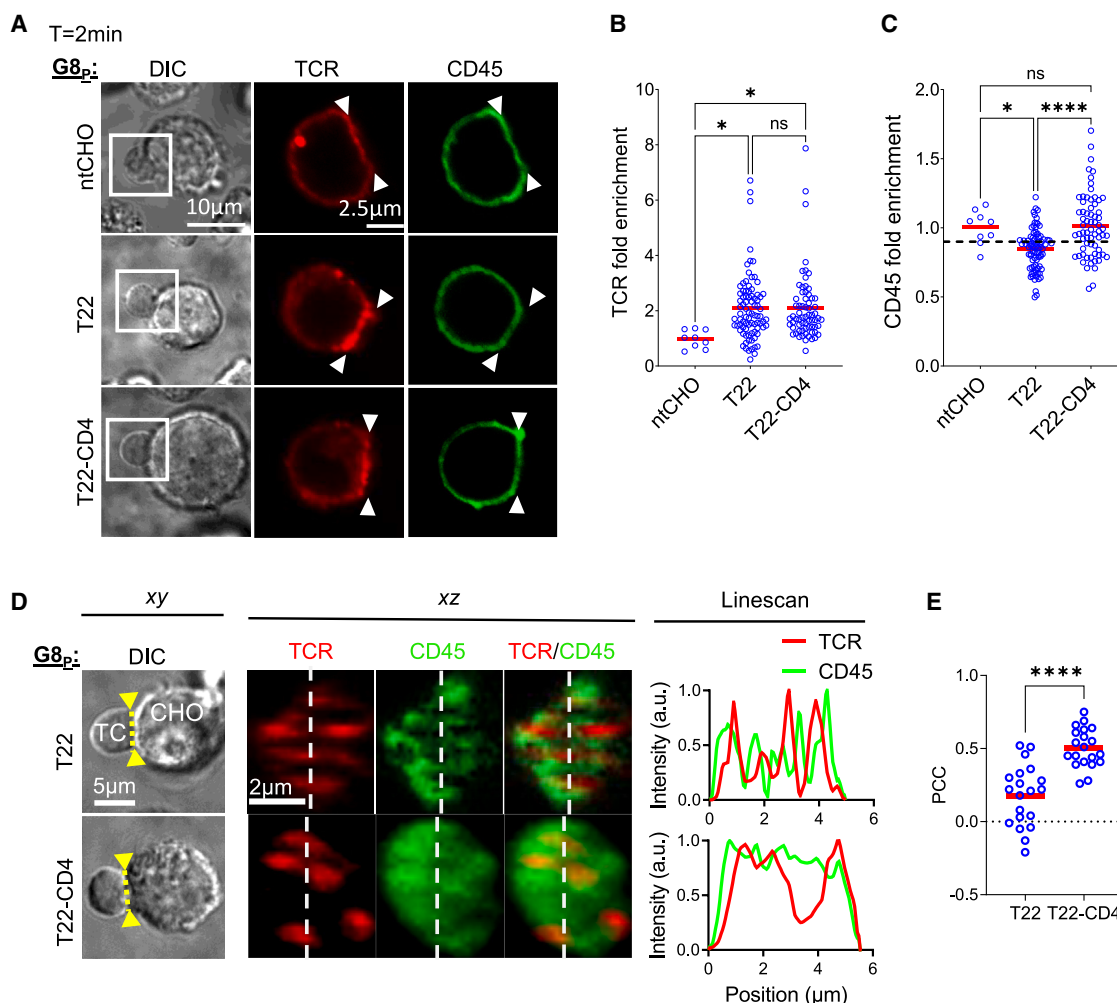


Figure 4. T22 ectodomain size controls CD45 segregation from TCR at G8 T cell synapses

(A) Representative confocal fluorescence images of conjugates of primary G8 T cells (G8p) with CHO cells expressing T22 or T22-CD4, or with nontransfected CHO cells (ntCHO) as a control. TCR (red) and CD45 (green) were labeled using specific primary antibodies and fluorescently labeled secondary F(ab')₂ fragments. Fluorescence images of T cells in boxed regions of differential interference contrast (DIC) images are shown in right panels. Arrowheads indicate position of synaptic interface in DIC image.

(B and C) Quantitation of TCR (B) and CD45 (C) at synaptic contacts expressed as the ratio of [mean plasma membrane fluorescence intensity at synaptic interface]/[mean plasma membrane fluorescence intensity in nonsynaptic region]. Each data point represents measurements from one T cell:CHO cell conjugate; red bars indicate means. Results are pooled from six independent experiments. Means were compared by one-way ANOVA corrected for all pairwise comparisons.

(D) Representative DIC image of G8p T cell with CHO cells expressing T22 or T22-CD4 (left panels). Yellow dotted line and arrowheads indicate xz plane sampled in fluorescence image z stacks of TCR (red) and CD45 (green) labeled as in (A) to reconstruct *en face* views of the synaptic interface (middle panels). Overlays of fluorescence intensities of TCR and CD45 along line scans positioned across *en face* synapse reconstructions (white dotted line) are shown in right panels.

(E) Quantitation of co-localization between TCR and CD45 at reconstructed *en face* synaptic interfaces using Pearson's correlation coefficient (PCC). Each data point represents measurements from one T cell:CHO cell conjugate; red bars indicate means. Means were compared by two-tailed t test.

* $p < 0.05$, **** $p < 0.0001$; ns, not significant ($p > 0.05$); p values are corrected for all pairwise comparisons. Results are pooled from five independent experiments.

expressing T22-CD4 were unchanged relative to nonsynaptic plasma membrane regions and were comparable to levels at synaptic contacts with ntCHO cells. Taken together, these data indicate that synaptic depletion of CD45 is dependent on the short span of T22-G8 TCR complexes, and elongating T22 results in increased overall access of CD45 to the T cell contact interface (Figures 4A–4C), despite comparable TCR engagement.

To measure the extent of overlap in TCR and CD45 distributions at synaptic contacts, we reconstructed *en face* (end-on) projections of synaptic interfaces from confocal z stacks of conjugates between G8 T cells and CHO cells expressing T22 or T22-CD4.³² Although the resolution of synapse reconstructions was limited by the axial anisotropy of the confocal point spread function, TCR microclusters, which form following TCR engagement,³³ could be resolved at contact interfaces (Figure 4D). CD45 was

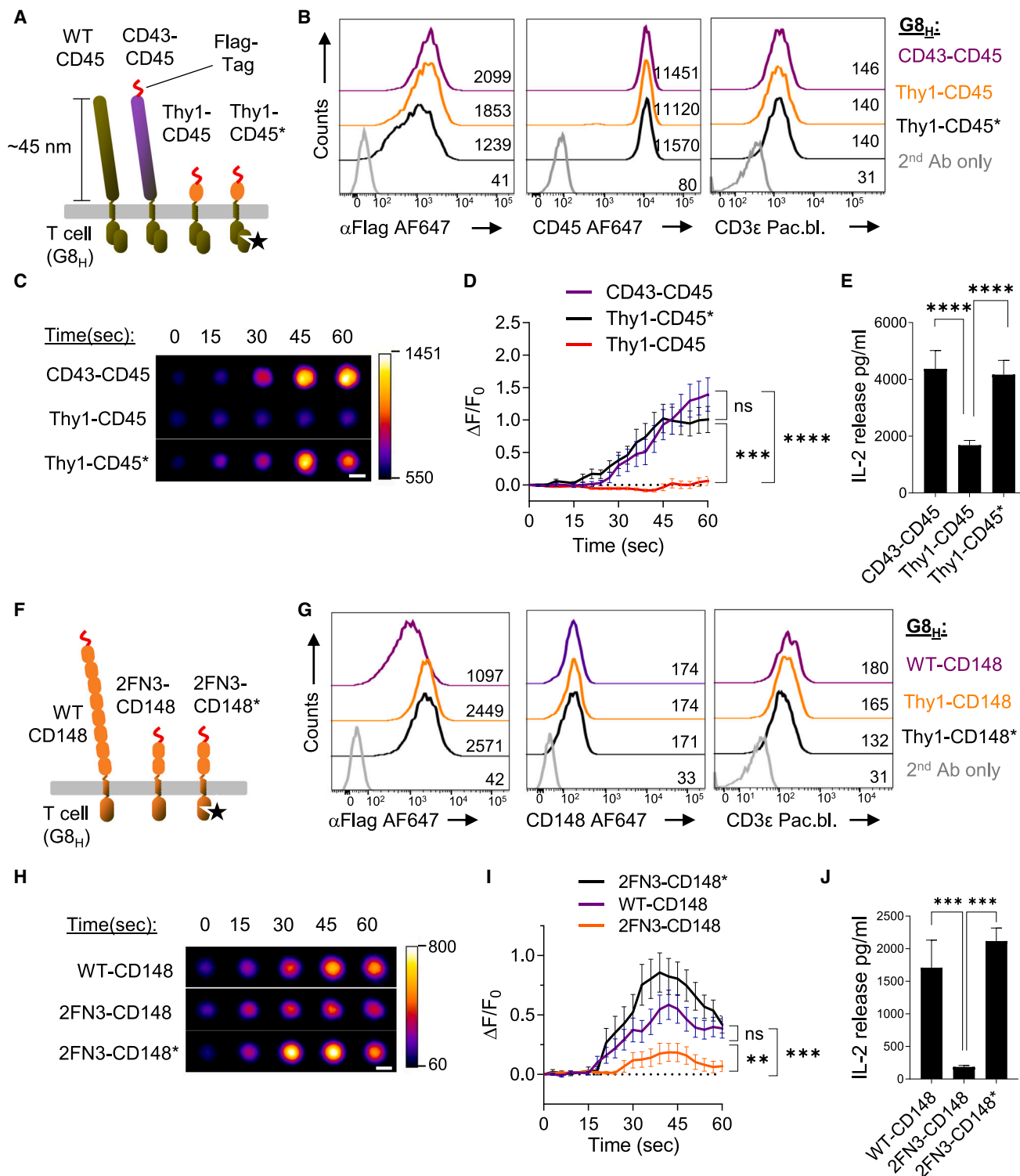


Figure 5. Truncation of the CD45 and CD148 ectodomains abrogates $\gamma\delta$ TCR triggering and T cell activation

(A) Schematic of wild-type CD45 (shown for comparison), and chimeras of the wild-type CD45 cytoplasmic domain fused to the ectodomains of CD43 (CD43-CD45) or Thy-1 (Thy1-CD45), depicted approximately to scale. Also shown is a chimera of a catalytically inactive mutant of the CD45 endodomain fused to the Thy-1 ectodomain (Thy1-CD45*). All constructs contain an N terminus FLAG tag (shown in red) and were stably expressed in G8 T cell hybridomas (G8_H). (B) Fluorescence histograms of cell-surface levels of the indicated CD45 chimeras (α Flag), endogenous CD45, and TCR (CD3 ϵ) in G8_H T cell transductants. CD43-CD45 transductants were stained with secondary antibody only as a labeling control. G8_H T cells were sorted for comparable expression levels of CD45 chimeras.

(legend continued on next page)

segregated from TCR microclusters at contact interfaces with T22-expressing CHO cells, resulting in anti-correlation between TCR and CD45 intensities across line scans of interface regions (Figure 4D). Characteristic “holes”³³ in the CD45 distribution in regions occupied by T22-induced TCR microclusters indicated CD45 exclusion from engaged TCRs (Figure 4D). In contrast, there was much greater overlap of CD45 distributions with TCR microclusters in *en face* reconstructions of synapses with T22-CD4-expressing CHO cells (Figure 4D), quantitated as a highly significant increase in Pearson’s correlation coefficient, indicating greater co-localization between CD45 with TCR (Figure 4E).

CD45 and CD148 ectodomain size is a critical determinant of TCR triggering

While T22 elongation increases CD45 access to engaged TCRs at synaptic contacts, it remained possible that introduction of non-native IgSF spacers may also have adversely affected triggering by altering cryptic mechanical and structural properties that are important for TCR triggering. To rule this out, we examined the effects of truncating the large ectodomains of CD45 or CD148 on $\gamma\delta$ TCR triggering by native T22. We engineered constructs of murine CD45 in which the native ectodomain was replaced with the single IgSF-containing ectodomain of rat Thy1 (Thy1-CD45) or with the ectodomain of rat CD43 (CD43-CD45) (Figures 5A and S1A), which is comparable in size to CD45 (~45 nm).^{34,35} We also made a Thy1-CD45 catalytically inactive mutant (Thy1-CD45*) to measure the contribution of its phosphatase activity on TCR triggering (Figures 5A and S1A).³⁶ All constructs contained N terminus FLAG tags for immunolabeling, cell sorting, and fluorescence imaging (Figure 5A). CD45 expression constructs were retrovirally transduced into G8 T cell hybridomas (G8_H) and transductants sorted for comparable surface levels (Figure 5B). Endogenous CD45 and TCR surface levels were also comparable across transductants (Figure 5B).

We measured ligand-induced Ca^{2+} flux in transduced G8_H T cells to determine whether truncating the CD45 ectodomain affected TCR triggering. T cell transductants were loaded with Fluo-4 fluorescent Ca^{2+} indicator, and intracellular Ca^{2+} influx was monitored by live-cell epifluorescence microscopy of

T cells interacting with SLBs containing T22. G8_H T cells transduced with CD43-CD45 exhibited robust Ca^{2+} influx within 30 s of contact with bilayers (Figures 5C and 5D), comparable to mock transduced G8_H T cells (Figure S7B). Strikingly, Ca^{2+} influx was abolished in G8_H T cells expressing Thy1-CD45 at 0.5% of endogenous CD45 levels but was unaffected by expression of comparable levels of catalytically inactive Thy1-CD45 (Figures 5C and 5D; Table S1), indicating that CD45-mediated dephosphorylation was responsible for the abrogation of triggering by Thy1-CD45. IL-2 release by CD43-CD45 transductants was similar to mock transduced G8_H T cells (Figure S7C), showing that activation of Thy1-CD45-expressing G8_H T cells was significantly reduced in co-cultures with T22-expressing CHO cells, relative to CD45-CD43 transductants, but was unaffected in Thy1-CD45*-expressing G8_H T cells (Figure 5E).

Using a similar approach, we next generated stable transductants of G8_H T cells expressing full-length CD148, a truncated form containing two (of seven) of its fibronectin type III domains (2FN3-CD148) and a truncated construct that was catalytically inactive (2FN3-CD148*) (Figures 5F and S1A).³⁶ Cells were sorted for comparable expression of transduced constructs and checked to compare endogenous CD148 and TCR surface levels (Figure 5G). G8_H T cell transductants expressed levels of endogenous CD148 comparable to those of primary G8 (G8_P) T cells (Figure S7A and Table 1). Overexpression of wild-type CD148 in G8_H T cells stimulated robust Ca^{2+} responses to T22 on SLBs, comparable to mock transduced G8_H T cells (Figure S7B). In contrast, Ca^{2+} influx was abrogated in transductants expressing 2FN3-CD148 (Figures 5H and 5I). However, transduction with 2FN3-CD148* (which lacks phosphatase activity) resulted in Ca^{2+} influx comparable to that of wild-type CD148 transductants (Figures 5H and 5I). In keeping with the observed Ca^{2+} responses, 2FN3-CD148 expression substantially reduced IL-2 release relative to wild-type CD148 transductants, while IL-2 release by G8_H T cells expressing 2FN3-CD148* was comparable to that of wild-type CD148 transductants (Figure 5J) and mock-transduced G8_H T cells (Figure S7C). Taken together, these results demonstrate that the large ectodomains of CD45 and CD148 are necessary for ligand-induced $\gamma\delta$ TCR

(C) Time series of calcium flux fluorescence imaging of Fluo-4-loaded G8_H T cells, transduced with the indicated CD45 chimeras, interacting with SLBs containing 100 molecules/ μm^2 T22 and 350 molecules/ μm^2 ICAM-1. Images at each time point are centered averages of 25 cells for CD43-CD45, 20 cells for Thy1-CD45, and 30 cells for Thy1-CD45*. Pseudocolor scale indicates Fluo-4 fluorescence intensity in arbitrary units. Scale bar, 5 μm .

(D) Quantitation of Fluo-4 fluorescence intensity over time as a measure of intracellular Ca^{2+} flux in G8_H T cell transductants. Data points are means \pm SEM; $n = 61$ cells (CD43-CD45), 29 cells (Thy1-CD45), and 51 cells (Thy1-CD45*), pooled from four independent experiments.

(E) IL-2 release by indicated G8_H T cell transductants in 1:1 co-cultures with CHO cells expressing T22. Results are representative of five independent experiments.

(F) Schematic of wild-type CD148 (WT-CD148) and an ectodomain truncation retaining two membrane-proximal fibronectin type III domains (2FN3-CD148), transduced into G8_H T cells, depicted approximately to scale. Also shown is a chimera of a catalytically inactive version of 2FN3-CD148 (2FN3-CD148*). All chimeras have an N-terminal FLAG tag.

(G) Fluorescence histograms of cell-surface expression levels of CD148 chimeras (α Flag), endogenous CD148, and TCR (CD3 ϵ) in stably transduced G8_H T cells expressing the indicated chimeras. G8_H T cells were sorted for comparable surface expression levels of CD148 chimeras.

(H) Time series of averaged epifluorescence images of Fluo-4-labeled G8_H T cell transductants expressing the indicated CD148 chimeras, interacting with SLBs as in (C). Images at each time point are centered averages of 22 WT-CD148-, 18 2FN-CD148-, and 25 2FN-CD148*-expressing G8_H T cells.

(I) Quantitation of Fluo-4 fluorescence intensity over time as in (H). Data points are means \pm SEM. $N = 46$ cells (WT-CD148), 40 cells (2FN-CD148), and 38 cells (2FN-CD148dead), pooled from two independent experiments.

(J) IL-2 release by indicated G8_H T cells in 1:1 co-cultures with CHO cells expressing T22. Results are representative of five independent experiments.

Means were compared by one-way ANOVA corrected for all pairwise comparisons. Statistical comparisons in (D) and (I) are for data points at $T = 60$ s.

**** $p < 0.0001$, *** $p < 0.001$, ** $p < 0.01$; ns, not significant ($p > 0.05$).

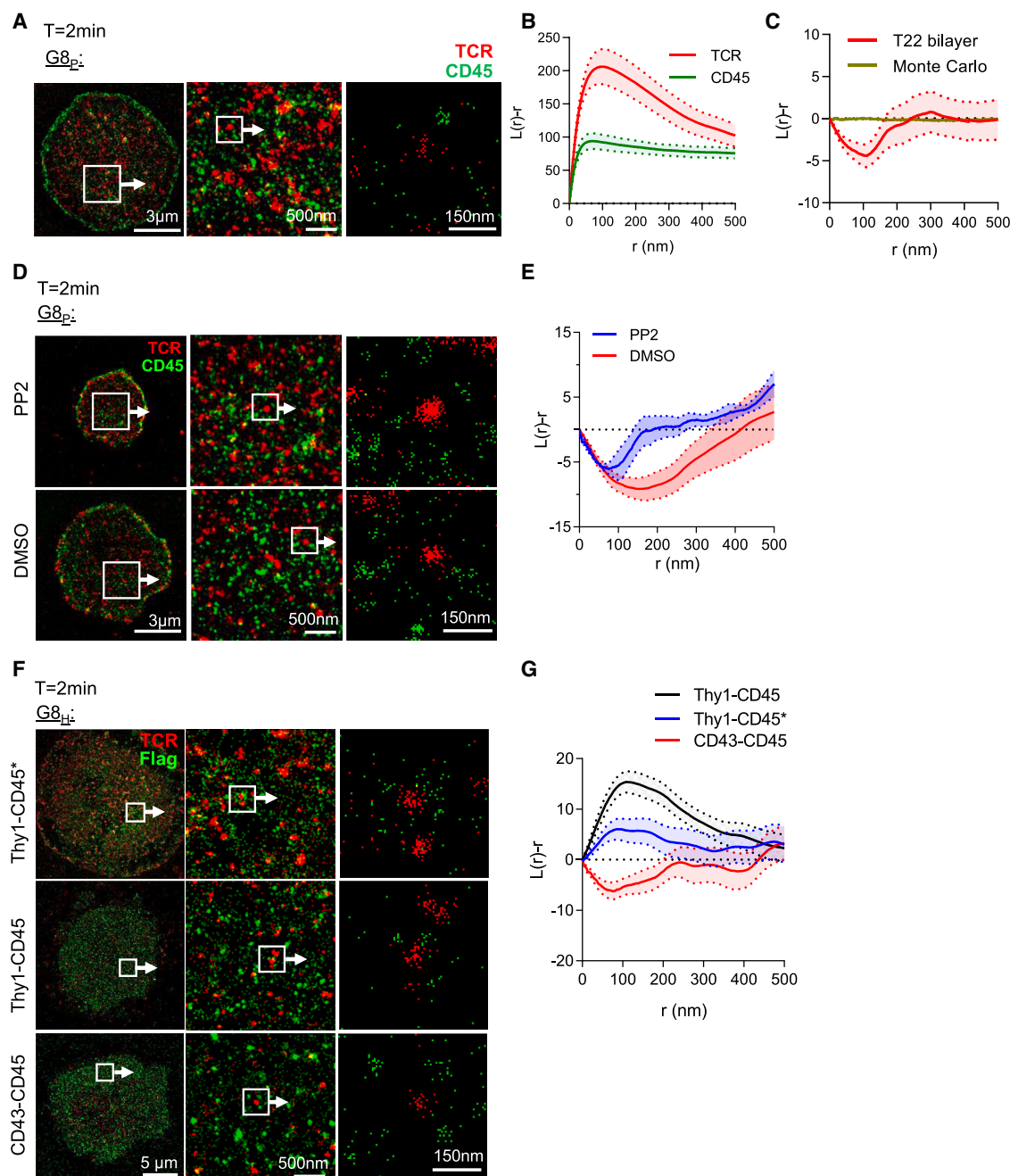


Figure 6. Truncated CD45 fails to segregate from $\gamma\delta$ TCR at synaptic contacts

(A) (Left) Representative low-magnification image of a TIRF-dSTORM Gaussian-filtered overlay of endogenous TCR and CD45 localizations at a G8_p T cell synapse, formed on an SLB containing 100 molecules/ μm^2 T22 and 350 molecules/ μm^2 ICAM-1 following 2 min of incubation at 37°C. Image intensity approximates localization density. (Middle) High-magnification Gaussian-filtered image of boxed region of left panel. (Right) Unfiltered localizations of endogenous TCR and CD45 in boxed region of middle panel (each dot represents a single antibody-associated fluorophore localization).

(B) Autocorrelation of endogenous TCR and CD45 localizations as a function of distance calculated as Ripley's H function. Peak values approximate cluster size (nm) and extent of clustering. Graphs represent means \pm SEM of 14 randomly selected regions of interest (ROIs) from 14 synapses of G8_p T cells pooled from three independent experiments. Shaded envelope within dotted lines represents \pm SEM.

(C) Cross-correlation of endogenous TCR and CD45 using Ripley's H function. Negative values indicate dispersion (segregation), and positive values indicate co-clustering. Random distribution represents the mean 2D Poisson distributions from 20 Monte Carlo simulations.

(D) Representative images of TIRF-dSTORM Gaussian-filtered overlays of endogenous TCR and CD45 localizations at synapses formed by G8_p T cells treated with PP2 or DMSO vehicle. Cells were pretreated for 30 min and concentrations maintained during synapse formation until fixed with paraformaldehyde.

(legend continued on next page)

phosphorylation and suggest that truncating their ectodomains abrogates segregation from TCR at synaptic contacts. Abrogation of TCR triggering by overexpression of ectodomain-truncated forms of CD45 and CD148 at substantially lower levels than their endogenous (full-length) counterparts demonstrates the acute susceptibility of G8 TCRs to dephosphorylation by these surface-expressed phosphatases and underscores the critical need for efficient lateral segregation for triggering (Table S1).

CD45 ectodomain size controls nanoscale segregation from T22-engaged G8 TCRs

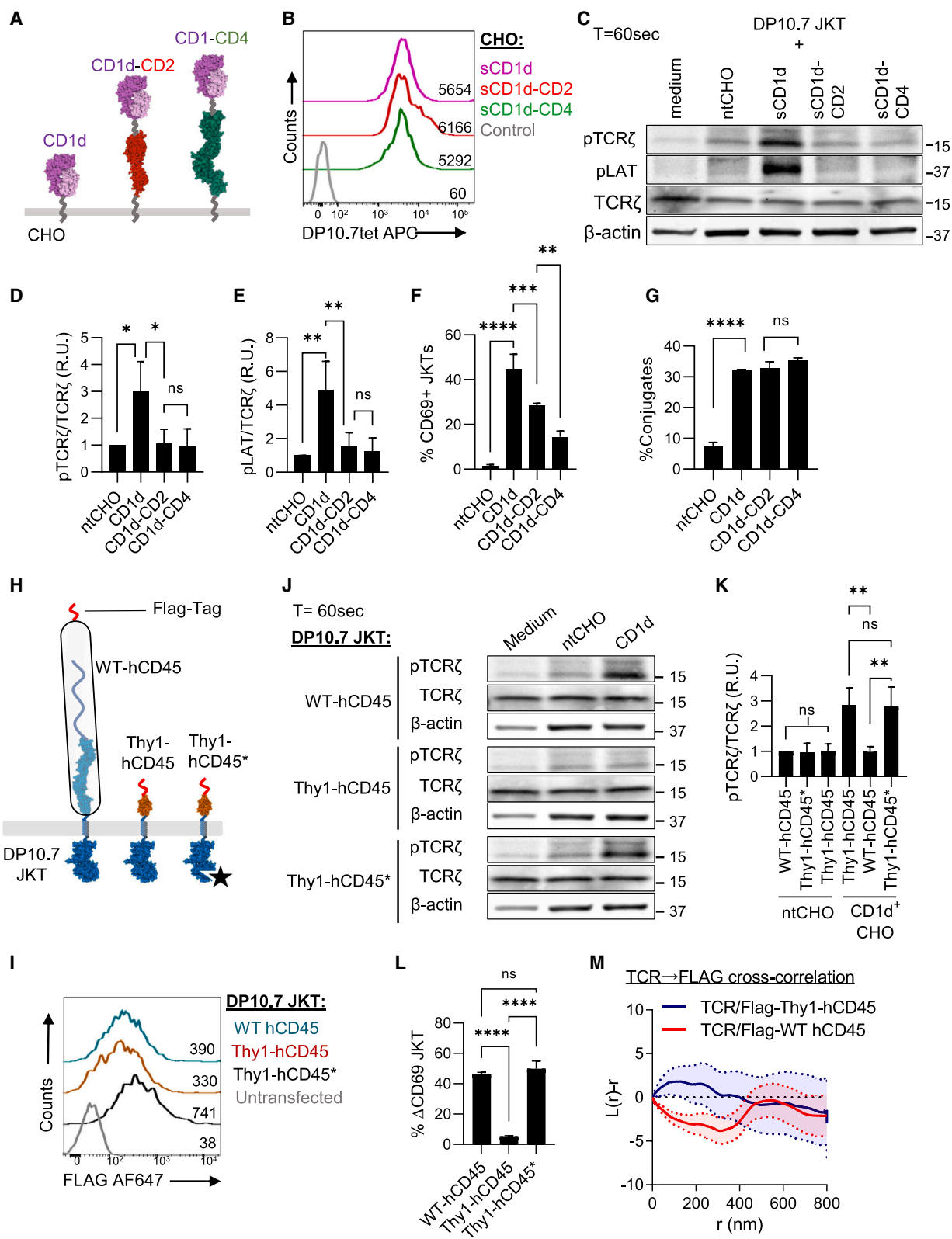
To investigate whether ectodomain size controls CD45 segregation from TCR at synaptic contacts, we performed two-dimensional (2D) direct stochastic optical reconstruction microscopy (dSTORM) using a TIRF (total internal reflection fluorescence) illumination platform.^{37,38} TIRF excitation substantially improved imaging signal/noise and localization accuracy, resulting in global image resolution of ~ 55 nm as estimated by Fourier ring correlation.³⁹ TCR and CD45/FLAG-tag constructs were labeled as for confocal microscopy, using secondary F(ab')₂ fragments conjugated with defined numbers of Atto488 and AF647 fluorophores, which spontaneously photoswitch under mild reducing conditions.⁴⁰ Effective lateral diffusion of bilayer-attached ligands is critical for binding-induced TCR clustering at early synapses (Figure S8A) and subsequent translocation to the synapse center (central supramolecular activation cluster [cSMAC]), where it is surrounded by an adhesive ICAM-1/LFA-1 ring (peripheral SMAC [pSMAC]) that is characteristic of mature synapses (Figure S8B). Bilayer mobility was checked by fluorescence recovery after photobleaching prior to all experiments (Figures S8C and S8D). To establish a baseline in unmanipulated cells, G8_P T cells were fixed after 2 min of incubation at 37°C with T22-containing SLBs and processed for two-channel dSTORM imaging (Figures 6A and 6B). Localizations were mapped and analyzed using Ripley's H function $L(r) - r^{41,42}$ for single-channel 2D spatial point autocorrelation (amplitude indicates relative cluster density, and r at maxima indicates approximate cluster radius) and two-channel cross-correlation (negative values indicate segregation). TCRs were highly clustered at G8_P T cells synapses, with a predominant cluster radius of ~ 100 nm (Figures 6A and 6B). In contrast, endogenous CD45 exhibited minimal clustering, with an autocorrelation amplitude and cluster size comparable to fluorophore localizations of primary and secondary antibody complexes alone (Figures 6A–6C and S8E–S8J). Cross-correlation analysis revealed CD45 segregation from TCR at nanometer-length scales, most prominent at ~ 100 nm radius, consistent with CD45 segregation from TCR nanoclusters (Figure 6C). To investigate whether CD45

segregation from TCR is a consequence of ligand engagement or whether it also requires TCR triggering, we pretreated G8_P T cells with PP2 (Figure S5A) and examined TCR and CD45 distributions at T22-induced synapses by dSTORM. Treatment with DMSO vehicle alone appeared to accentuate CD45 segregation from TCR, reflected in an increase in the maximal segregation radius from ~ 100 nm to ~ 200 nm (Figure 6E), which may reflect DMSO-induced changes in membrane flexibility and fluidity. Following treatment with PP2, CD45 remained segregated from TCR, although the maximal segregation radius decreased to ~ 100 nm (Figure 6E). This apparent change likely reflects increased overall density of CD45 and TCR at smaller synaptic footprints, since PP2 also inhibits LFA-1-mediated cell spreading. Despite this, CD45 remained segregated from TCR at length scales corresponding to TCR clusters (~ 100 nm), suggesting that the resulting CD45 segregation was dependent on TCR engagement, but Src kinase-mediated TCR phosphorylation was not required, consistent with a causal role in initiating TCR signaling (Figures 6D and 6E). Since TCR triggering also regulates inside-out LFA-1 activation,⁴³ it remains possible that CD45 redistribution is maximized, beyond the length scales necessary for segregation from engaged TCR clusters, by effective LFA-1 activation and cell spreading.⁴⁴ Comparable in size to endogenous CD45, CD43-CD45 also exhibited nanoscale segregation from TCR (Figures 6F and 6G). In stark contrast, CD45 chimeras with Thy1-substituted ectodomains, Thy1-CD45 and catalytically inactive Thy1-CD45*, were no longer segregated from TCR and could be detected within TCR clusters (Figures 6F and 6G). Thy1-CD45 appeared more co-clustered with TCR than Thy1-CD45*, which may reflect an increase in membrane roughness at synapses due to the abrogation of triggering and loss of consequent actin-mediated protrusive flattening. Such membrane unevenness may result in portions of the synaptic membrane lying outside the TIRF excitation field (which extends ~ 100 nm above the coverslip), leading to relative undercounting of both TCR and CD45 outside of close contacts, which are always well within the TIRF field. Endogenous CD45 remained segregated from TCR in both CD43-CD45- and Thy1-CD45-transduced G8_H T cells (Figures S8K and S8L). These results demonstrate that ectodomain size is the principal determinant of CD45 segregation from TCRs at synaptic contacts. The large ectodomain of endogenous CD45 is required for segregation from TCR, which is preserved when the CD45 ectodomain is substituted with the comparably sized but structurally unrelated ectodomain of CD43. Segregation from TCR is abolished by substitution of the CD45 ectodomain with the small single IgSF Thy-1 ectodomain. Since overexpression of CD148 constructs functionally phenocopies transduction with CD45 constructs, it seems likely

(E) Cross-correlation plot of endogenous TCR and CD45 at synapses in (D). Graphs show means \pm SEM. Data are from ten ROIs sampled from ten DMSO-treated cells, and four ROIs from four PP2-treated cells, randomly chosen from a pool of three independent experiments. Data show means \pm SEM.

(F) G8_H T cell transductants forming synapses with SLB as in (A). (Left) Representative TIRF-dSTORM Gaussian-filtered overlays of TCR and the indicated CD45 chimeras (Flag). (Middle) High-magnification images of boxed region in left panels. (Right) Unfiltered localizations of TCR and CD45 chimeras in boxed regions of middle panels (each dot represents a single fluorophore localization).

(G) Cross-correlation of TCR and CD45 chimeras in G8_H T cell transductants forming synapses as in (F). For CD43-CD148 $n = 29$ ROIs, for Thy1-CD148 $n = 38$ ROIs, for Thy1-CD45* $n = 84$ ROIs. ROIs were randomly chosen from a total of 13 synapses for each condition, pooled from three independent experiments. Data are means \pm SEM.



(legend on next page)

that its large ectodomain is similarly required for segregation from engaged TCRs.

Triggering of sulfatide/CD1d-specific human $\gamma\delta$ TCR DP10.7 requires CD45 segregation

We next sought to determine whether phosphatase segregation was also a critical requirement for human $\gamma\delta$ TCR triggering. As in mice, nonclassical MHC class Ib molecules are a prominent class of antigens recognized by human $\gamma\delta$ T cells, primarily of the V δ 1⁺ subset.^{45–47} Since most of the identified MHC class Ib ligands recognized by V δ 1⁺ T cells are lipid-presenting molecules, we chose to focus on the well-characterized V γ 4V δ 1 TCR DP10.7, which recognizes sulfatide lipids presented by the nonclassical MHC I molecule CD1d.⁴⁸ We expressed a previously described⁴⁸ CD1d SCD construct in CHO cells, and used this as a template to generate elongated versions of CD1d by insertion of the 2-IgSF ectodomain of mouse CD2 (CD1d-CD2) and the 4-IgSF ectodomain of mouse CD4 (CD1d-CD4) into the CD1d SCD membrane-proximal stalk (Figures 7A and S1A). CHO cell transductants were sorted for comparable cell-surface expression levels and exogenously loaded with soluble sulfatide lipid (24:1 acyl chain). We confirmed comparable sulfatide loading of CD1d constructs by labeling cells with a fluorescently tagged DP10.7 TCR tetramer and analyzed surface staining by flow cytometry (Figure 7B). DP10.7 TCR triggering in response to sulfatide-loaded CD1d constructs was assessed using TCR β -chain-deficient human Jurkat T cells (J.RT3-T3.5) stably transduced with DP10.7 TCR (DP10.7 Jurkat T cells), as described previously.⁴⁸ As with murine $\gamma\delta$ TCRs, the binding-induced conformational change in CD3 ϵ was absent following engagement of DP10.7 TCR by cell-expressed sulfatide/CD1d

or by soluble sulfatide-loaded CD1d tetramers, as assessed by Nck SH3.1 pull-down and TCR ζ immunoblot (Figures S9A and S9B). Despite this, DP10.7 TCR was robustly phosphorylated in response to cell-expressed sulfatide-CD1d (Figures 7C and 7D), resulting in downstream LAT phosphorylation (Figures 7C and 7E) and resulting in T cell activation as measured by CD69 upregulation (Figures 7F and S9C). However, TCR triggering and T cell activation was drastically attenuated by CD1d elongation, demonstrating that the small size of CD1d was critically important for effective TCR triggering (Figures 7A–7F and S9C). This was not due to impaired TCR engagement, as DP10.7 Jurkat T cells formed comparable levels of antigen-induced conjugates with CHO cells presenting sulfatide-loaded CD1d and elongated forms of CD1d, as measured by a flow-cytometry-based adhesion assay (Figure 7G).

To assess whether the size of the CD45 ectodomain affected human $\gamma\delta$ TCR triggering, we made a human CD45 chimera, similar in design to our mouse CD45 constructs, in which the native CD45 ectodomain was replaced with that of rat Thy1 (Thy1-hCD45) (Figures 7H and S1A). We also generated expression constructs for full-length native human CD45 (WT-hCD45) and a phosphatase-inactivated mutant of Thy1-hCD45 (Thy1-hCD45*) (Figure 7H). All constructs contained an N-terminal FLAG tag for sorting and immunodetection (Figure 7H). DP10.7 Jurkat T cell transductants that stably expressed CD45 constructs were labeled with an anti-FLAG antibody and sorted for comparable surface expression levels (Figure 7I). Transductants were also checked for comparable TCR and CD45 surface levels (Figure S9D). TCR triggering and DP10.7 Jurkat T cell activation, as measured by TCR ζ phosphorylation (Figures 7J and 7K) and CD69 upregulation (Figures 7L and S9E), respectively, was

Figure 7. Triggering of human $\gamma\delta$ TCR DP10.7 by sulfatide-CD1d requires phosphatase segregation

- (A) Schematic of single-chain constructs of human CD1d and elongated forms of CD1d incorporating membrane-proximal mouse CD2 and CD4 spacers.
- (B) Fluorescence histograms showing cell-surface expression levels of sulfatide-loaded CD1d chimeras in CHO cell transductants. Sulfatide/CD1d complexes were detected with cognate DP10.7 TCR tetramer conjugated with APC. Results are representative of four independent experiments.
- (C) Immunoblot of indicated tyrosine-phosphorylated TCR proximal signaling components (pTCR- ζ and pLAT) following 60-s contact at 37°C with CHO cells expressing the indicated CD1d constructs. Results are representative of three independent experiments.
- (D and E) Quantitation of TCR (D) and LAT (E) phosphorylation from blots as in (C). Data are presented as ratios of normalized pTCR ζ or pLAT density over corresponding normalized TCR density for each lane. R.U., relative units. $n = 3$; data are means \pm SD.
- (F) Activation of DP10.7 Jurkat T cells co-cultured with CHO cells expressing the indicated constructs for 4 h at 37°C, depicted as percentage of CD69-positive cells, as measured by flow cytometry. $n = 5$; data are means \pm SD.
- (G) Conjugate formation, as a measure of cell-cell adhesion, between fluorescently labeled Jurkat T cells expressing the sulfatide/CD1d-specific TCR DP10.7 (CMFDA) and CHO cells expressing the indicated CD1d chimeras loaded with sulfatide (CellTracker Deep Red). Data are pooled from three independent experiments and shown as means \pm SD.
- (H) Schematic of expression constructs of wild-type human CD45 (WT-hCD45) and a chimera of the CD45 endodomain fused to the ectodomain of rat Thy-1 (Thy1-hCD45), depicted approximately to scale. Also shown is a chimera of a catalytically inactive human CD45 endodomain mutant fused to the Thy-1 ectodomain (Thy1-hCD45*). All constructs contain an N-terminal FLAG tag.
- (I) Fluorescence histograms of cell-surface expression levels of the indicated CD45 chimeras in DP10.7 Jurkat T cell transductants sorted for comparable surface expression.
- (J) Immunoblot of tyrosine-phosphorylated TCR (pTCR ζ) in DP10.7 Jurkat T cell transductants following 60-s contact at 37°C with CHO cells expressing CD1d or with untransfected CHO cells as a control (ntCHO). Also shown are Jurkat T cell transductants incubated for 60 s at 37°C in medium alone as a baseline control. TCR ζ and β -actin were blotted as loading controls.
- (K) Quantitation of TCR phosphorylation from blots as in (J). Data are presented as normalized ratios of normalized pTCR ζ density over corresponding normalized TCR density for each lane. R.U., relative units. $n = 3$; data are means \pm SD.
- (L) CD69 upregulation, as measured by flow cytometry, of DP10.7 Jurkat T cell transductants expressing the indicated hCD45 constructs, after 4-h co-culture with CHO cells presenting the sulfatide-loaded CD1d. Results are presented as percentage change in CD69 surface levels relative to unstimulated cells (% Δ CD69). $n = 3$; data are means \pm SD.
- (M) Ripley's H cross-correlation between endogenous TCR and transduced CD45 chimeras at synapses of indicated DP10.7 Jurkat T cell transductants. For WT-CD45 $n = 93$ ROIs (from 15 synapses), and for Thy1-CD45 $n = 33$ ROIs (from 11 synapses), pooled from three independent experiments.

*** $p < 0.0001$, ** $p < 0.001$, * $p < 0.01$; ns, not significant ($p > 0.05$); p values are corrected for all pairwise comparisons.

unaffected by expression of WT-hCD45 at ~6% of endogenous CD45 levels (Table S1). In marked contrast, TCR triggering and T cell activation was almost completely abrogated in DP10.7 Jurkat T cells expressing the truncated Thy1-hCD45 construct at ~5% of endogenous CD45 levels (Figures 7J and 7L; Table S1). In contrast, TCR triggering and T cell activation was unaffected by catalytically inactive Thy1-hCD45*, despite expression at more than twice the levels of Thy1-hCD45 (~11% of endogenous CD45). Like endogenous CD45, transduced WT-hCD45 remained segregated from TCR at DP10.7 Jurkat T cell synapses with CD1d-sulfatide-containing SLBs, as determined by dSTORM imaging (Figure S9F). Spatial point cross-correlation analysis of TCR/WT-hCD45 localizations using Ripley's H function revealed negative values at distances less than ~400 nm, indicating lateral segregation of WT-hCD45 from TCR at approximately receptor-level length scales (Figure 7M). In contrast, Ripley's H function for TCR/Thy1-hCD45 approximated zero at all length scales, representing a loss of TCR/CD45 segregation (Figure 7M). Taken together, these results demonstrate that the large ectodomain of human CD45 is necessary for effective segregation from engaged DP10.7 TCR and is required for stable ligand-induced TCR phosphorylation at synaptic contacts.

DISCUSSION

Here, we identify size-based steric segregation of engaged TCRs from large T cell surface tyrosine phosphatases CD45 and CD148 as a critical requirement for $\gamma\delta$ TCR triggering. This is in keeping with the K-S model of TCR triggering,¹⁵ which does not depend on binding-induced mechanical forces, conformational changes, or co-receptor-mediated aggregation but only requires that membrane-tethered cognate ligands are small in size relative to the large ectodomains of T cell surface tyrosine phosphatases.

We show in two well-characterized $\gamma\delta$ TCR/ligand pairs, murine G8/T22¹⁷ and human DP10.7/sulfatide-CD1d,⁴⁸ that increasing phosphatase access to engaged TCRs abrogates triggering. Engagement of the G8 $\gamma\delta$ TCR by elongated T22 increases intermembrane distance of apposed plasma membranes at T cell synaptic contacts. Despite effective TCR engagement by elongated T22, loss of close contacts abolishes CD45 segregation from engaged TCRs and abrogates TCR triggering. While we show that ligand elongation does not affect overall TCR binding, it remained possible that engagement by elongated ligands held TCRs in orientations unfavorable for triggering. To address this, we increased the flexibility of elongated T22 to enable greater degrees of freedom for TCR engagement. This did not rescue TCR triggering, as would be expected if TCR binding were aberrantly constrained in unfavorable orientations. Moreover, we show that $\gamma\delta$ TCR triggering in response to native-sized T22 and sulfatide-CD1d is abrogated by expression of ectodomain-truncated phosphatases in T cells, where the TCR-ligand interaction is unperturbed, hence ruling out inadvertent disruption of binding-induced mechanical forces or conformational changes. Our findings, however, do not preclude the involvement of conformational changes or mechanical forces in $\gamma\delta$ TCR signal transduction. We envisage that such processes

would complement the core K-S triggering mechanism that we identify here for murine and human TCRs specific for MHC class Ib ligands. For instance, mechanical forces may increase antigen sensitivity through amplifying TCR-evoked proximal signals or enhance antigen specificity by sensing binding-induced force signatures of cognate ligands.⁴⁹ Our results raise the possibility that other $\gamma\delta$ TCRs that recognize small membrane-tethered ligands may be similarly triggered according to K-S principles. Further mechanistic investigation of diverse $\gamma\delta$ TCRs is warranted in this regard.

Interestingly, in contrast to $\alpha\beta$ T cells, artificial aggregation of G8 or DP10.7 TCRs by soluble T22 or sulfatide-CD1d tetramers fails to activate $\gamma\delta$ T cells, suggesting that ligand-induced oligomerization alone is insufficient to trigger $\gamma\delta$ TCRs. Strict reliance on the K-S mechanism for $\gamma\delta$ T cell antigen sensing, especially in the absence of co-receptor-mediated signal amplification,⁵⁰ likely reflects a higher signaling threshold for $\gamma\delta$ T cell activation. This may be important for calibrating $\gamma\delta$ T cell antigen sensitivity to the relatively higher levels of basal MHC class Ib ligands on cell surfaces in comparison to the handful of cognate pMHC ligands typically displayed on antigen-presenting cells. Similarly, our finding that Csk downmodulation had no impact on $\gamma\delta$ TCR triggering suggests that stress-induced upregulation of abundant nonpolymorphic ligands on cell surfaces obviates the need for Csk-mediated fine-tuning of $\gamma\delta$ TCR signaling thresholds to adjust for variability in ligand potency.²⁹

Structural studies have revealed substantial variability in $\gamma\delta$ TCR docking angles and ligand-binding topology, in contrast to the stereotypical end-to-end orientation and "diagonal" binding mode of $\alpha\beta$ TCRs to cognate pMHC ligands.⁵¹ Both the murine G8 TCR and the human DP10.7 TCR bind their MHC class Ib ligands predominantly with their δ chains,^{17,48} while some MR1-restricted $\gamma\delta$ TCRs bind to the MR1 $\alpha 3$ domain, below the antigen-presenting platform.⁵² This surprising flexibility in ligand binding, free from the constraints imposed by peptide recognition or co-receptor engagement, suggests that effective $\gamma\delta$ TCR triggering is indifferent to the site and orientation of binding to cognate ligands as long as TCR engagement takes place in synaptic close-contact zones,⁵³ from which phosphatases are excluded. This B cell receptor-like recognition of membrane-tethered invariant antigens is reminiscent of antigen targeting by chimeric antigen receptors (CARs). CARs employ small antibody fragments for targeting extracellular tumor antigens, fused to ITAM-containing cytoplasmic domains,⁵⁴ fulfilling conditions for triggering according to K-S principles. In support of this, CAR triggering has recently been shown to be dependent on compact CAR and antigen dimensions.⁵⁵

Finally, our findings raise the possibility that the K-S mechanism may also be involved in TCR triggering in human V γ 9V δ 2 T cells. These $\gamma\delta$ T cells are activated by exposure to phosphorylated isoprenoid metabolites (PiPs),⁴ although the mechanism by which PiPs activate V γ 9V δ 2 T cells remains unclear. V γ 9V δ 2⁺ T cells require contact with accessory cells for activation,⁵⁶ and CD45 is depleted at synaptic contacts.⁵⁷ Recently, the small cell-surface glycoprotein BTN2A1, a member of the B7 receptor family, was identified as a ligand for V γ 9V δ 2⁺ T cells.^{58,59} BTN2A1, which possesses a small 2-IgSF ectodomain, directly engages the TCR and may therefore mediate

TCR triggering, in part, by trapping TCR in close-contact zones from which T cell surface phosphatases have been excluded.

Limitations of the study

We show that Src-kinase-dependent $\gamma\delta$ TCR triggering is dependent on the small size of its membrane-tethered ligands and also requires the large and bulky ectodomains of T cell surface phosphatases CD45 and CD148, which are segregated from engaged TCRs at synaptic contacts. We use murine T22 and human CD1d as model antigens, since nonclassical MHC class I molecules constitute a major class of ligands for $\gamma\delta$ TCRs. However, our studies do not directly address whether triggering conforms to K-S principles in the special case of human V γ 9V δ 2 T cells, which are co-activated by soluble prenyl phosphates and small cell-surface-expressed butyrophilins. While we show that size manipulations of both ligands and CD45/CD148 drastically affect triggering, our inability to concurrently match TCR/CD45 distributions to synaptic topography is limiting and will benefit from correlative optical and electron microscopy approaches for more definitive characterization of molecular segregation. Moreover, we make intermembrane measurements from embedded sections, which may be prone to fixation/dehydration and sectioning artifacts. More accurate measurements using cryoelectron tomography may allow the size, structure, and orientation of TCR/ligand complexes at synaptic contacts to be directly resolved. To probe TCR/CD45 distributions at receptor-level length scales, we have performed dSTORM nanoscopy, necessarily on well-fixed cells, in part to satisfy the requirement of stationarity for accurate localizations. Emerging super-resolved imaging techniques for low-photon-dose live-cell imaging may more accurately reveal molecular-level organization and, importantly, dynamics, without potential fixation artifacts. While current evidence disfavors mechanotransduction in $\gamma\delta$ TCR triggering, our findings do not rule out as yet unidentified forces acting on the triggering process. In this respect, actomyosin coupling to $\gamma\delta$ TCR signaling warrants further investigation.

RESOURCE AVAILABILITY

Lead contact

Further information and requests for resources and reagents should be directed to and will be fulfilled by the lead contact, Kaushik Choudhuri (kaushik.choudhuri@biochemistry.utah.edu).

Materials availability

Further requests for resources and reagents generated in this report should be directed to and will be fulfilled by the [lead contact](#).

Data and code availability

- The data figures supporting the findings of this study are available within the article and its supplementary materials. Associated data tables can be shared in shared by the [lead contact](#) upon request.
- This paper does not employ original code.
- Any additional information required to reanalyze the data reported in this work is available from the [lead contact](#) upon request.

ACKNOWLEDGMENTS

We thank Y.H. Chien (Stanford University) for the generous gifts of mAb 7H9, G8 hybridoma, and the *tcrG8rag*^{-/-} *Balb/c* mice, Luc Van Kaer (Vanderbilt University) for kindly providing KN6 hybridomas, and Dr. Marilia

Cascahlo (University of Michigan) for the gift of QM transgenic mice. This work was supported by NIH grants K99AI093884, R00AI093884, and R01AI134999 and University of Utah start-up funds to K.C., grant NIH R01AI155984 to E.J.A., and an MRC program grant (G9722488) and Wellcome Trust Senior Investigator Award (101799/Z/13/Z) to P.A.v.d.M. We thank the University of Michigan Biomedical Research Core Facilities and Rogel Cancer Center (NCI award P30CA046592) for support with microscopy and flow-cytometry/cell-sorting resources. The following reagents were obtained through the NIH Tetramer Core Facility: T22 and sulfatide/CD1d tetramers, and monobiotinylated T22 and biotinylated CD1d monomers.

AUTHOR CONTRIBUTIONS

K.C. and P.A.v.d.M. conceived the study. K.C. and P.A.v.d.M. designed the study. F.L., K.C., and J.N. performed experiments. K.G. made T22 constructs. E.J.A. and S.R. made critical reagents and advised on study design for CD1d experiments. K.C. and F.L. wrote the manuscript draft. All authors contributed to editing the final manuscript.

DECLARATION OF INTERESTS

E.J.A. declares consultancy with Laguna Therapeutics, TcBioPharm, and Notch on $\gamma\delta$ T cell immunotherapy development.

STAR★METHODS

Detailed methods are provided in the online version of this paper and include the following:

- **KEY RESOURCES TABLE**
- **EXPERIMENTAL MODEL AND STUDY PARTICIPANT DETAILS**
 - Mice
 - Cells
- **METHOD DETAILS**
 - Recombinant expression constructs and siRNA vectors
 - Cell transfection and transduction
 - Flow cytometry and cell sorting
 - Cell isolation and enrichment
 - DP10.7 tetramer production
 - T cell activation assay
 - Adhesion assay
 - Biochemistry
 - Detection of CD3 ϵ conformational change using APA1/1 antibody and flow cytometry
 - Flow cytometry of intracellular phosphoproteins
 - TCR downregulation assay
 - Supported lipid bilayers
 - Intracellular Ca²⁺ imaging and analysis
 - Confocal fluorescence microscopy
 - dSTORM sample preparation & imaging
 - dSTORM image processing
 - Transmission electron microscopy
- **QUANTIFICATION AND STATISTICAL ANALYSIS**

SUPPLEMENTAL INFORMATION

Supplemental information can be found online at <https://doi.org/10.1016/j.celrep.2024.114761>.

Received: October 31, 2023

Revised: March 21, 2024

Accepted: August 29, 2024

REFERENCES

- Papotto, P.H., Ribot, J.C., and Silva-Santos, B. (2017). IL-17(+) gamma-delta T cells as kick-starters of inflammation. *Nat. Immunol.* 18, 604–611. <https://doi.org/10.1038/ni.3726>.
- Junqueira, C., Polidoro, R.B., Castro, G., Absalon, S., Liang, Z., Sen-Santara, S., Crespo, A., Pereira, D.B., Gazzinelli, R.T., Dvorin, J.D., and Lieberman, J. (2021). gamma-delta T cells suppress Plasmodium falciparum blood-stage infection by direct killing and phagocytosis. *Nat. Immunol.* 22, 347–357. <https://doi.org/10.1038/s41590-020-00847-4>.
- Chien, Y.H., Meyer, C., and Bonneville, M. (2014). gamma-delta T cells: first line of defense and beyond. *Annu. Rev. Immunol.* 32, 121–155. <https://doi.org/10.1146/annurev-immunol-032713-120216>.
- Castro, C.D., Boughter, C.T., Broughton, A.E., Ramesh, A., and Adams, E.J. (2020). Diversity in recognition and function of human gamma-delta T cells. *Immunol. Rev.* 298, 134–152. <https://doi.org/10.1111/imr.12930>.
- Strominger, J.L. (1989). The gamma delta T cell receptor and class Ib MHC-related proteins: enigmatic molecules of immune recognition. *Cell* 57, 895–898. [https://doi.org/10.1016/0092-8674\(89\)90326-7](https://doi.org/10.1016/0092-8674(89)90326-7).
- Hayes, S.M., and Love, P.E. (2006). Stoichiometry of the murine gamma-delta T cell receptor. *J. Exp. Med.* 203, 47–52. <https://doi.org/10.1084/jem.20051886>.
- Siegers, G.M., Swamy, M., Fernández-Malavé, E., Minguet, S., Rathmann, S., Guardo, A.C., Pérez-Flores, V., Regueiro, J.R., Alarcón, B., Fisch, P., and Schamel, W.W.A. (2007). Different composition of the human and the mouse gamma-delta T cell receptor explains different phenotypes of CD3gamma and CD3delta immunodeficiencies. *J. Exp. Med.* 204, 2537–2544. <https://doi.org/10.1084/jem.20070782>.
- Kersh, E.N., Shaw, A.S., and Allen, P.M. (1998). Fidelity of T cell activation through multistep T cell receptor zeta phosphorylation. *Science* 281, 572–575. <https://doi.org/10.1126/science.281.5376.572>.
- Choudhuri, K., and van der Merwe, P.A. (2007). Molecular mechanisms involved in T cell receptor triggering. *Semin. Immunol.* 19, 255–261. <https://doi.org/10.1016/j.smim.2007.04.005>.
- Gil, D., Schamel, W.W.A., Montoya, M., Sánchez-Madrid, F., and Alarcón, B. (2002). Recruitment of Nck by CD3 epsilon reveals a ligand-induced conformational change essential for T cell receptor signaling and synapse formation. *Cell* 109, 901–912. [https://doi.org/10.1016/S0092-8674\(02\)00799-7](https://doi.org/10.1016/S0092-8674(02)00799-7).
- Dopfer, E.P., Hartl, F.A., Oberg, H.H., Siegers, G.M., Yousefi, O.S., Kock, S., Fiala, G.J., Garcillán, B., Sandstrom, A., Alarcón, B., et al. (2014). The CD3 conformational change in the gamma-delta T cell receptor is not triggered by antigens but can be enforced to enhance tumor killing. *Cell Rep.* 7, 1704–1715. <https://doi.org/10.1016/j.celrep.2014.04.049>.
- Das, D.K., Feng, Y., Mallis, R.J., Li, X., Keskin, D.B., Hussey, R.E., Brady, S.K., Wang, J.H., Wagner, G., Reinherz, E.L., and Lang, M.J. (2015). Force-dependent transition in the T-cell receptor beta-subunit allosterically regulates peptide discrimination and pMHC bond lifetime. *Proc. Natl. Acad. Sci. USA* 112, 1517–1522. <https://doi.org/10.1073/pnas.1424829112>.
- Mallis, R.J., Duke-Cohan, J.S., Das, D.K., Akitsu, A., Luoma, A.M., Banik, D., Stephens, H.M., Tetteh, P.W., Castro, C.D., Krahne, S., et al. (2021). Molecular design of the gamma-delta T cell receptor ectodomain encodes biologically fit ligand recognition in the absence of mechanosensing. *Proc. Natl. Acad. Sci. USA* 118, e2023050118. <https://doi.org/10.1073/pnas.2023050118>.
- Pennington, D.J., Silva-Santos, B., and Hayday, A.C. (2005). Gamma-delta T cell development—having the strength to get there. *Curr. Opin. Immunol.* 17, 108–115. <https://doi.org/10.1016/j.coi.2005.01.009>.
- Davis, S.J., and van der Merwe, P.A. (2006). The kinetic-segregation model: TCR triggering and beyond. *Nat. Immunol.* 7, 803–809. <https://doi.org/10.1038/ni1369>.
- Nika, K., Soldani, C., Salek, M., Paster, W., Gray, A., Etzensperger, R., Fugger, L., Polzella, P., Cerundolo, V., Dushek, O., et al. (2010). Constitutively active Lck kinase in T cells drives antigen receptor signal transduction. *Immunity* 32, 766–777. <https://doi.org/10.1016/j.immuni.2010.05.011>.
- Adams, E.J., Chien, Y.H., and Garcia, K.C. (2005). Structure of a gamma-delta T cell receptor in complex with the nonclassical MHC T22. *Science* 308, 227–231. <https://doi.org/10.1126/science.1106885>.
- Bonneville, M., Ito, K., Krecko, E.G., Itoharu, S., Kappes, D., Ishida, I., Kanagawa, O., Janeway, C.A., Murphy, D.B., and Tonegawa, S. (1989). Recognition of a self major histocompatibility complex TL region product by gamma delta T-cell receptors. *Proc. Natl. Acad. Sci. USA* 86, 5928–5932. <https://doi.org/10.1073/pnas.86.15.5928>.
- Adams, E.J., Strop, P., Shin, S., Chien, Y.H., and Garcia, K.C. (2008). An autonomous CDR3delta is sufficient for recognition of the nonclassical MHC class I molecules T10 and T22 by gamma-delta T cells. *Nat. Immunol.* 9, 777–784. <https://doi.org/10.1038/ni.1620>.
- Zeng, X., Meyer, C., Huang, J., Newell, E.W., Kidd, B.A., Wei, Y.L., and Chien, Y.H. (2014). Gamma delta T cells recognize haptens and mount a hapten-specific response. *Elife* 3, e03609. <https://doi.org/10.7554/eLife.03609>.
- Bluestone, J.A., Cron, R.Q., Cotterman, M., Houlden, B.A., and Matis, L.A. (1988). Structure and specificity of T cell receptor gamma/delta on major histocompatibility complex antigen-specific CD3+, CD4-CD8- T lymphocytes. *J. Exp. Med.* 168, 1899–1916. <https://doi.org/10.1084/jem.168.5.1899>.
- Schild, H., Mavaddat, N., Litzenberger, C., Ehrlich, E.W., Davis, M.M., Bluestone, J.A., Matis, L., Draper, R.K., and Chien, Y.H. (1994). The nature of major histocompatibility complex recognition by gamma delta T cells. *Cell* 76, 29–37. [https://doi.org/10.1016/0092-8674\(94\)90170-8](https://doi.org/10.1016/0092-8674(94)90170-8).
- Risueno, R.M., Gil, D., Fernandez, E., Sanchez-Madrid, F., and Alarcon, B. (2005). Ligand-induced conformational change in the T-cell receptor associated with productive immune synapses. *Blood* 106, 601–608. <https://doi.org/10.1182/blood-2004-12-4763>.
- Choudhuri, K., Wiseman, D., Brown, M.H., Gould, K., and van der Merwe, P.A. (2005). T-cell receptor triggering is critically dependent on the dimensions of its peptide-MHC ligand. *Nature* 436, 578–582. <https://doi.org/10.1038/nature03843>.
- Choudhuri, K., Parker, M., Milicic, A., Cole, D.K., Shaw, M.K., Sewell, A.K., Stewart-Jones, G., Dong, T., Gould, K.G., and van der Merwe, P.A. (2009). Peptide-major histocompatibility complex dimensions control proximal kinase-phosphatase balance during T cell activation. *J. Biol. Chem.* 284, 26096–26105. <https://doi.org/10.1074/jbc.M109.039966>.
- Trinh, R., Gurbaxani, B., Morrison, S.L., and Seyfzadeh, M. (2004). Optimization of codon pair use within the (GGGG)3 linker sequence results in enhanced protein expression. *Mol. Immunol.* 40, 717–722. <https://doi.org/10.1016/j.molimm.2003.08.006>.
- van Rosmalen, M., Krom, M., and Merckx, M. (2017). Tuning the Flexibility of Glycine-Serine Linkers To Allow Rational Design of Multidomain Proteins. *Biochemistry* 56, 6565–6574. <https://doi.org/10.1021/acs.biochem.7b00902>.
- Valitutti, S., Müller, S., Cella, M., Padovan, E., and Lanzavecchia, A. (1995). Serial triggering of many T-cell receptors by a few peptide-MHC complexes. *Nature* 375, 148–151. <https://doi.org/10.1038/375148a0>.
- Courtney, A.H., Shvets, A.A., Lu, W., Griffante, G., Mollenauer, M., Horikova, V., Lo, W.L., Yu, S., Stepanek, O., Chakraborty, A.K., and Weiss, A. (2019). CD45 functions as a signaling gatekeeper in T cells. *Sci. Signal.* 12, eaaw8151. <https://doi.org/10.1126/scisignal.aaw8151>.
- Bergman, M., Mustelin, T., Oetken, C., Partanen, J., Flint, N.A., Amrein, K.E., Autero, M., Burn, P., and Alitalo, K. (1992). The human p50csk tyrosine kinase phosphorylates p56lck at Tyr-505 and down regulates its catalytic activity. *EMBO J.* 11, 2919–2924. <https://doi.org/10.1002/j.1460-2075.1992.tb05361.x>.

31. Aricescu, A.R., Siebold, C., Choudhuri, K., Chang, V.T., Lu, W., Davis, S.J., van der Merwe, P.A., and Jones, E.Y. (2007). Structure of a tyrosine phosphatase adhesive interaction reveals a spacer-clamp mechanism. *Science* 317, 1217–1220. <https://doi.org/10.1126/science.1144646>.
32. Vardhana, S., Choudhuri, K., Varma, R., and Dustin, M.L. (2010). Essential role of ubiquitin and TSG101 protein in formation and function of the central supramolecular activation cluster. *Immunity* 32, 531–540. <https://doi.org/10.1016/j.immuni.2010.04.005>.
33. Varma, R., Campi, G., Yokosuka, T., Saito, T., and Dustin, M.L. (2006). T cell receptor-proximal signals are sustained in peripheral microclusters and terminated in the central supramolecular activation cluster. *Immunity* 25, 117–127. <https://doi.org/10.1016/j.immuni.2006.04.010>.
34. McCall, M.N., Shotton, D.M., and Barclay, A.N. (1992). Expression of soluble isoforms of rat CD45. Analysis by electron microscopy and use in epitope mapping of anti-CD45R monoclonal antibodies. *Immunology* 76, 310–317.
35. Cyster, J.G., Shotton, D.M., and Williams, A.F. (1991). The dimensions of the T lymphocyte glycoprotein leukosialin and identification of linear protein epitopes that can be modified by glycosylation. *EMBO J.* 10, 893–902. <https://doi.org/10.1002/j.1460-2075.1991.tb08022.x>.
36. Cordoba, S.P., Choudhuri, K., Zhang, H., Bridge, M., Basat, A.B., Dustin, M.L., and van der Merwe, P.A. (2013). The large ectodomains of CD45 and CD148 regulate their segregation from and inhibition of ligated T-cell receptor. *Blood* 121, 4295–4302. <https://doi.org/10.1182/blood-2012-07-442251>.
37. Rossy, J., Cohen, E., Gaus, K., and Owen, D.M. (2014). Method for co-cluster analysis in multichannel single-molecule localisation data. *Histochem. Cell Biol.* 141, 605–612. <https://doi.org/10.1007/s00418-014-1208-z>.
38. Bates, M., Jones, S.A., and Zhuang, X. (2013). Stochastic optical reconstruction microscopy (STORM): a method for superresolution fluorescence imaging. *Cold Spring Harb. Protoc.* 2013, 498–520. <https://doi.org/10.1101/pdb.top075143>.
39. Culley, S., Albrecht, D., Jacobs, C., Pereira, P.M., Leterrier, C., Mercer, J., and Henriques, R. (2018). Quantitative mapping and minimization of super-resolution optical imaging artifacts. *Nat. Methods* 15, 263–266. <https://doi.org/10.1038/nmeth.4605>.
40. Dempsey, G.T., Vaughan, J.C., Chen, K.H., Bates, M., and Zhuang, X. (2011). Evaluation of fluorophores for optimal performance in localization-based super-resolution imaging. *Nat. Methods* 8, 1027–1036. <https://doi.org/10.1038/nmeth.1768>.
41. Kiskowski, M.A., Hancock, J.F., and Kenworthy, A.K. (2009). On the use of Ripley's K-function and its derivatives to analyze domain size. *Biophys. J.* 97, 1095–1103. <https://doi.org/10.1016/j.bpj.2009.05.039>.
42. Kennedy, P.R., Barthen, C., Williamson, D.J., Pitkeathly, W.T.E., Hazime, K.S., Cumming, J., Stacey, K.B., Hilton, H.G., Carrington, M., Parham, P., and Davis, D.M. (2019). Genetic diversity affects the nanoscale membrane organization and signaling of natural killer cell receptors. *Sci. Signal.* 12, eaaw9252. <https://doi.org/10.1126/scisignal.aaw9252>.
43. Dustin, M.L., and Springer, T.A. (1989). T-cell receptor cross-linking transiently stimulates adhesiveness through LFA-1. *Nature* 341, 619–624. <https://doi.org/10.1038/341619a0>.
44. Tabdanov, E., Gondarenko, S., Kumari, S., Liapis, A., Dustin, M.L., Sheetz, M.P., Kam, L.C., and Iskratsch, T. (2015). Micropatterning of TCR and LFA-1 ligands reveals complementary effects on cytoskeleton mechanics in T cells. *Integr. Biol.* 7, 1272–1284. <https://doi.org/10.1039/c5ib00032g>.
45. Willcox, C.R., Pitard, V., Netzer, S., Couzi, L., Salim, M., Silberzahn, T., Moreau, J.F., Hayday, A.C., Willcox, B.E., and Déchanet-Merville, J. (2012). Cytomegalovirus and tumor stress surveillance by binding of a human gamma delta T cell antigen receptor to endothelial protein C receptor. *Nat. Immunol.* 13, 872–879. <https://doi.org/10.1038/ni.2394>.
46. Bai, L., Picard, D., Anderson, B., Chaudhary, V., Luoma, A., Jabri, B., Adams, E.J., Savage, P.B., and Bendelac, A. (2012). The majority of CD1d-sulfatide-specific T cells in human blood use a semiinvariant Vdelta1 TCR. *Eur. J. Immunol.* 42, 2505–2510. <https://doi.org/10.1002/eji.201242531>.
47. Roy, S., Ly, D., Castro, C.D., Li, N.S., Hawk, A.J., Altman, J.D., Meredith, S.C., Piccirilli, J.A., Moody, D.B., and Adams, E.J. (2016). Molecular Analysis of Lipid-Reactive Vdelta1 gamma delta T Cells Identified by CD1c Tetramers. *J. Immunol.* 196, 1933–1942. <https://doi.org/10.4049/jimmunol.1502202>.
48. Luoma, A.M., Castro, C.D., Mayassi, T., Bembinster, L.A., Bai, L., Picard, D., Anderson, B., Scharf, L., Kung, J.E., Sibener, L.V., et al. (2013). Crystal structure of Vdelta1 T cell receptor in complex with CD1d-sulfatide shows MHC-like recognition of a self-lipid by human gamma delta T cells. *Immunity* 39, 1032–1042. <https://doi.org/10.1016/j.immuni.2013.11.001>.
49. Choi, H.K., Cong, P., Ge, C., Natarajan, A., Liu, B., Zhang, Y., Li, K., Rushdi, M.N., Chen, W., Lou, J., et al. (2023). Catch bond models may explain how force amplifies TCR signaling and antigen discrimination. *Nat. Commun.* 14, 2616. <https://doi.org/10.1038/s41467-023-38267-1>.
50. Jiang, N., Huang, J., Edwards, L.J., Liu, B., Zhang, Y., Beal, C.D., Evavold, B.D., and Zhu, C. (2011). Two-stage cooperative T cell receptor-peptide major histocompatibility complex-CD8 trimolecular interactions amplify antigen discrimination. *Immunity* 34, 13–23. <https://doi.org/10.1016/j.immuni.2010.12.017>.
51. Garcia, K.C., Teyton, L., and Wilson, I.A. (1999). Structural basis of T cell recognition. *Annu. Rev. Immunol.* 17, 369–397. <https://doi.org/10.1146/annurev.immunol.17.1.369>.
52. Le Nours, J., Gherardin, N.A., Ramarathnam, S.H., Awad, W., Wiede, F., Gully, B.S., Khandokar, Y., Praveena, T., Wubben, J.M., Sandow, J.J., et al. (2019). A class of gamma delta T cell receptors recognize the underside of the antigen-presenting molecule MR1. *Science* 366, 1522–1527. <https://doi.org/10.1126/science.aav3900>.
53. Chang, V.T., Fernandes, R.A., Ganzinger, K.A., Lee, S.F., Siebold, C., McColl, J., Jönsson, P., Palayret, M., Harlos, K., Coles, C.H., et al. (2016). Initiation of T cell signaling by CD45 segregation at 'close contacts'. *Nat. Immunol.* 17, 574–582. <https://doi.org/10.1038/ni.3392>.
54. June, C.H., O'Connor, R.S., Kawalekar, O.U., Ghassemi, S., and Milone, M.C. (2018). CAR T cell immunotherapy for human cancer. *Science* 359, 1361–1365. <https://doi.org/10.1126/science.aar6711>.
55. Xiao, Q., Zhang, X., Tu, L., Cao, J., Hinrichs, C.S., and Su, X. (2022). Size-dependent activation of CAR-T cells. *Sci. Immunol.* 7, eabl3995. <https://doi.org/10.1126/sciimmunol.abl3995>.
56. Morita, C.T., Beckman, E.M., Bukowski, J.F., Tanaka, Y., Band, H., Bloom, B.R., Golan, D.E., and Brenner, M.B. (1995). Direct presentation of non-peptide prenyl pyrophosphate antigens to human gamma delta T cells. *Immunity* 3, 495–507. [https://doi.org/10.1016/1074-7613\(95\)90178-7](https://doi.org/10.1016/1074-7613(95)90178-7).
57. Favier, B., Espinosa, E., Tabiasco, J., Dos Santos, C., Bonneville, M., Valitutti, S., and Fournié, J.J. (2003). Uncoupling between immunological synapse formation and functional outcome in human gamma delta T lymphocytes. *J. Immunol.* 171, 5027–5033. <https://doi.org/10.4049/jimmunol.171.10.5027>.
58. Rigau, M., Ostrouska, S., Fulford, T.S., Johnson, D.N., Woods, K., Ruan, Z., McWilliam, H.E.G., Hudson, C., Tutuka, C., Wheatley, A.K., et al. (2020). Butyrophilin 2A1 is essential for phosphoantigen reactivity by gamma delta T cells. *Science* 367, eaay5516. <https://doi.org/10.1126/science.aay5516>.
59. Karunakaran, M.M., Willcox, C.R., Salim, M., Paletta, D., Fichtner, A.S., Noll, A., Starick, L., Nohren, A., Begley, C.R., Berwick, K.A., et al. (2020). Butyrophilin-2A1 Directly Binds Germline-Encoded Regions of the Vgamma9Vdelta2 TCR and Is Essential for Phosphoantigen Sensing. *Immunity* 52, 487–498. <https://doi.org/10.1016/j.immuni.2020.02.014>.

60. Cascalho, M., Ma, A., Lee, S., Masat, L., and Wabl, M. (1996). A quasi-monoclonal mouse. *Science* 272, 1649–1652. <https://doi.org/10.1126/science.272.5268.1649>.
61. Scharf, L., Li, N.S., Hawk, A.J., Garzón, D., Zhang, T., Fox, L.M., Kazen, A.R., Shah, S., Haddadian, E.J., Gumperz, J.E., et al. (2010). The 2.5 Å structure of CD1c in complex with a mycobacterial lipid reveals an open groove ideally suited for diverse antigen presentation. *Immunity* 33, 853–862. <https://doi.org/10.1016/j.immuni.2010.11.026>.
62. Lopez-Sagaseta, J., Kung, J.E., Savage, P.B., Gumperz, J., and Adams, E.J. (2012). The molecular basis for recognition of CD1d/alpha-galactosylceramide by a human non-Valpha24 T cell receptor. *PLoS Biol.* 10, e1001412. <https://doi.org/10.1371/journal.pbio.1001412>.
63. Dustin, M.L., Starr, T., Varma, R., and Thomas, V.K. (2007). Supported planar bilayers for study of the immunological synapse. *Curr Protoc Immunol* Chapter 76, 18.13.1–18.13.35. <https://doi.org/10.1002/0471142735.im1813s76>.
64. Ovesny, M., Krizek, P., Borkovec, J., Svindrych, Z., and Hagen, G.M. (2014). ThunderSTORM: a comprehensive ImageJ plug-in for PALM and STORM data analysis and super-resolution imaging. *Bioinformatics* 30, 2389–2390. <https://doi.org/10.1093/bioinformatics/btu202>.
65. Schindelin, J., Arganda-Carreras, I., Frise, E., Kaynig, V., Longair, M., Pietzsch, T., Preibisch, S., Rueden, C., Saalfeld, S., Schmid, B., et al. (2012). Fiji: an open-source platform for biological-image analysis. *Nat. Methods* 9, 676–682. <https://doi.org/10.1038/nmeth.2019>.
66. Baddeley, A., Rubak, E., and Turner, R. (2015). *Spatial Point Patterns: Methodology and Applications with R* (Chapman and Hall/CRC Press).

STAR★METHODS

KEY RESOURCES TABLE

REAGENT or RESOURCE	SOURCE	IDENTIFIER
Antibodies		
Anti-human TCR ζ (phospho Y83)	Abcam	Cat #: ab68236; RRID:AB_11155460
Anti-mouse Lck antibody	Abcam	Cat #: ab3885; RRID:AB_2249950
Anti-mouse/human CD247 (TCR ζ chain)	BD Pharmingen	Cat #: 51-6527GR
Anti-mouse pLCK(Tyr505)	Cell Signaling Technology	Cat #: 2751; RRID:AB_330446
Anti-mouse pSrc(Tyr416)	Cell Signaling Technology	Cat #: 6943; RRID:AB_10013641
Anti-mouse CSK	Cell Signaling Technology	Cat #: 4980; RRID:AB_2276592
Anti-human pLAT (Tyr191)	Cell Signaling Technology	Cat #: 3584; RRID:AB_2157728
Anti- β -actin	Cell Signaling Technology	Cat #: 4970; RRID:AB_2223172
Anti- β -actin	Cell Signaling Technology	Cat #: 3700; RRID:AB_2242334
Anti-Phospho-p44/42 MAPK (Erk1/2) (Thr202/Tyr204)	Cell Signaling Technology	Cat #: 4370; RRID:AB_2315112
Anti-human CD1d	Santa Cruz	Cat #: SC-19632; RRID:AB_626960
IRDye® 680LT Donkey anti-mouse IgG	LI-COR	Cat #: 926-68022; RRID:AB_10715072
IRDye® 800CW Donkey anti-rabbit IgG	LI-COR	Cat #: 926-32213; RRID:AB_621848
Anti-human CD45 Antibody	Biolegend	Cat #: 304002; RRID:AB_314390
Anti-Flag	SIGMA	Cat #: F7425; RRID:AB_439687
Anti-Flag	SIGMA	Cat #: F1804; RRID:AB_262044
Anti-human CD3 Antibody	Biolegend	Cat #: 300438; RRID:AB_11146991
Anti-human CD1d	Biolegend	Cat #: 350302; RRID:AB_10641848
Anti-human/mouse CD3 ϵ (activation epitope)	Biolegend	Cat #: 362701; RRID:AB_2563713
APC/Fire 750 anti-human CD3	Biolegend	Cat #: 344840; RRID:AB_2572114
Pacific Blue anti-human CD69	Biolegend	Cat #: 310920; RRID:AB_493667
Alexa Fluor 647 Goat anti-hamster (Armenian) IgG	Biolegend	Cat #: 405510; RRID:AB_2566695
Brilliant Violet 510™ anti-mouse TCR γ/δ	Biolegend	Cat #: 118131; RRID:AB_2563534
Alexa Fluor 647 F(ab') ₂ -goat anti-mouse IgG (H + L)	Invitrogen/Thermo Fisher Scientific	Cat #: Cat# A-21237; RRID:AB_2535806
F(ab') ₂ anti-mouse IgG (H + L)	Invitrogen/Thermo Fisher Scientific	Cat #: A24508; RRID:AB_2535977
F(ab') ₂ anti-rat IgG (H + L)	Invitrogen/Thermo Fisher Scientific	Cat #: A24551; RRID:AB_2536019
Anti-mouse CD3 ϵ	Biolegend	Cat #: 100340; RRID:AB_11149115
Anti-mouse CD3 ϵ	Biolegend	Cat #: 100202; RRID:AB_312659
Anti-mouse CD45.2	Biolegend	Cat #: 109802; RRID:AB_313439
Anti-mouse IL-2	Biolegend	Cat #: 503704; RRID:AB_315294
Biotin anti-mouse IL-2	Biolegend	Cat #: 503804; RRID:AB_315298
Anti-mouse IFN- γ	Biolegend	Cat #: 505702; RRID:AB_315390
Biotin anti-mouse IFN- γ	Biolegend	Cat #: 505804; RRID:AB_315398
Anti-mouse CD4	Biolegend	Cat #: 100441; RRID:AB_11150580
Anti-mouse CD8 α	Biolegend	Cat #: 100775; RRID:AB_2810325
Anti-T22	Gift from Dr. YS Chien	Clone#: 7h9
eFluor 450 anti-mouse pCD3 ζ (Tyr142)	eBioscience/Thermo Fisher Scientific	Cat #: 48-2478-42; RRID:AB_2866438
PE anti-mouse pLAT (Tyr171)	Biolegend	Cat #: 946605; RRID:AB_2936765
PE anti-mouse CD19	Biolegend	Cat #: 115507; RRID:AB_313642
Anti-mouse CD148	Millipore Sigma	Cat #: MABF2070
Bacterial and virus strains		
One Shot™ OmniMAX™ 2 T1R	Invitrogen	C854003
Chemically Competent E. coli		

(Continued on next page)

Continued

REAGENT or RESOURCE	SOURCE	IDENTIFIER
Chemicals, peptides, and recombinant proteins		
DP10.7 tetramer	This paper	N/A
T22 tetramer	NIH tetramer core	N/A
T22 monomer-biotin	NIH tetramer core	N/A
CD1d tetramer	NIH tetramer core	N/A
CD1d monomer-biotin	NIH tetramer core	N/A
pOVA-I-Ab tetramer	NIH tetramer core	N/A
ICAM-1-His	Sino Biological	Cat#: 50440-M08H
Nck SH3.1	Peptide 2.0	Batch #: 110165-001
Experimental models: Cell lines		
CHO cells	ATCC	CCL-61; RRID:CVCL_0214
G8 T cell hybridoma	Gift from Dr. YS Chien	N/A
Dp10.7 TCR Jurkat T cells	Luoma et al. ⁴⁸	N/A
KN6 T cell hybridoma	Gift from Dr. Luc Van Kaer	N/A
HEK293T	Gift from Dr. Akira Ono	N/A
Experimental models: Organisms/strains		
G8 $\gamma\delta$ TCR transgenic mouse	Gift from Dr. YH Chien	N/A
OT-II transgenic mouse	The Jackson Laboratory	004194; RRID:IMSR_JAX:004194
QM-BCR transgenic mouse	Gift from Dr. Marilia Cascalho	N/A
Oligonucleotides		
T22 constructs, T22 forward: tcgggtggcg gcggctctggtcacactcgcttaggtatttc	Sigma	N/A
T22 constructs, T22 reverse: gaggaagct tcagtcgaagtgacagtaagactcg	Sigma	N/A
T22 constructs, β -2M forward: gatatctc gagtcgcttcagtcgtagcatgg	Sigma	N/A
T22 constructs, β -2M reverse: ccagagc cgccaccgagccgctccgcccgaaccgcca cctcccatgtctgatccagtagac	Sigma	N/A
T22 constructs, BamHI site insertion forward: taatggatcctgcatggaagtgggtgc	Sigma	N/A
T22 constructs, BamHI site insertion reverse: taatggatcctcagtcggcagaacctg	Sigma	N/A
T22 constructs, BamHI site removal single primer: gatgggaggatccgtggattggattgtg	Sigma	N/A
mCD45 constructs, GFP STOP insertion forward: gagcaaggcgagtagctgttcaccgg	IDT	N/A
mCD45 constructs, GFP STOP insertion reverse: ccggtgaacagctactcgccctgtctc	IDT	N/A
hCD45 cDNA amplification forward: ttccagatatgacctgtattt	IDT	N/A
hCD45 cDNA amplification reverse: cctatgaaccttgattaaagctgga	IDT	N/A
hCD45 phosphatase dead mutation forward: tgtgtgcaactccagtgctggtg	IDT	N/A
hCD45 phosphatase dead mutation reverse: atgggaccactgaagaaattgc	IDT	N/A
RT-PCR primer pairs for T22-SCD: atggctcgctcggtgacc and aggtgacagtaaagactcgcca	IDT	N/A

(Continued on next page)

Continued

REAGENT or RESOURCE	SOURCE	IDENTIFIER
RT-PCR primer pairs for Flag-mCD45: gattacaaggatgacgacgataagccta and cgtgaactctgggttgagct	IDT	N/A
RT-PCR primer pairs for Flag-mCD148: gattacaaggatgacgacgataagccta and gatgtaaccattagtcttccaacatgct	IDT	N/A
RT-PCR primer pairs for CD1d-SCD: ggggggatcccgtactcgagggttcaataag and agtcgcggccgctcacaggacgcctgatagga	IDT	N/A
RT-PCR primer pairs for Flag-hCD45: gggattataaggacgatgatgacaaaca and tgaaccttgatttaaagctggacttg	IDT	N/A
RT-PCR primer pairs for mouse β -actin: ctgtccctgtatgcctctg and atgtcacgcacgatttcc	IDT	N/A
RT-PCR primer pairs for hamster β -actin: ctgtccctgtatgcctctg and atgtcacgcacaaatttcc	IDT	N/A
RT-PCR primer pairs for human β -actin: gagcacagagcctcgcctt and ccaggaaggaaggctggaag	IDT	N/A
Recombinant DNA		
pKG5-scT22	This paper	N/A
pKG5-scT22-CD2	This paper	N/A
pKG5-scT22-CD4	This paper	N/A
pKG5-scT22 10G/S	This paper	N/A
pKG5-scT22-CD4 10 G/S	This paper	N/A
pHR-SIN-blank (mock)	This paper	N/A
pHR-SIN-CD43-mCD45	This paper	N/A
pHR-SIN-Thy1-mCD45	This paper	N/A
pHR-SIN-Thy1-mCD45 dead	This paper	N/A
pHR-SIN-WT-mCD148	This paper	N/A
pHR-SIN-2FN3-mCD148	This paper	N/A
pHR-SIN-2FN3-mCD148 dead	This paper	N/A
pHR-SIN-schCD1d	This paper	N/A
pHR-SIN-schCD1d-CD2	This paper	N/A
pHR-SIN-schCD1d-CD4	This paper	N/A
pHR-SIN-CD43-hCD45	This paper	N/A
pHR-SIN-Thy1-hCD45	This paper	N/A
pHR-SIN-Thy1-hCD45 dead	This paper	N/A
pRSV	Dr. Ben de Wet	N/A
pGAG	Dr. Ben de Wet	N/A
pVSV-G	Dr. Ben de Wet	N/A
SMARTvector CSK shRNA 1: CAGGGTAGTTGGTGCTTTC	Dharmacon	V3SM11241-231315823
SMARTvector CSK shRNA 2: GTGCCATGGAAGTTGTACT	Dharmacon	V3SM11241-231577414
SMARTvector CSK shRNA 3: ATAAGGCTGAGTTTGGTGCT	Dharmacon	V3SM11241-231942940
SMARTvector Non-targeting Control	Dharmacon	VSC11714
pMD2.G	Dr. Didier Trono	Addgene #:12259; RRID:Addgene_12259
psPAX2	Dr. Didier Trono	Addgene #:12260; RRID:Addgene_12260

(Continued on next page)

Continued

REAGENT or RESOURCE	SOURCE	IDENTIFIER
Software and algorithms		
ImageJ V1.53	Software	https://imagej.nih.gov/ij/
Flowjo V10.6–10.9	Software	https://www.flowjo.com/
Prism GraphPad V9	Software	https://www.graphpad.com/
Rstudio 1.2	Software	https://posit.co/
DNASTAR V17	Software	https://www.dnastar.com/
Spatstat 1.64–1	Software	https://spatstat.org/

EXPERIMENTAL MODEL AND STUDY PARTICIPANT DETAILS

Mice

A breeding pair of mice that transgenically express the G8 $\gamma\delta$ TCR (bred on a Balb/c Rag^{−/−} genetic background) were a gift from YH Chien (Stanford). OT-II transgenic mouse breeding pairs (B6.Cg-Tg(TcraTcrb)425Cbn/J) were purchased from Jackson Laboratory. QM transgenic mice were a gift from Dr. Marilia Cascalho (University of Michigan Medical School).⁶⁰ Colonies were maintained under specific pathogen-free (SPF) housing conditions at the University of Michigan Medical School animal housing facility, under an Institutional Animal Care & Use Committee (IACUC) approved protocol (PRO00008433). Mice were maintained in accordance with local, state and federal regulations. 8–10-week-old male and female mice were used for experiments. Both male and female mice were used in experiments.

Cells

G8 hybridoma were a gift from Dr. YH Chien (Stanford), KN6 hybridoma were a gift from Dr. Luc Van Kaer (Vanderbilt University Medical Center), DP10.7 JKT were established as reported,⁴⁸ HEK293T cell were a gift from Dr. Akira Ono (University of Michigan). Primary cells (G8 T cells, OT-II T cells, QM-B cells) were isolated from corresponding transgenic mice (described in [method details](#)). All cells except HEK293T were cultured in complete RPMI (Gibco, 2mM Glutamax and 10% FCS.). HEK293T cells were cultured in complete DMEM (Gibco, 2mM Glutamax and 10% FCS). All cells were grown at 37°C in a humidified incubator containing 5% CO₂.

METHOD DETAILS

Recombinant expression constructs and siRNA vectors

T22 mRNA was isolated from LPS-stimulate C57BL/6 splenocytes. After RNA extraction, T22 cDNA was obtained using the Qiagen one-step RT-PCR kit according to the manufacturer's instructions. T22, and β 2-microglobulin (β 2M) were amplified by PCR, using primers listed in [key resources table](#)., such that β 2M contained a 5' XhoI site, T22 a 3' HindIII site while the primers for the β 2M 3' and T22 5'-ends together encoded for a (GGGGS)₃ flexible linker with 20 base pair overlap between the two primers. Overlap extension PCR was then used to produce a single chain dimer (SCD) of T22, consisting of murine β 2m (including the leader sequence), followed by a (GGGGS)₃ linker and the complete T22 sequence. After digestion with HindIII and XhoI, this was then cloned into the pKG5 expression vector for transfection.

The elongated SCD chimeras were generated by first introducing a BamHI site into the extracellular stalk region by site-directed mutagenesis (using oligonucleotides listed in [key resources table](#)), thereby changing the amino acid sequence by 1 residue, from the native WEPAW to WEDPAW. Human cDNA templates were used to create PCR products flanked with the BamHI restriction sites and encoding either the human CD2 ectodomain (amino acids 1–180), or human CD4 ectodomain (amino acids 1–363). The elongated SCD constructs were then produced by inserting CD2 or CD4 into the BamHI site. For the T22 SCD constructs containing GGGGS or (GGGGS)₂ flexible linkers, complementary 5'-phosphorylated oligonucleotides were annealed. The sequences of these oligonucleotides were such as to produce double-stranded DNA with 5'-overhangs of identical sequence to those produced by BamHI. These were then annealed into the T22 SCD BamHI site. Alternatively, 6 amino acids of the wild type T22 stalk sequence after the BamHI site were first deleted by oligonucleotide-directed mutagenesis (using oligonucleotides listed in [key resources table](#)) and converting WEDPAWYQDPWIW to WEDPWIW followed by insertion of the annealing oligos encoding the GGGGS or (GGGGS)₂ flexible linkers. Finally, the T22-CD4 chimera was also mutated by site-directed mutagenesis (using oligonucleotides listed in [key resources table](#)) to remove the membrane proximal BamHI site, allowing insertion of the annealing oligonucleotides encoding the GGGGS or (GGGGS)₂ flexible linkers at the remaining membrane-distal BamHI site.

A single chain construct of human CD1d was generated, with a similar design to T22 SCD. The Gp64 signal peptide, full-length human β 2M and a (G₄S)₂ linker were amplified from plasmid CD1C-NO403⁶¹ by PCR. hCD1d α chain ectodomain (aa24–295) was amplified from plasmid CD1d-590⁶² by PCR, while a segment comprising the hCD1d α chain transmembrane and cytoplasmic domains (aa296–335) were synthesized as dsDNA gBlock fragments (IDT). These three segments were ligated sequentially by overlap

PCR and inserted into XhoI/NotI linearized Phr-SIN vector by In-fusion cloning (Clontech) to produce full length CD1d SCD. To produce elongated CD1d constructs, the CD1d transmembrane and cytoplasmic segment was first 5'-ligated with mouse CD2 (aa23-202) gBlock or CD4 (aa28-391) gBlock, then ligated with the other two upstream segments (GP64 signal peptide-human β 2M-(G₄S)₂ linker and hCD1d α ectodomain) by overlap PCR, and the resulting CD1d-CD2 and CD1d-CD4 SCDs were cloned into Phr-SIN expression vector (as for CD1d SCD) for lentiviral transduction of CHO cells.

Expression constructs for Thy1-CD45, Thy1-CD45* (*; inactivating mutation in the phosphatase domain), CD43-CD45, wtCD148, 2FN3-CD148 and 2FN3-CD148* are described in detail elsewhere.³⁶ The ectodomains are derived from rat Thy1, and human CD148 and CD43, and the phosphatase-containing intracellular domain of all constructs are derived from mouse CD45. Constructs were amplified from their original vectors by PCR, and cloned into Phr-SIN vector, using XhoI and NotI restriction sites, for lentiviral transduction. The C terminus GFP sequence of the original constructs resulted in unstable expression in G8 T cell hybridomas, and was therefore removed by insertion of a TAG stop codon after the 3rd amino acid residue in the 5'-end of the sequence encoding GFP (using mutagenesis oligonucleotides listed in [key resources table](#)). Phr-SIN vector cloned with GFP alone was also mutated using the same primers to produce a "blank" Phr-SIN vector for mock transduction.

Human wild-type CD45 (WT-hCD45), Thy1-hCD45 and Thy1-hCD45* were made using a similar design to mouse CD45 chimeras. A human CD45 DNA template was amplified by PCR from Jurkat T cell cDNA using the primers listed in [key resources table](#). The CD45 signal peptide (aa1-25), FLAG tag, and full-length CD45 (aa26-1306), were amplified by PCR primers containing overlapping sequences, and ligated sequentially with XhoI/NotI-linearized Phr-SIN vector by In-fusion cloning. For the Thy1-CD45 expression construct, a rat Thy1 (aa20-135) gBlock and an overlapping CD45 segment containing the stalk/transmembrane/cytoplasmic domain of human CD45 (aa571-1306) were ligated by overlap PCR to replace full length CD45 ectodomain. The Thy1-CD45* construct was generated by site-directed mutagenesis by C853S substitution, using the primers listed in [key resources table](#).

For Csk knockdown, SMARTvector lentiviral shRNA expression vectors encoding targeting and control (non-targeting) sequences listed in [key resources table](#) under the CMV promoter were purchased from Dharmacon and used according to the manufacturer's instructions.

Cell transfection and transduction

TAP2 deficient CHO cells were stably transfected with >10g plasmid DNA using poly-L-ornithine and a 30% DMSO shock, as previously described.²⁴ Stable transfectants were selected using 0.8 mg/ml geneticin (Invitrogen) and maintained as polyclonal populations. For lentiviral transduction, HEK293T cells were transfected with constructs in Phr-SIN expression vectors, or blank Phr-SIN vector as mock control, together with pRSV, pGAG, and pVSV-G using lipofectamine 3000 (ThermoFisher), to make lentiviral particles for transduction of G8_H, Jurkat and CHO cells. Transduced cells were sorted for comparable expression levels by flow cytometry using Armenian-hamster 7H9 anti-T22 (gift from YH Chien, Stanford) for T22-expressing CHO, anti-Flag-tag M2 for Flag-CD45/CD148 chimera-expressing G8_H and Jurkat T cells, and anti-CD1d antibody for CD1d-expressing CHO cells.

For Csk knockdown, HEK293T cells were transfected with shRNA lentiviral expression vectors containing CSK-targeting shRNA or a control non-targeting RNA sequence derived from firefly luciferase ([key resources table](#)), along with pMD2.G and psPAX2 vectors. Lentiviral particles were harvested and used to transduce G8_H T cells. Transduced G8_H T cells were selected using puromycin and monitored by RFP expression. Lentiviral transduction was typically performed by "spinduction" at 1000g for 1 h at 32°C in neat RPMI containing 5 μ g/ml polybrene. Following 24hrs incubation at 37°C, 5% CO₂, cells were washed and maintained in complete RPMI.

Flow cytometry and cell sorting

To label cells for flow cytometry and cell sorting, live cells (5 x 10⁵ cells/ml) were suspended in PBS/2% FBS buffer, Fc-blocked as appropriate, and stained with surface fluorescence antibodies on ice. The stained cells were washed and filtered through a 70 μ m cell strainer before analysis using an LSRFortessa (BD) flow-cytometer. Cell sorting was performed using FACSARIA-I (BD) or Sony SH800 instruments fitted with a 100 μ m nozzle (FacsARIA-I) or 100 μ m chip (SH800). Fluorescently labeled cells were gated to select for singlets using FSC-H/FSC-W and SSC-H/SSC-W channels, and a serial fluorescence gate used to sort cells with defined expression levels of labeled cell surface proteins. Cells were sorted into tubes containing cold FBS, and transferred to complete RPMI to rest and expand for 3–5 days prior to use in experiments. Sorted cells were checked for matched levels post-sort, and prior to experiments. Flow cytometry data analysis was performed using Flowjo10 software.

Cell isolation and enrichment

Primary G8 T cells, OT-II T cells and QM-B cells were isolated by negative selection, from spleens harvested from the corresponding transgenic mice, using EasySep Mouse T cell Isolation Kit (Stemcell), EasySep Mouse CD4⁺ T cell Isolation Kit (Stemcell) and EasySep Mouse B Cell Isolation Kit (Stemcell), respectively, according to the manufacturer's instructions. Briefly, splenocytes were prepared as a single-cell suspension by maceration and straining through a 45 μ m cell strainer. Rat serum and cell separation antibody cocktails and associated magnetic beads were added, and labeled cells were removed by magnetic isolation (Big Easy, Stemcell). Enriched primary G8 cells were checked for purity by flow cytometry and rested overnight in complete RPMI media before experiment. Cell purity was checked by labeling with fluorescently labeled anti-mouse CD3 ϵ antibody and T22 tetramer (NIH Tetramer Core Facility). Alternatively, primary G8 cells were cryopreserved in 10% DMSO/FCS in liquid nitrogen. After gently thawing at 37°C water bath, frozen G8 cells were washed and rested overnight in complete RPMI media prior to use in experiments.

DP10.7 tetramer production

DP10.7 TCR was expressed in insect cells, biotinylated and tetramerized as reported previously.⁴⁸ Both chains were co-expressed in Hi5 cells by baculovirus transduction. The heterodimeric TCR was purified from cell culture supernatant with Ni-NTA Agarose (Qia-gen) and treated with 3C protease to remove tags. TCR was biotinylated with BirA biotin protein ligase in the presence of biotin, and purified over an S200 size exclusion column. TCR was tetramerized with streptavidin-allophycocyanin (Agilent).

T cell activation assay

For murine T cells and hybridomas, activation assays were performed as previously described.²⁴ Briefly, for G8 T cell hybridomas, cells (10^4 /well) were incubated with varying numbers of T22-expressing CHO cells (shown as APC/G8 ratio) at 37°C in 5% CO₂ for 24 h. In experiments using G8 T cell hybridoma transductants expressing CD45 and CD148 chimeras, 10^4 cells/well were co-cultured with equal numbers of CHO cells. Culture supernatants were assayed for IL-2 by sandwich ELISA using 1 µg/ml capture antibody (JES6-1A12), and 1 µg/ml biotinylated detecting antibody (JES6-5H4) followed by labeling with 1:2000 diluted ExtrAvidin–Peroxidase (Sigma E2886) and developed with 1-Step Ultra TMB-ELISA Substrate Solution (Thermo Scientific). For primary G8 T cells, experiments were performed as for T cell hybridomas, but mouse IFN-γ was assayed in culture supernatants using 4 µg/ml capture antibody (R4-6A2), and 1 µg/ml biotinylated detecting antibody (XMG1.2). For DP10.7 Jurkat T cells, CHO cells expressing CD1d constructs (10^5 /mL) were incubated with 30 µg/ml sulfatide (Matreya LLC) in complete RPMI for 1 h at 37°C 5% CO₂, before washing and co-culture with equal numbers of DP10. JKT cells. CD1d loading was measured using a CD1d-APC tetramer and flow cytometry. Activation of DP10.7 Jurkat T cells and CD45 transductants was assayed by measuring surface upregulation of CD69 (expressed as percentage of CD69 positive cells, or, if resting levels were variable, as change in percentage of CD69 positive cells (ΔCD69%)), relative to unstimulated cells, measured by flow cytometry.

Adhesion assay

Experiments were performed as previously described.²⁴ Briefly, to assay T22-CHO/G8_H adhesion, CHO and G8_H cells were loaded respectively with 10 µM of the red cell-labeling agent DDAO (Molecular Probes) [ex/em 635/662] and 1 µM Vybrant CFDA SE [ex/em 492/517] in serum-free RPMI-1640 for 30 min at 37°C. After 3 washes and 30 min 37°C incubation in complete media, equal numbers of CHO and G8_H (2×10^5) were mixed and centrifuged at 400rpm/4°C (brake off). Cells were incubated for 10 min at 37°C gently resuspended, and immediately analyzed using a flow-cytometer (FacScan, BD). To assay CD1d-CHO/JKT adhesion, CHO and JKT cells were loaded respectively with 2 µM CellTracker Deep Red [ex/em 630/650] and 0.5 µM CellTracker Green CMFDA [ex/em 492/517] for 30 min at 37°C, after 3 washes and 30 min 37°C incubation in complete media, CD1d-CHO were incubated with 30 µg/mL Sulfatide for 60 min at 37°C. equal numbers of CHO and JKT (2×10^5) were mixed and centrifuged at 1000rpm/4°C (brake off). Cells were incubated for 10 min at 37°C, gently resuspended, and immediately analyzed by flow cytometry (LSRFortessa, BD). Adhesion between CHO cells expressing comparable levels of CD1d constructs loaded with sulfatide, and DP10.7 Jurkat T cells were performed using a similar protocol. Comparable presentation of sulfatide-loaded CD1d constructs was checked by labeling with a fluorescently labeled DP10.7 TCR tetramer, analyzed by flow cytometry.

Biochemistry

Immunoprecipitation and immunoblotting for TCRζ was performed as previously described.²⁴ Briefly, equal numbers of G8 cells and CHO APCs expressing the indicated SCDs were rapidly brought into contact by pulse centrifugation at 500g for 1 min at 4°C. After incubation at 37°C for 0, 2, 5 or 10 min, cells were lysed with chilled lysis buffer (50 mM HEPES, pH 7.4, 150 mM NaCl, 1% NP-40, 1 mM PMSF, 10 mM pervanadate, protease inhibitor cocktail (Sigma)). For samples at the 0 time point, cells were lysed on ice immediately following centrifugation. To detect TCR conformations that bind Nck, a pull-down assay was designed based on a well-established protocol. Briefly, C-terminal mono-biotinylated Nck SH3.1 peptides were immobilized on streptavidin-conjugated magnetic beads (Pierce) and washed thoroughly. 10^7 T cells were incubated at 37°C for 10 min with anti-CD3ε mAb (2C11), T22 tetramers, CHO cells expressing T22, or sulfatide loaded CD1d. Cells were lysed using RIPA buffer (0.3% Brij O10, 140mM NaCl, 50mM HEPES, 10mM iodoacetamide, 1% protease inhibitors, 1mM sodium metavanadate), and 10^7 T cells derived lysate were incubated with 10^7 Nck peptide-immobilized beads at 4°C on a rotating mixer for 4 h. Beads were washed 5 times with RIPA buffer and eluted by boiling in loading buffer containing 20mM DTT. Samples were separated by SDS-PAGE, transferred to PVDF membranes, and immunoblotted for TCRζ using anti-CD3ζ mAb (51-6527GR), and IRDye 680LT Donkey anti-Mouse IgG (LI-COR). Blots were recorded using Odyssey Classic Infrared Imaging System.

Detection of CD3ε conformational change using APA1/1 antibody and flow cytometry

Primary G8 T and OT-II T cells were stimulated with 10 µg/ml soluble anti-CD3ε (2C11) or 15 µg/ml tetramer (T22 tetramer for G8, pOVA/I-Ab tetramer for OT-II), and medium alone was used as unstimulated control. For cell-mediated stimulation, G8_p T cells were co-cultured with CHO cells expressing T22 SCD, OT-II T cells were stimulated by co-culture with NP-specific and I-A^b-expressing QM-B cells pulsed for 16 h with 500 µg/ml NP-OVA, to present I-A^b/OVA³²³⁻³³⁹ complexes for recognition by OT-II T cells. Equal numbers of T cells and target cells were mixed and cell contacts were induced as described in [biochemistry](#). After 5 min incubation at 37°C, cells were fixed with 2% PFA for 25 min, permeabilized with 90% ice-cold methanol/PBS for 30 min, Fc-blocked and stained

with APA1/1 antibody, and secondary fluorescently conjugated anti-mouse antibody, in addition to a fluorescently labeled CD3 ϵ antibody for gating T cells from in co-cultures. Stained samples were analyzed by flow cytometry.

Flow cytometry of intracellular phosphoproteins

Primary G8 T cells were stimulated by incubation with T22-expressing CHO cells at 1:1 ratio for 2 min at 37°C. Non-transfected CHO cells were used as a negative control. Cells were then fixed, methanol-permeabilized, and Fc-blocked as in [detection of CD3 \$\epsilon\$ conformational change using APA1/1 antibody and flow cytometry](#).

TCR and LAT phosphorylation was assayed by staining fixed cells on ice for 30 min with a fluorescently labeled phospho-CD3 ζ antibody (3ZBR4S, eBioscience) and a phospho-LAT antibody (A20005D, Biolegend) respectively, and analyzed by flow cytometry.

To inhibit Lck activity in primary G8 T cells or G8 T cell hybridomas, cells were pre-incubated with 10 μ M PP2 (Sigma), 1 μ M A770041 (Sigma) or 0.1% (v/v) DMSO vehicle control for 30 min at 37°C, before incubation on plate-coated recombinant T22/ β 2M monomeric complexes (coating concentration 10 μ g/ml, 16 h at 4°C) and stimulated for the indicated times at 37°C. Inhibitor and DMSO concentrations were maintained during stimulation with plate-bound T22. Cells were then fixed, permeabilized, Fc-blocked and stained as described for [flow cytometry and cell sorting](#).

TCR downregulation assay

G8_H T cells and CHO cells expressing T22 constructs were gently centrifuged at 4°C and incubated in complete RPMI for 0–60 min at 37°C in 5% CO₂. As a control, G8_H T cells were co-cultured with untransfected CHO cells. At indicated time points, cells are resuspended and fixed with PFA at a final concentration of 2% for 15 min. Cells were then washed, quenched, labeled with Alexa 488-anti-CD3 ϵ mAb (17A2), and analyzed by flow cytometry.

Supported lipid bilayers

Supported lipid bilayers were formed by liposome deposition on piranha-cleaned glass coverslips in Biopetechs flow chambers as previously described.⁶³ The resulting planar bilayers contained DOPC as the base lipid, and contained 12.5 mol% NTA-DGS (charged with Ni³⁺), and 0.1 mol% biotinyl Cap-PE. Recombinantly produced monobiotinylated T22 or CD1d alpha-chains complexed with β 2M (obtained from the NIH Tetramer Core Facility) were attached to bilayers via a streptavidin bridge: SLBs formed in flow chambers were blocked with 4% casein containing 10mM NiSO₄, and incubated with 5 mg/mL streptavidin (Thermo Scientific) for 15 min, followed by 15 min incubation with monobiotinylated T22 or CD1d. Recombinantly produced ICAM-1-His10 (Sinobiologicals) was then attached to bilayers by coupling to Ni³⁺-charged NTA-DGS. Bilayers contained 100 molecules/ μ m² of T22 or CD1d, and 350 molecules/ μ m² of ICAM-1-10His. To load CD1d monomers with sulfatide, bilayers formed in flow chambers were incubated with 30 μ g/ml sulfatide in HBS for 1 h at 37°C, and sulfatide concentrations were maintained following introduction of T cells into flow chambers. Densities of T22, ICAM-1 and CD1d on SLBs were determined by interpolation from reference fluorophore beads as previously described.⁶³ The mobility bilayers was checked prior to imaging, by fluorescence recovery after photo bleaching of fluorophore-conjugated ICAM-1 in a randomly selected region of the bilayer. The diffusion rate, and mobile fraction was calculated from recovery curves. Typically, mobile fraction was >90% and diffusion coefficient was \sim 1 μ m²/s.

Intracellular Ca²⁺ imaging and analysis

Live G8 T cell hybridomas, mock transduced or stably transduced with CD45/CD148 chimeras or shRNA expression vectors, were washed and resuspended in neat RPMI containing 2 μ M Fluo-4 (ex/em 494/506, Ca²⁺-bound) and incubated for 25 min at 37°C. Cells were then pelleted and resuspended in complete RPMI and rested for a further 30 min at 37°C. Equilibrated cells were resuspended at 3×10^6 /mL in HBS/HSA imaging buffer (20 mM HEPES, 137 mM NaCl, 5 mM KCL, 0.7 mM Na₂HPO₄, 6mM D-Glucose, 1mM CaCl₂, 2mM MgCl₂ and 1% HSA, PH 7.2), and injected into heated Biopetechs flow chambers containing SLBs containing T22 and ICAM-1-AF647. Fluo-4 fluorescence was imaged by wide-field microscopy (20 \times objective, 488nm laser excitation, and FITC emission filters) from the point cells settled on bilayers (T = 0), and subsequently every 3 s for 2 min. 4 preselected imaging fields on each SLB were sampled sequentially at each timepoint using an encoded motorized stage with IR-based focus stabilization. The objective was pre-focused on lipid bilayers using ICAM-AF647 fluorescence. Fluo-4 fluorescence was measured using 488nm laser excitation, 500-550nm emission filter (Nikon), and an EMCCD camera (Andor).

Quantitation of Fluo-4 fluorescence intensity was performed using Fiji/ImageJ by defining ROIs of cells contacting SLBs using a threshold above the image background. Mean fluorescence intensity of ROIs was plotted for all cells in an imaging field, starting with the image corresponding to T = 0s (F₀), the first frame in cell contact with bilayers was detectable, and in subsequent images of the same cell acquired every 3 s. As a measure of intracellular Ca²⁺ influx, the ratio of the difference in Fluo-4 fluorescence intensity from the initial F₀ value (ΔF) over F₀ ($\Delta F/F_0$) was calculated for each cell over time, and mean values from all cells at each timepoint plotted as a time series.

Confocal fluorescence microscopy

Conjugates of G8 primary T cells with CHO cells expressing T22 or T22-CD4 or non-transduced CHO cells (ntCHO) were made by mixing cells at 1:1 ratio in complete RPMI, and intercellular contact established by brief centrifugation at 4°C. Pelleted cells were then incubated at 37°C to initiate signaling. Following 2 min incubation, cells were fixed by replacing culture media with 3% PFA/PBS,

gently resuspended, and left to settle on ice-cooled acid-washed coverslips coated with and poly-L-lysine for 20 min. Cells were permeabilized in 0.1% saponin/PBS for 5 min, quenched with 100 mM glycine/PBS, and blocked with 5% BSA/PBS. For labeling TCR and CD45 in G8 T Cells, samples were serially stained with 10 μ g/ml of anti-mCD3 ϵ mAb 17A2 (1hr), followed by 10 μ g/ml of Atto-488 anti-rat F(ab')₂ fragments (45 min), 10 μ g/ml anti-mCD45.2 104 (1hr), and 10 μ g/ml AF647 anti-mouse F(ab')₂ fragments (45 min). Cells were washed thoroughly with 2% BSA/PBS after each labeling step. Labeled samples were mounted in ProLong Glass Antifade mountant (Invitrogen), and imaged using a NIKON A1+ inverted microscope fitted with a 60 \times oil objective (NA 1.4, Plan Apo λ , 60 \times). The pinhole was set to obtain \sim 300 nm optical sections for each channel. AF647 was excited using a 640nm laser, and emission detected using 700/40nm emission filter, and Atto488 was excited with a 488nm laser and fluorescence images acquired using 525/50nm emission filter. DIC images were acquired using slider-mounted optics in the objective adapter. Images were recorded using and GaAsP PMT detector (Nikon). To acquire 3D image stacks, samples were imaged 200nm z-steps from the plane of the coverslip progressively into the sample. Synapse planes were isolated using the Reslice ImageJ plugin.

dSTORM sample preparation & imaging

For imaging primary G8 T cells and G8 hybridomas, 10⁶ T cells suspended in HBS/HSA were introduced into heated FCS2 flow chambers (Bioptechs) and allowed to interact with T22-containing SLBs as for *intracellular Ca²⁺-imaging*. In the experiments to inhibit LCK activity, primary G8 T cells were pretreated with 10 μ M PP2 or DMSO for 30min, PP2 and DMSO were maintained during the interaction of primary G8 T cells and SLB. After 2 min incubation, settled cells on SLBs were fixed with 3% PFA/HBS for 15 min. Flow-chambers were maintained at 37°C throughout using a filament heater attachment. Following fixation, cells were processed at room temperature as for *confocal fluorescence microscopy*. For both primary G8 T cells and G8 hybridomas, endogenous murine TCR and CD45 were labeled with antibodies and secondary reagents as for confocal microscopy. For G8 hybridomas transduced with Flag-tagged CD45 constructs, exogenous CD45 were labeled by incubation with 10 μ g/ml anti-Flag-tag mAb M2 (1hr) followed by AF647-conjugated anti-mouse F(ab')₂ fragments. DP10.7 Jurkat T cell samples were prepared using a similar process. Cells were incubated in flow chambers with SLBs containing sulfatide-loaded CD1d and ICAM-1, then fixed and processed as for G8_H T cells. Endogenous TCR and CD45 in DP10.7 Jurkat T cells were labeled by serial staining with AF647-conjugated anti-hCD45 antibody H130 (1hr) and Atto-488-conjugated anti-hCD3 ϵ antibody UCHT1 (1hr). Flag-tagged CD45 constructs in DP10.7 Jurkat T cell transductants were stained with 10 μ g/ml anti-Flag-tag polyclonal antibody (Sigma) for 1hr.

For dSTORM imaging of T cell synapses on SLBs, HBS/HAS in flow chambers containing labeled samples was exchanged with STORM buffer (10 μ M MEA, 0.56 mg/mL glucose oxidase, 40 μ g/mL catalase, 10 mM NaCl, 10% D-glucose and 200 mM Tris-HCl (pH 8)) and cells imaged on a Nikon TIRF-STORM inverted microscope fitted with a NIKON 100 \times TIRF objective (NA 1.49), using TIRF mode laser illumination. Laser outputs were 100% of a 70 mW 488 nm diode laser and 30% of a 125 mW 633nm diode laser with 0–5% of a 20 mW 405 mW diode laser, in line with a 4 \times beam magnification lens. Images were acquired with a Quad band N-STORM filter set (Nikon) fitted with excitation and emission filters for Atto-488 (ex/em: 488/505–545nm) and AF647 (ex/em: 647/664–787nm) and fluorescence detected using a sCMOS digital camera (Hamamatsu). Approximately 1,000 images were acquired alternately from each channel (total of \sim 5000 images/channel), and assembled into two-channel image stacks for analysis.

dSTORM image processing

STORM image stacks were initially analyzed using the ThunderSTORM⁶⁴ localization plugin in Fiji/ImageJ.⁶⁵ Stacks were drift-corrected using the cross-correlation method, and background noise reduced by applying a B-spline wavelet image filter. Approximate positions of fluorophore emitters were localized by identifying local maxima of emitter spots, followed by Gaussian-fitting of spot PSFs for subpixel localization of the spot center using the maximum likelihood method and multi-emitter fitting. The resulting 2D localization dataset was filtered to include fitted PSFs with a standard deviation of 50–250 nm, and a precision σ ($\sqrt{SD^2/\text{photon count}}$) cut-off of \leq 16 nm. This cut-off was empirically determined to be the minimum value that did not change the overall distribution of localization standard deviations relative to the unfiltered data. The effective overall resolution was calculated to be \sim 55nm by Fourier ring correlation using NanoJ-SQUIRREL. Localized spot coordinates were reformatted and exported as.csv files for statistical analysis in the R software package SPATSTAT.⁶⁶ Post-filtered images typically contained 10⁴ – 10⁵ localizations/channel, and 5 μ m \times 5 μ m ROIs (in SLB-formed synaptic contacts) contained \sim 5 \times 10³–10⁴ localizations/channel. The *Lest* SPATSTAT core function was used to calculate autocorrelation of spots in an individual channel using Ripley's L-function plotted as the normalized H function L(r)-r, as a function of r, where L is the L-function (variance-stabilized Ripley's K-function derived by Besag's transformation) and r is the correlation radius. This yields a value of 0 for a random Poisson distribution. Similarly, the *Lcross* core function was used to analyze cross-correlation of spots between two imaging channels, and plotted as the normalized H function. Negative values indicate dispersion (segregation) and positive values indicate co-clustering. Images were rendered as Gaussian filtered images (using the Gaussian blur function in ImageJ – in which “intensity” approximates point density) or as 2D point coordinates at higher digital magnification.

Transmission electron microscopy

Sample processing of T cell/CHO cell conjugates for electron microscopy has been described in detail elsewhere. Briefly, conjugates of G8 T cell hybridomas and CHO cells expressing either T22 or T22-CD45 were prepared as for fluorescence microscopy. Culture medium was replaced with a mixture of 2.5% glutaraldehyde and 2% formaldehyde in 100mM cacodylate buffer (pH 7.4) with 2 mM

Ca^{2+} , post-fixed in buffered 1% osmium tetroxide and *en bloc* stained with 0.5% aqueous uranyl acetate. Ultrathin sections (~60 nm thick) were cut and double-stained with uranyl acetate and lead citrate. Subsequent sample processing and image acquisition was performed as previously described. Intermembrane distance was measured in regions of the interface (at 200% digital magnification) where apposed membranes were aligned (parallel), and at which both membranes exhibited a trilaminar “tramline” appearance, indicating that they were orthogonal to the imaging plane.

QUANTIFICATION AND STATISTICAL ANALYSIS

Unpaired t test and one-way ANOVA (with correction for multiple comparisons) were performed to compare multiple sample means using GraphPad PRISM9 software. Pearson’s cross-correlation coefficient (PCC) is used to analyze co-localization in confocal *en face* synapse reconstructions, in which higher values indicate greater intensity co-localization between corresponding pixels from two images. For dSTORM auto- and cross-correlation analysis averaged Ripley’s H function is plotted \pm SEM (see [dSTORM image processing](#)). To quantify immunoblot blots, TIF image scans of blots were analyzed using the Gel Analyzer tool in ImageJ. The intensity of TCR ζ bands in Nck-PD or phosphorylated TCR ζ (pTCR ζ), were measured and normalized against control samples (either untreated or stimulated with ntCHO, as applicable). Normalized values were plotted as a ratio over normalized intensity of TCR ζ bands in the input cell lysates of corresponding samples. In the case of TCR ζ pull-down, the intensity of pY bands was normalized against of the intensity pY in control lanes, and plotted as a ratio of TCR ζ normalized to TCR ζ intensity in control lanes. Normalized ratios were pooled from multiple independent experiments, and expressed in relative units (R.U.). The R.U. data were then graphed and statistically analyzed using GraphPad Prism software.

Cell Reports, Volume 43

Supplemental information

**Ligand-induced segregation from large
cell-surface phosphatases is a critical
step in $\gamma\delta$ TCR triggering**

Fenglei Li, Sobhan Roy, Jacob Niculcea, Keith Gould, Erin J. Adams, P. Anton van der Merwe, and Kaushik Choudhuri

Figure S1.

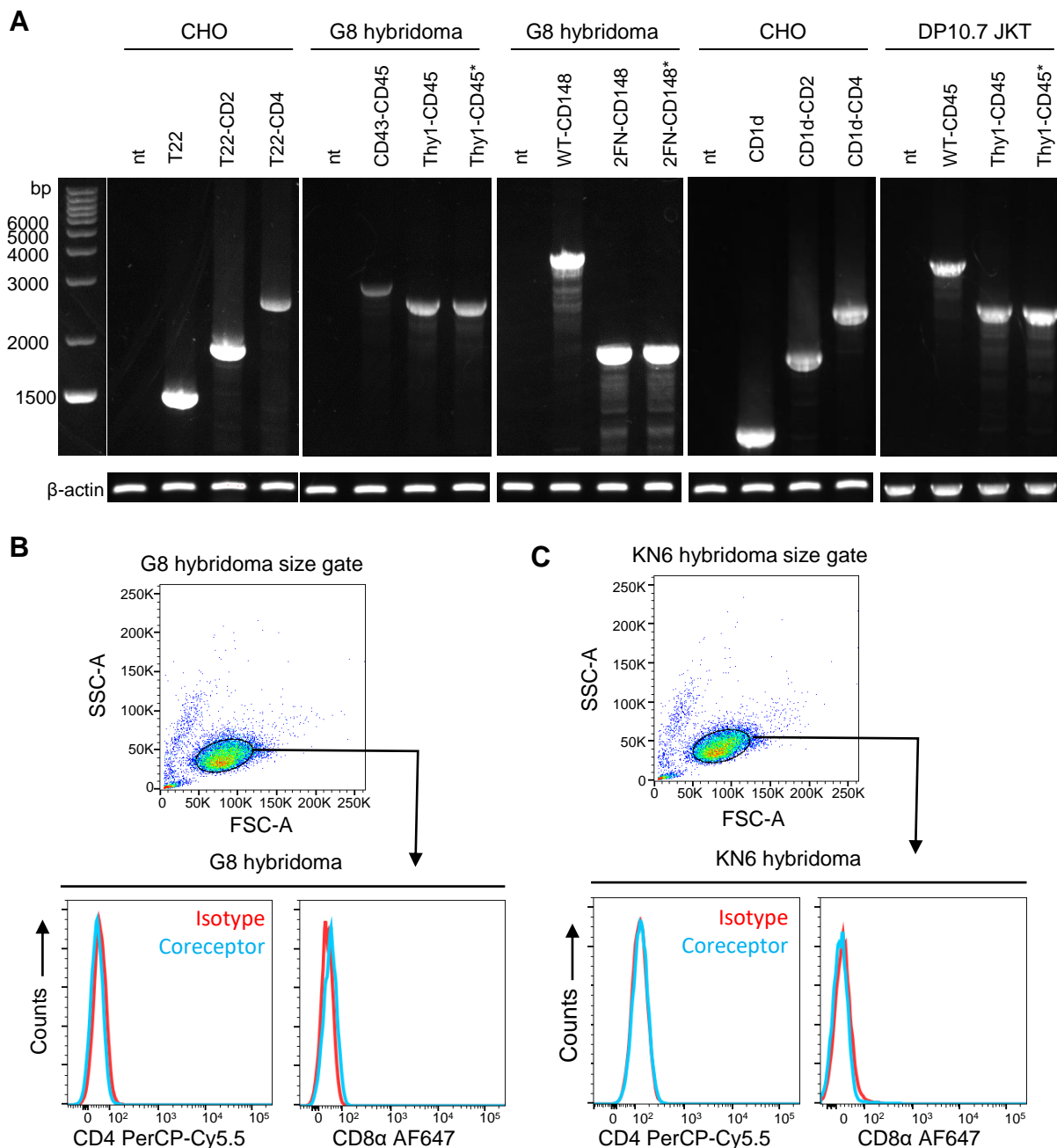


Figure S1. Characterization of CHO cell transductants and T cell hybridomas (related to expression constructs and cell lines in Figures 1, 5 and 7).

(A) RT-PCR of total RNA extracted from the indicated cell lines stably transduced with the indicated constructs. RT-PCR reactions were performed using the primers listed in Supplementary Table 2.

(B), (C) Gating strategy and histogram overlays of surface expression of co-receptors CD4 and CD8 (cyan lines) in (B) G8, and (C) KN6, T cell hybridomas as measured by flow-cytometry.

Figure S2.

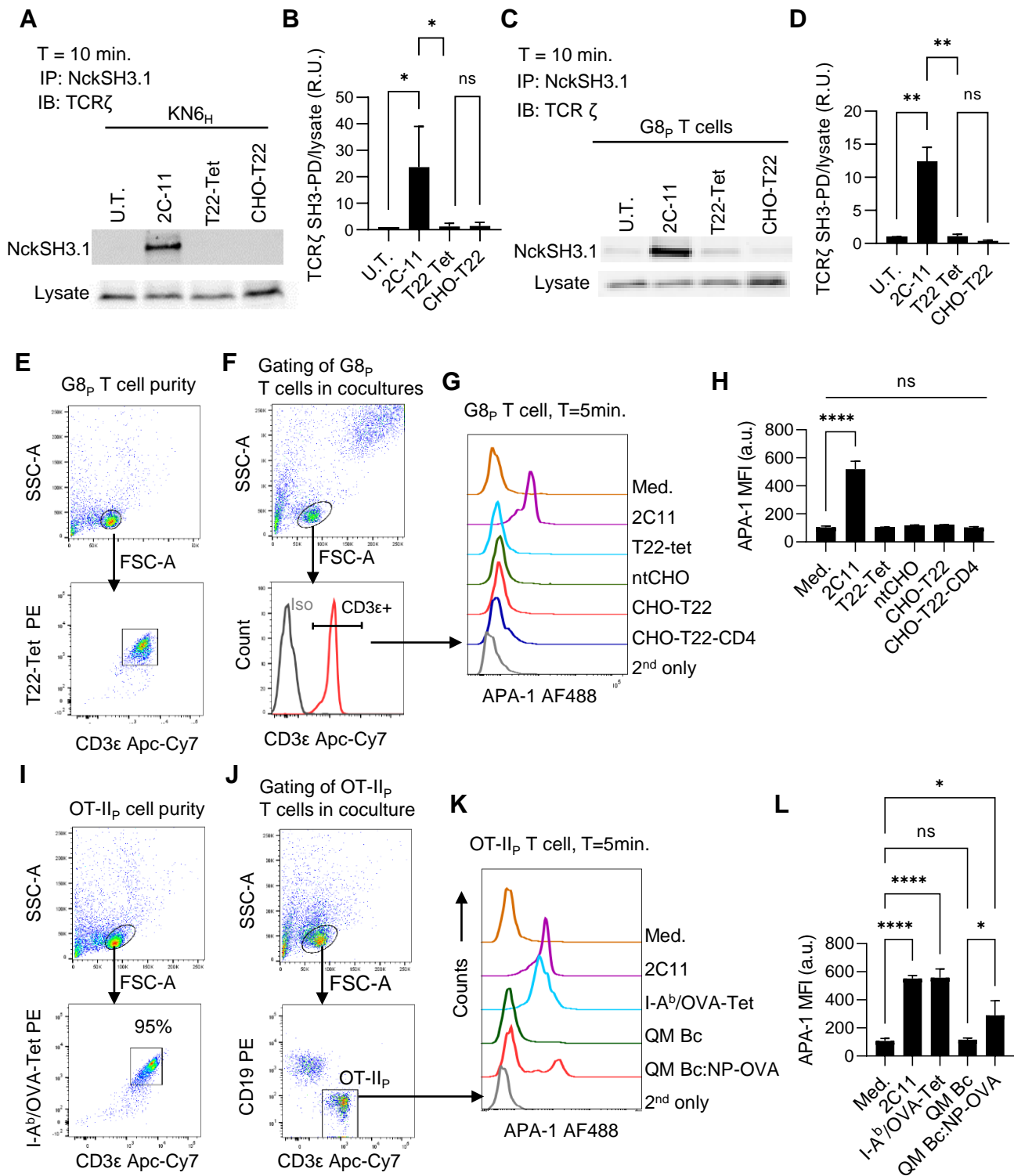


Figure S2. $\gamma\delta$ TCR triggering does not require conformational changes typical of $\alpha\beta$ TCRs (related to Figures 1 and 2, figure legend on following page).

Figure S2. KN6 and G8 $\gamma\delta$ TCR triggering does not require conformational changes typical of $\alpha\beta$ TCRs (related to Figures 1 and 2).

(A) Representative immunoblot of TCR ζ in Nck SH3.1 pulldowns from KN6 T cell hybridomas (KN6_H) following 10 min incubation with anti-CD3 ϵ antibody 2C11, T22 tetramer (T22 Tet), or CHO cells expressing T22 SCD. TCR ζ blots of input lysates is shown as a loading control.

(B) Quantitation of blots as in (A). Data are presented as normalized ratios of TCR ζ density in Nck SH3.1 pulldowns (TCR ζ SH3-PD) over TCR ζ density in corresponding input lysates. $n = 3$, data are mean \pm SD.

(C) Representative immunoblot of TCR ζ in Nck SH3.1 pulldowns from primary G8 T cell hybridomas (G8_p) following 10 min incubation with anti-CD3 ϵ antibody 2C11, T22 tetramer, or CHO cells expressing T22 SCD. TCR ζ blots of input lysates is shown as a loading control.

(D) Quantitation of blots as in (C). Data are presented as normalized ratios of TCR ζ in Nck SH3.1 pulldown (TCR ζ SH3-PD) over TCR ζ in corresponding input lysates. $n = 2$, data are mean \pm SD.

(E) Flow cytometry dot plots showing size gate and purity of primary G8 T cells (G8_p) stained with fluorescently labelled cognate T22 tetramer (T22-Tet) and anti-CD3 ϵ antibody.

(F) Gating of G8_p T cells in cocultures with CHO cell transductants.

(G) Histogram cascade plots of G8_p T cells gated as in (F) stained with fluorescently labelled conformation-sensitive CD3 ϵ antibody APA1/1, after incubation for 5min at 37°C in medium alone (Med.), or with 2C11 antibody, T22-Tet, non-transduced CHO cells (ntCHO), or with the indicated CHO cell transductants.

(H) Quantitation of APA1/1 staining intensity (MFI) of G8_p T cells as in (G). $n = 3$, data are mean \pm SD. a.u, arbitrary units.

(I) Flow cytometry dot plots showing size gate and purity of primary OTII $\alpha\beta$ T cells (OT-II_p) stained with fluorescently labelled cognate I-A^b/OVA³²³⁻³³⁹ tetramer (I-A^b/OVA-Tet) and anti-CD3 ϵ antibody.

(J) Gating of OT-II_p T cells in cocultures with QM B cells (CD19⁺).

(K) Histogram cascade plots of OT-II_p T cells gated as in (J) stained with with fluorescently labelled conformation-sensitive CD3 ϵ antibody APA1/1, after incubation for 5min at 37°C in medium alone (Med.), or with 2C11 antibody, I-A^b/OVA-Tet, unloaded QM B cells (QM Bc), or with ovalbumin-loaded QM B cells (QM Bc:NP-OVA).

(L) Quantitation of APA1/1 staining intensity (MFI) of OT-II_p T cells as in (K). $n = 3$, data are mean \pm SD. a.u, arbitrary units.

Means were compared by 1-way ANOVA corrected for all pairwise comparisons. *, $P < 0.05$; **, $P < 0.001$; ***, $P < 0.0001$; ns, not significant ($P > 0.05$).

Figure S3.

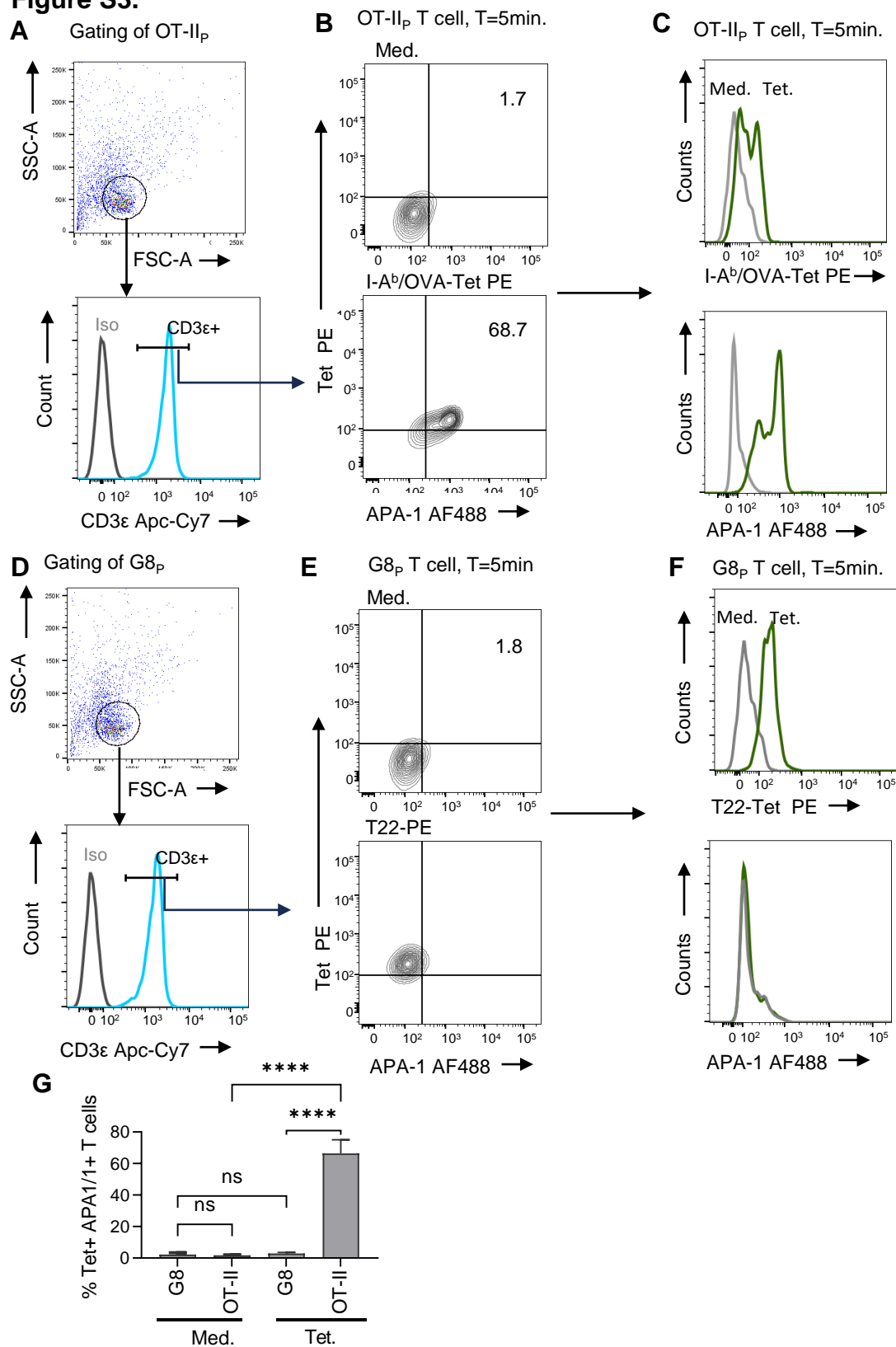


Figure S3. Absence of T22 tetramer-induced conformational change in G8 TCRs is not due to tetramer unbinding. (related to Figures 1 and 2, figure legend on following page).

Figure S3. Absence of T22 tetramer-induced conformational change in G8 TCRs is not due to tetramer unbinding.

(A) OT-II_p and (D) G8_p T cells were incubated with the indicated fluorescently labeled tetramers (Tet) or medium (Med) alone for 5 min, following washing, were fixed, permeabilized and stained with fluorescently-labeled conformation sensitive antibody specific for the cytoplasmic portion of CD3 ϵ (APA1/1) and CD3 ϵ ectodomain-specific antibody for gating. Shown are scatter plots indicating the live cell size gate and TCR+ serial gates.

(B,E) Contour plots of TCR-gated OT-II_p (B) and G8_p (E) T cells showing APA1/1 staining and levels of cell-bound cognate tetramers.

(C,F) Histogram overlays of TCR-gated OT-II_p (C) and G8_p (F) T cells showing APA1/1 staining and levels of cognate tetramer binding.

(G) Quantitation of Tetramer+ APA1/1+ cells. Means were compared by 1-way ANOVA corrected for all pairwise comparisons. ****, $P < 0.0001$; ns, not significant ($P > 0.05$).

Figure S4.

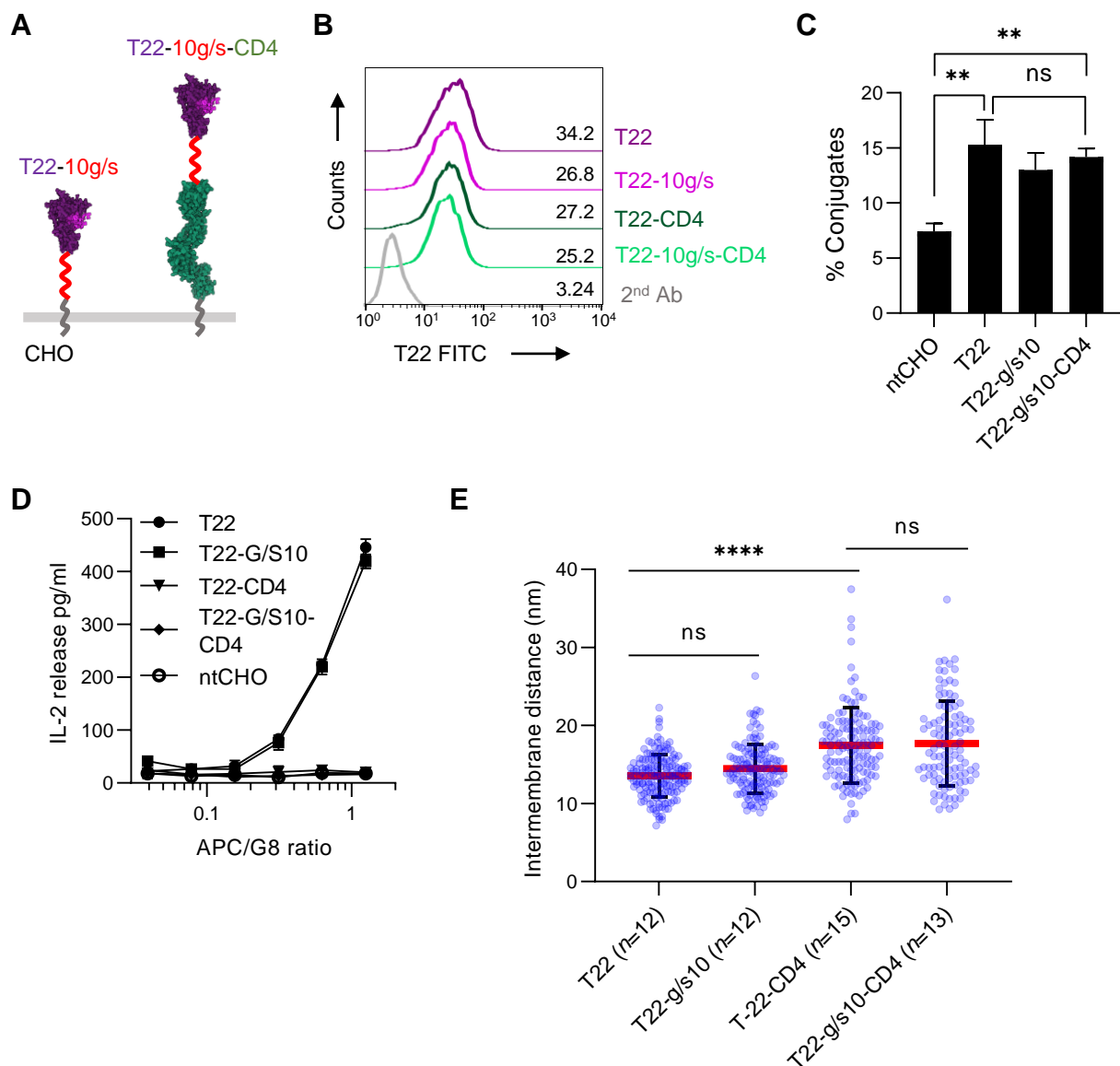


Figure S4. G8_H T cell activation and intermembrane distance at synapses is unaffected by increased T22 flexibility (related to Figures 1 and 3, figure legend on following page)

Figure S4. G8_H T cell activation and intermembrane distance at G8 synapses is unaffected by increased T22 flexibility (related to Figures 1 and 3).

(A) Cartoon schematic of T22 and CD4-elongated T22 in which the 5 residue glycine/serine (g/s) linkers (grey) at the T22 C-terminus were replaced with 10 residue glycine/serine linkers (red) to increase flexibility of chimeric constructs.

(B) Histogram cascade plots of CHO cell surface expression of the indicated T22 constructs as measured by flow-cytometry. Constructs were stably expressed in CHO cells and sorted for comparable expression.

(C) Cell-cell adhesion as measured by conjugate formation between G8 T cell hybridomas and CHO cells expressing indicated T22 constructs. Results are representative of 3 independent experiments. Data are mean \pm SD.

(D) Activation of G8 $\gamma\delta$ T cell hybridomas in response to original and flexible forms of T22, as measured by IL-2 release. 10^4 G8 $\gamma\delta$ T cell hybridomas were cocultured with increasing numbers of T22-expressing CHO cells for 24 hrs (expressed as APC/G8 cell ratio), and IL-2 release in culture supernatants measured by ELISA. Results are representative of 3 independent experiments. Data are mean \pm SD.

(E) Intermembrane distances measured at synaptic contacts between G8 $\gamma\delta$ T cell hybridomas and CHO cells expressing original and flexible versions of T22 and CD4-elongated T22. Data points are individual intermembrane distance measurements in each group. The number of conjugates sampled (n) is indicated for each group. Red line indicate mean and error bars are \pm SD.

Means were compared by 1-way ANOVA corrected for all pairwise comparisons. **, $P < 0.001$; ***, $P < 0.0001$; ns, not significant ($P > 0.05$).

Figure S5.

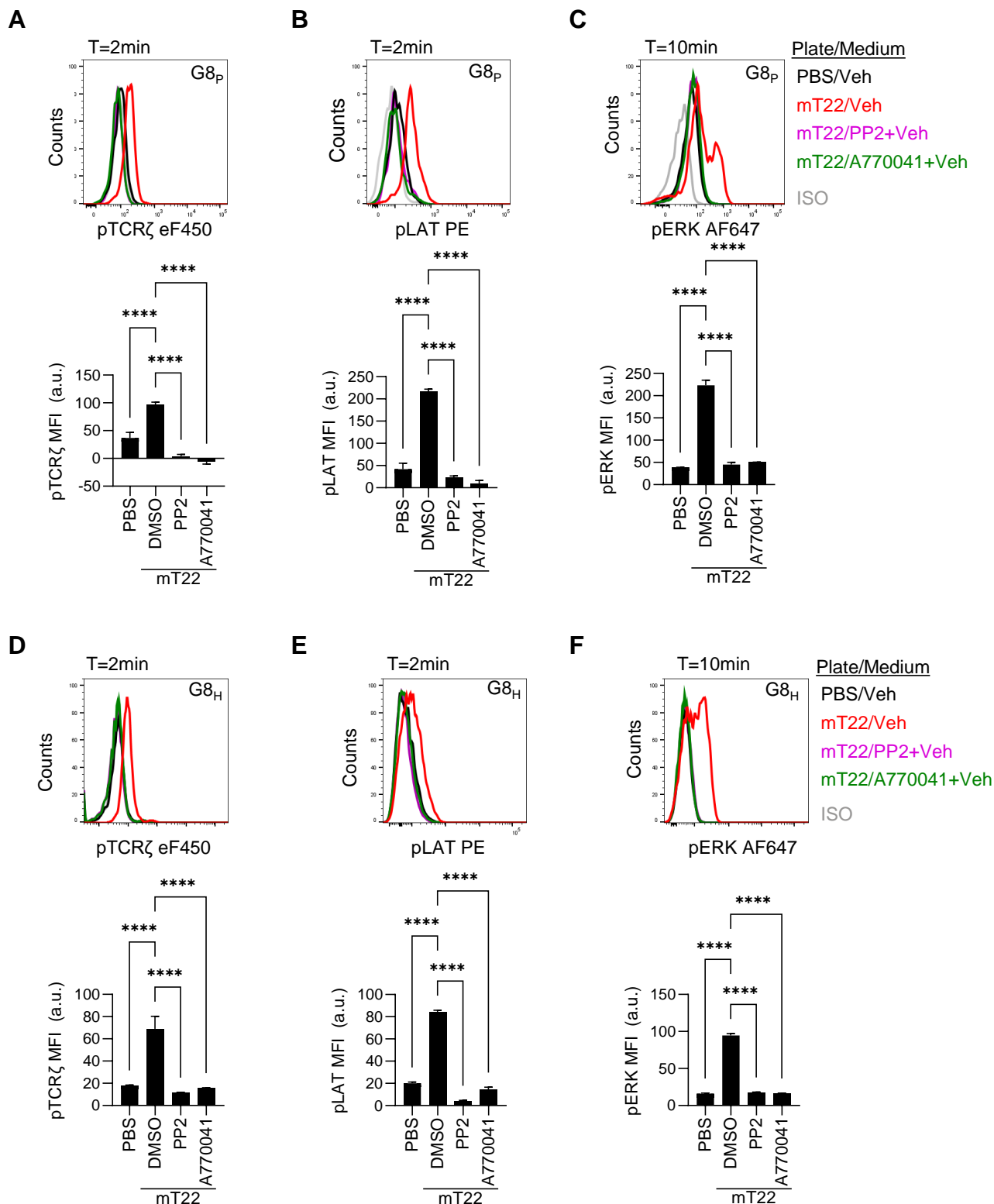


Figure S5. Lck activity is critical for T22-mediated G8 TCR phosphorylation and downstream signal transduction. (related to Figures 1 and 2, figure legend on following page).

Figure S5. Lck activity is critical for T22-mediated G8 TCR phosphorylation and downstream signal transduction. (related to Figures 1 and 2).

(A) Top panel, Flow cytometry histogram overlay of pCD3 ζ antibody staining of primary G8 T cells (G8_p), pretreated with the indicated inhibitors, or with DMSO vehicle alone (Veh), and incubated for 2 minute at 37°C on plate-adsorbed recombinant T22 monomers (mT22), or in uncoated wells (PBS). ISO, Isotype control antibody staining. **Bottom panel,** Quantitation of pCD3 ζ antibody staining as in *Top Panel*.

(B) Top panel, Histogram overlay of pLAT antibody staining in primary G8 T cells (G8_p) treated as in (A). **Bottom panel,** Quantitation of pLAT antibody staining as in (A, *Bottom Panel*).

(C) Top panel, Histogram overlay of pERK antibody staining in primary G8 T cells (G8_p) pretreated as in (A), and incubated for 10 min at 37°C on plate-adsorbed recombinant T22 monomers (mT22), or in uncoated wells (PBS). **Bottom panel,** Quantitation of pERK antibody staining as in (A).

(D) Top panel, Histogram overlay of pCD3 ζ antibody staining in G8 T cell hybridomas (G8_H), treated as in (A). **Bottom panel,** Quantitation of pCD3 ζ antibody staining as in (A).

(E) Top panel, Histogram overlay of pLAT antibody staining in G8_H T cells treated as in (A). **Bottom panel,** Quantitation of pLAT antibody staining as in (A, *Bottom Panel*).

(F) Top panel, Histogram overlay of pERK antibody staining in G8_H T cells pretreated as in (A), and incubated for 10 min at 37°C on plate-adsorbed recombinant T22 monomers (mT22), or in uncoated wells (PBS). **Bottom panel,** Quantitation of pERK antibody staining as in (A).

Data are MFI after background subtraction of mean ISO values, and results are representative of 3 independent experiments. Mean \pm SD is shown. Means were compared by 1-way ANOVA and corrected for all pairwise comparisons. *****, $P < 0.0001$.

Figure S6.

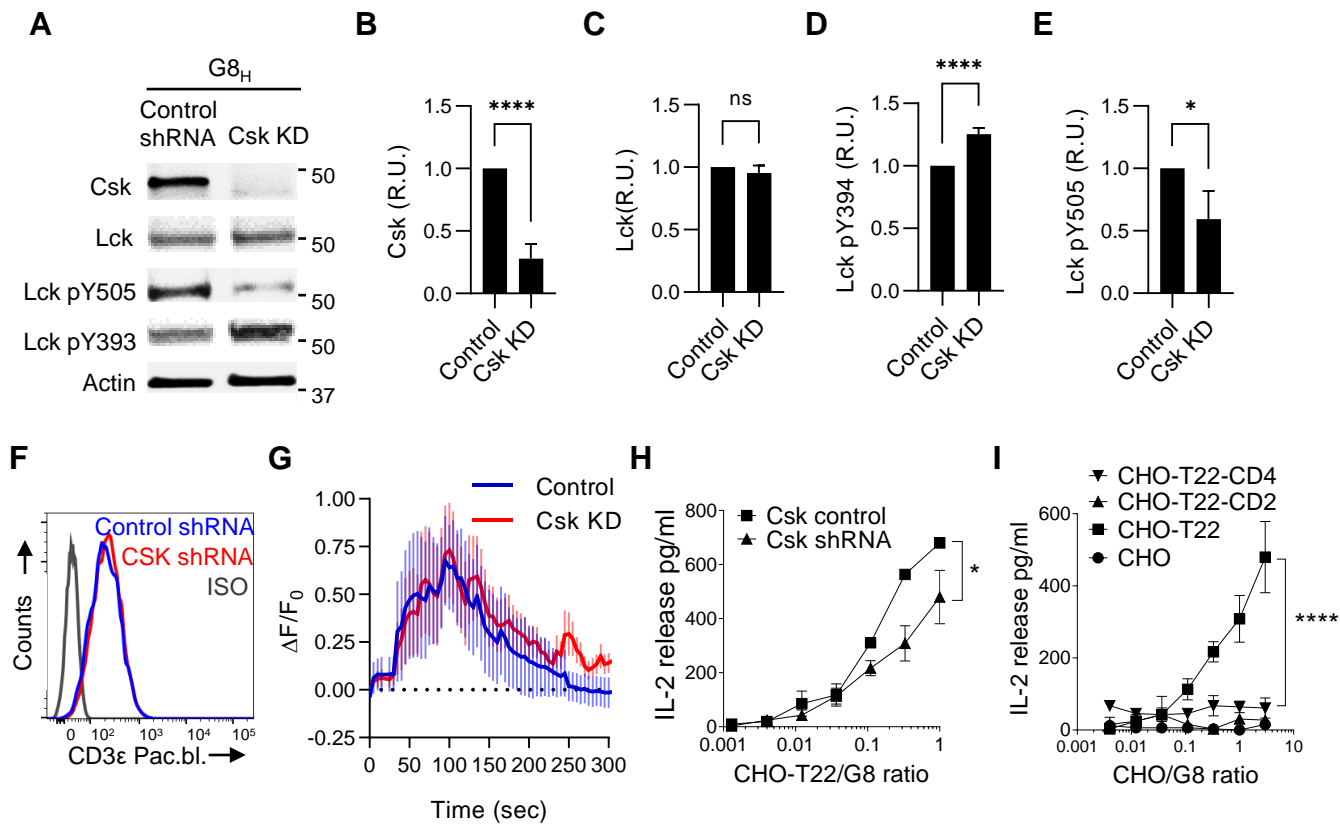


Figure S6. Suppression of Csk expression increases active Lck levels but fails to rescue TCR triggering in response to elongated T22 (related to Figure 1, figure legend on following page).

Figure S6. Suppression of Csk expression increases active Lck levels but fails to rescue TCR triggering in response to elongated T22.

(A) Immunoblots of resting G8_H T cell lysates that were stably transduced with Csk-targeting or non-targeting control shRNA. Cell lysates were analyzed using antibodies for Csk, and antibodies specific for the tyrosine phosphorylated positive (Y393) and negative (Y505) regulatory sites of Lck. A representative blot from 3-5 independent experiments is shown.

(B)-(E) Quantitation of the indicated phosphorylated proteins from immunoblots as in **(A)**. B: $n = 4$, C, E: $n = 5$, D: $n = 3$.

(F) Cell-surface TCR expression levels of G8_H T cells transduced with the indicated shRNA expression vectors shRNA. Cells were labeled with an anti-CD3 ϵ antibody and analyzed by flow-cytometry.

(G) Analysis of Ca²⁺ signaling in live G8_H T cells transduced with Csk targeting (Csk KD) or non-targeting (Control) shRNA following contact with planar lipid bilayers containing 100 molecules/ μm^2 T22 and 350 molecules/ μm^2 ICAM-1. T cells were loaded with Fluo-4 and Ca²⁺ flux imaged by epifluorescence microscopy following contact with supported lipid bilayers (T=0). Plots represent (mean fluorescence - fluorescence at T=0)/(fluorescence at T=0) \pm SEM. Results are pooled from 2 independent experiments.

(H) Activation of G8_H T cells stably transduced with Csk-targeting or control shRNA, as measured by IL-2 release after 24hrs co-culture with T22-expressing CHO cells. Results are representative of 3 independent experiments.

(I) IL-2 release in response to Increasing numbers of CHO cells expressing T22 and elongated forms of T22 (expressed as CHO/G8 ratio) by 10⁴ G8_H T cells expressing Csk-targeting shRNA. Results are representative of 3 independent experiments.

Mean \pm SD is shown. Means were compared by *t*-test. *, $P < 0.05$; ****, $P < 0.0001$. In **(H)** and **(I)** data means at G8/CHO ratio=1 are tested for the indicated comparisons.

Figure S7.

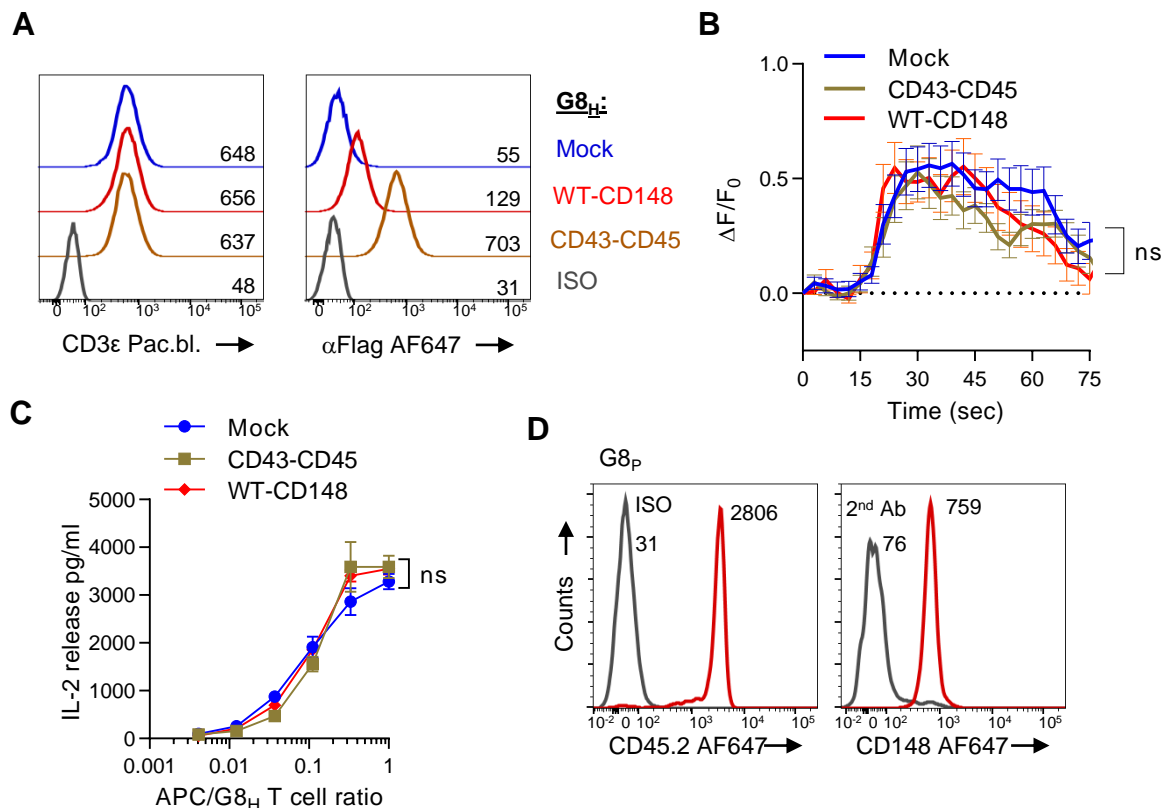


Figure S7. Phenotype and function of lentivirally transduced G8_H T cells. Related to Figure 5.

(A) Cascade plots of surface expression levels of TCR and the indicated CD45/148 constructs, including an empty expression construct for mock transduction, following lentiviral transduction of G8_H T cells. Flag-tagged constructs and surface TCR were detected by immunostaining and flow-cytometry.

(B) Analysis of Ca²⁺ signaling in live G8_H T cells, transduced with the indicated expression constructs, following contact with planar lipid bilayers containing 100 molecules/μm² T22 and 350 molecules/μm² ICAM-1. T cells were loaded with Fluo-4 and Ca²⁺ flux imaged by epifluorescence microscopy following contact with supported lipid bilayers (T=0). Plots represent (mean fluorescence - fluorescence at T=0)/(fluorescence at T=0) ± SEM. Results are pooled from 3 independent experiments.

(C) Activation of the indicated G8_H T cell transductants as measured by IL-2 release after 24hrs co-culture with T22-expressing CHO cells. Results are expressed as a ratio of increasing numbers CHO cells expressing T22 incubated with 10⁴ G8_H T cell transductants for 24hrs. Results are representative of 3 independent experiments.

(D) Flow-cytometry histograms showing surface expression levels of CD45 and CD148 on primary G8 (G8_p) T cells. ISO, isotype control antibody.

Figure S8.

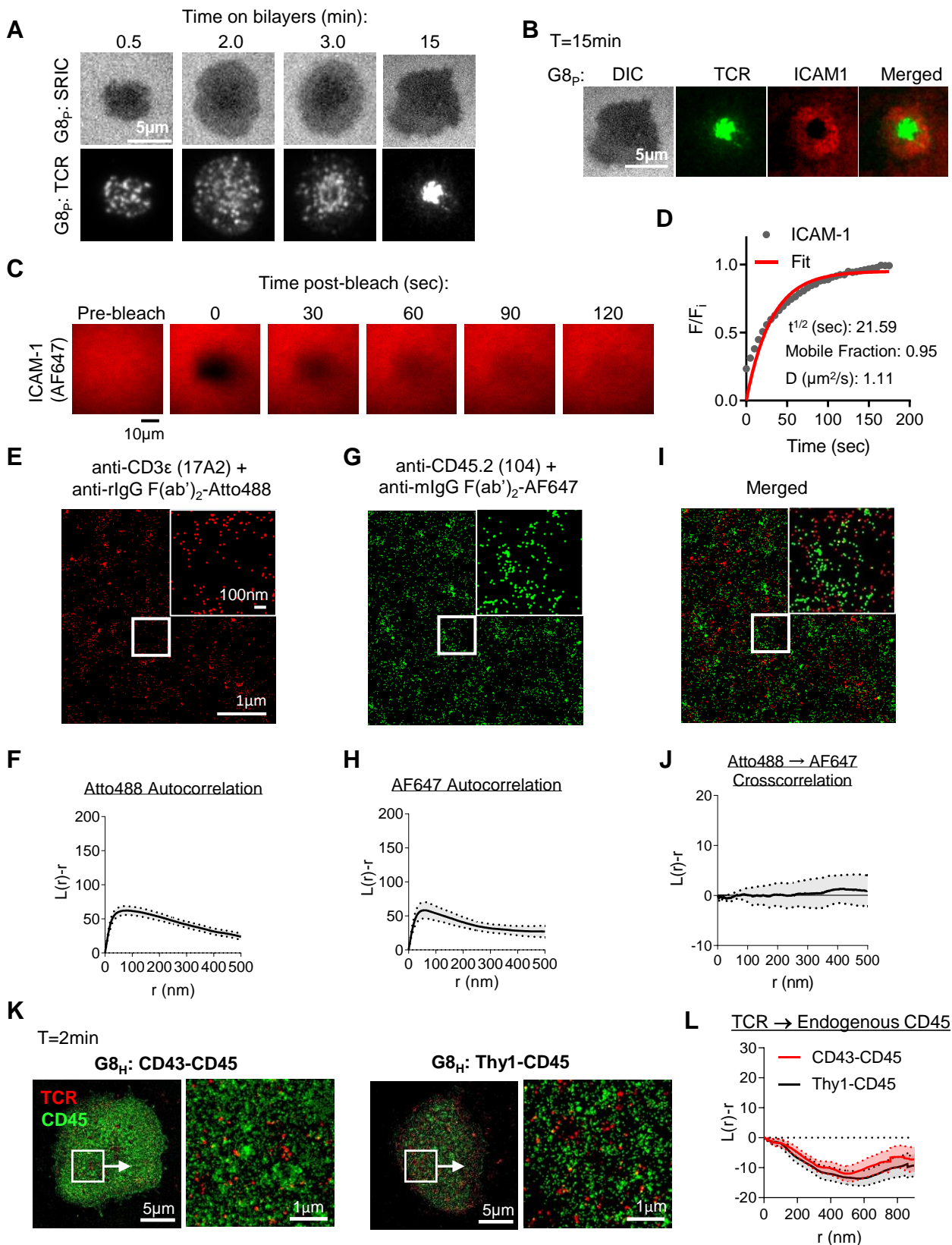


Figure S8. Validation of imaging conditions and cell sample controls for TIRFM/dSTORM imaging of $\gamma\delta$ T cell synapses on SLB (related to Figures 6 and 7, figure legend on following page).

Figure S8. Validation of imaging conditions and cell sample controls for TIRFM/dSTORM imaging of $\gamma\delta$ T cell synapses on SLB (related to Figures 6 and 7).

(A) Representative TIRFM images of G8_p T cells forming synapses on SLB containing 100 molecules/ μm^2 T22 and 350 molecules/ μm^2 ICAM-1 at the indicated timepoints. T cells were incubated on bilayers for indicated times at 37°C. cells were then fixed,, permeabilized and labelled with an anti-CD3 ϵ antibody and a fluorescently-labeled 2nd antibody.

(B) Representative image of a G8_p T cell forming a mature immunological synapse after 15 minutes interaction with SLB containing T22 and ICAM-1-AF647, and processed as in A.

(C) Time series of fluorescence recovery after photobleaching of AF647-labeled ICAM-His10 attached to SLB at 350 mol/ μm^2 . A prebleach image was taken prior to photobleaching of a 15 μm diameter ROI using 633nm laser irradiation.

(D) The ratio of post-bleach fluorescence intensity captured at 5sec intervals (F_i) over the pre-bleach fluorescence intensity (F_0) was plotted over time to fit with one phase exponential function for extraction of recovery half-time $t^{1/2}$, diffusion coefficient D , and mobile fraction parameters.

(E) dSTORM Gaussian filtered localization image of rat anti-mCD3 ϵ mAb 17A2 adsorbed onto a PLL-coated coverslip. Indicated primary antibodies were adsorbed on PLL coverslip for 1hr at RT, fixed with 3% PFA for 45mins, quenched with 100mM glycine for 1hr, blocked with 5% BSA for 1hr, and stained with indicated 2nd antibody for 1hr (f/p ~ 2). Inset shows unfiltered localizations in white boxed region.

(F) Ripley's H-function autocorrelation of the Atto488 label.

(G) dSTORM localization image of the anti-CD45.2 mAb 104 labelled with a polyclonal anti-mIgG (H+L chain) F(ab')₂-AF647 secondary antibody (f/p ~2).

(H) Autocorrelation of the AF647 label.

(I) Merged image of Atto488 and AF647 localizations.

(J) Ripley's H-function cross-correlation of Atto488 and AF647 labels. Negative values represent dispersion (segregation) and positive values represent clustering. Shaded region within dotted lines demarcate 95% confidence intervals.

(K) Left panels, Representative Gaussian-filtered images of endogenous TCR and CD45 localizations at synapses formed by G8 hybridoma (G8_H) transduced with the indicated Flag-tagged CD45 chimeras (not detected). **Right panels,** High magnification Gaussian-filtered images of white boxed region in *left panels*.

(L) Cross-correlation of endogenous TCR and CD45 localizations. Graphs represent mean \pm SEM. CD43-CD45 transduced G8 hybridomas: $n=39$ ROIs (pooled from 10 synapses); Thy1-CD45 transduced G8 hybridomas: $n= 30$ ROIs (pooled from 11 synapses). Synapses were randomly chosen from pooled images from 3 independent experiments.

Figure S9.

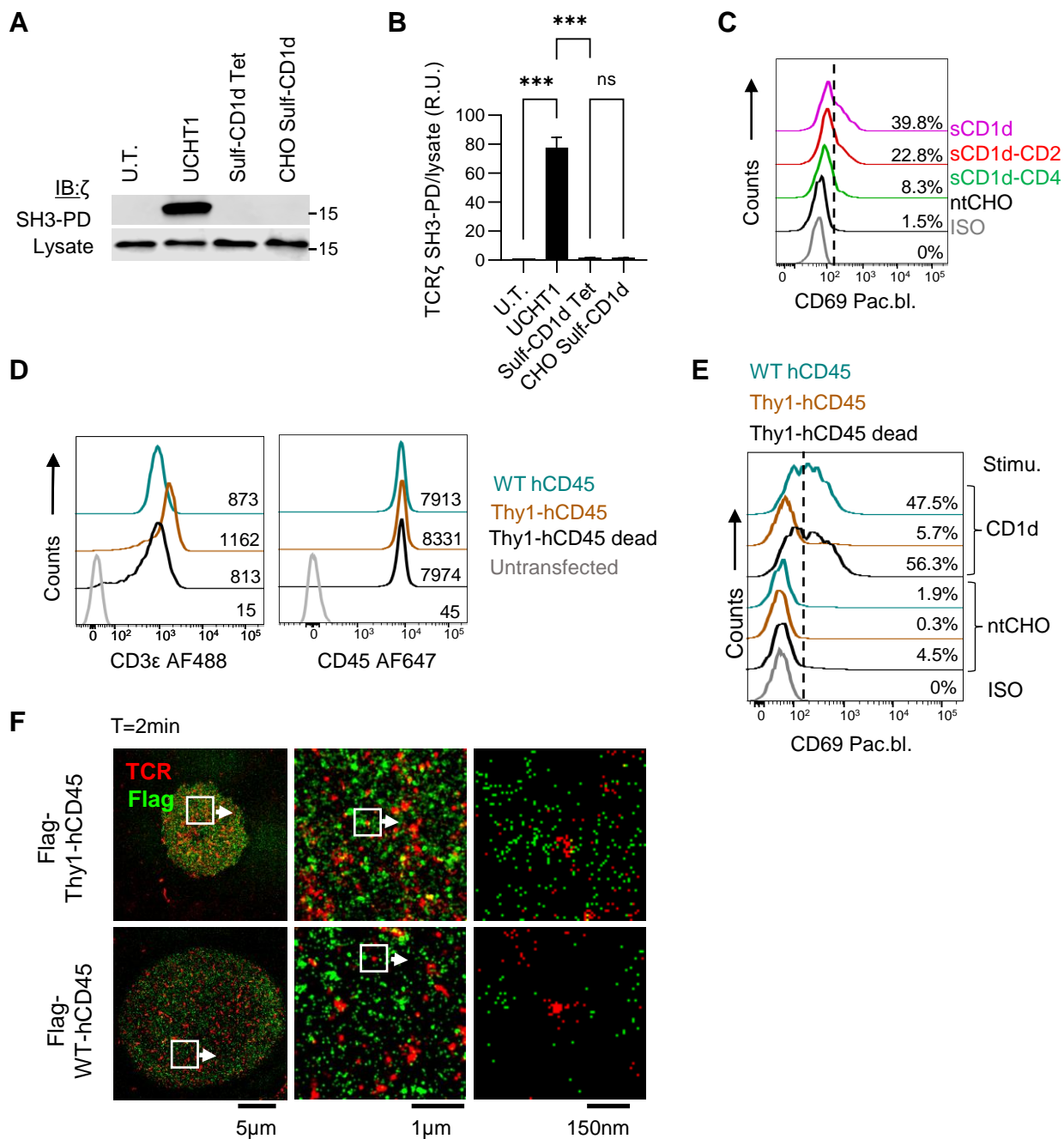


Figure S9. Size-dependent DP10.7 TCR signaling in the absence of Nck-recruiting conformational change (Related to Figure 7, figure legend on following page).

Figure S9. Size-dependent DP10.7 TCR signaling in the absence of Nck-recruiting conformational change.

(A) Detection of CD3 ϵ conformational change by Nck SH3.1 TCR pulldown in DP10.7 Jurkat T cells. Cells were incubated with anti-CD3 ϵ mAb UCHT1, sulfatide-loaded CD1d tetramer, or left untreated (U.T.), and blotted for TCR ζ in pulldowns and input lysates.

(B) Quantitation of blots as in **(A)**. Data are presented as normalized ratios of TCR ζ density in Nck SH3.1 pulldown lanes (TCR ζ SH3-PD) over TCR ζ density in corresponding input lysates. R.U., relative units. $n = 3$, data are mean \pm SD.

(C) Representative histogram cascade plot of surface CD69 expression levels of DP10.7 Jurkat T cells corresponding to **Figure 7F**. Numbers denote % CD69 $^{+}$ cells determined by isotype antibody labeling of resting DP10.7 Jurkat T cells (demarcated by dashed line).

(D) Representative histogram cascade plot of surface staining of endogenous TCR and CD45 in DP10.7 Jurkat T cell transductants expressing the indicated CD45 chimeras. Numbers represent MFI.

(E) Representative histogram cascade plot of surface CD69 expression levels of DP10.7 Jurkat T cell transductants, incubated with sulfatide-loaded CD1d-CHO cells, corresponding to Figure 7L. Due to variability in CD69 levels in resting DP10.7 Jurkat T cell transductants, change in % CD69 $^{+}$ DP10.7 cells was calculated for Figure 7L ($\Delta\%$ CD69 $^{+}$).

(F) Representative *d*STORM images of TCR and Flag-tag localizations at synapses of DP10.7 Jurkat T cells transduced with the indicated Flag-tagged CD45 chimeras.

Supplementary Table 1. Quantitation of cell surface molecules

Cell Type	Construct expressed	mol/ μm^2	% of endogenous CD45/CD148
G8 T cell hybridoma (G8 _H)	None (Endogenous CD45)	793.8	100
	Thy-CD45	3.6	0.5
	Thy1-CD45*	2.9	0.4
	CD43-CD45	16.3	2.1
	None (Endogenous CD148)	43.8	100
	2FN3-CD148	19.4	44.3
	2FN3-CD148*	18.8	42.3
	WT-CD148	3.2	7.3
Primary G8 T cells (G8 _P)	None (Endogenous)	47.3	100
DP10.7 Jurkat T cell	None (Endogenous CD45)	622	100
	Thy-CD45	34.1	5.3
	Thy1-CD45*	72.2	11.2
	WT-CD45	38.0	5.9

*Catalytically inactive mutant

Extended Data Table 2. Oligonucleotide sequences

T22 constructs	T22	Forward: tcgggtggcggcggtctgggtcacactcgcttaggtatttc
		Reverse: gaggaagcttcagtcgaagtgacagtaaagactcg
	β -2M	Forward: gatatctcgagtcgcttcagtcgtcagcatgg
		Reverse: ccagagccgccacccgagccgcctccgccgaaccgcca cctcccatgtctcgatcccagtagac
	BamHI site insertion	Forward: taatggatcctgcatggaagtgggtgc
		Reverse: taatggatcctcagtcggcagaacctg
	BamHI site removal	Single primer: gatgggaggatccgtggatttgattgtg
	CD45 STOP insertion	Forward: gagcaagggcgagtagctgttcaccgg
		Reverse: ccggtgaacagctactcgcccttgctc
RT-PCR	T22-SCD	Forward: atggctcgtcggtgacc
		Reverse: aggtgacagtaaagactcgcca
	Flag-mouseCD45	Forward: gattacaaggatgacgacgataagccta
		Reverse: cgtgaactctgggttgagct
	Flag-mouseCD148	Forward: gattacaaggatgacgacgataagccta
		Reverse: gatgtaaccattagtcttccaacatgct
	CD1d-SCD	Forward: ggggggatcccggtactcgagggttcaataag
		Reverse: agtcgcggccgctcacaggacgccctgatagga
	Flag-humanCD45	Forward: gggattataaggacgatgatgacaaaca
		Reverse: tgaaccttgattaaagctggacttg
	Mouse β -actin	Forward: ctgtccctgtatgcctctg
		Reverse: atgtcacgcacgatttcc
	Hamster β -actin	Forward: ctgtccctgtatgcctctg
		Reverse: atgtcacgcacaatttcc
	Human β -actin	Forward: gagcacagagcctcgcttt
		Reverse: ccaggaaggaaggctggaag